POLITECNICO DI TORINO

Collegio di Ingegneria Chimica e dei Materiali

Corso di Laurea Magistrale
in Ingegneria Chimica e dei Processi Sostenibili

Tesi di Laurea Magistrale

Kinetic Modeling of Soot Oxidation inside Diesel Particulate Filter

Relatore
Prof. Marco Piumetti

Candidato
Alessia Natta

Ottobre 2018

Sommario

Le ottime prestazioni e la prolungata durata nel tempo rendono i motori diesel ancora molto diffusi nei mezzi di trasporto e nei macchinari pesanti. Tuttavia, gli alti valori di pressione e di temperatura raggiunti nella camera di combustione sono la causa di formazione di emissioni nocive allo scarico. In conseguenza della legislazione sulle emissioni sempre più stringente, tecnologie pre e post-combustione sono ancora in fase di perfezionamento. Per i veicoli da strada, i massimi livelli ammissibili di CO, idrocarburi totali (THC), NO_x, NH_3, massa (PM) e numero di particelle (PN) di particolato sono regolati.

L'obiettivo principale di questa tesi è l'elaborazione di un modello computazionale che catturi le principali caratteristiche dei fenomeni che intervengono nel filtro antiparticolato (FAP, in inglese DPF), una tecnica ben consolidata per la rimozione del particolato allo scarico dei motori diesel.

Il particolato (PM) è un inquinante con seri effetti sulla salute umana, dal momento che particelle di dimensione nanometrica possono penetrare nel tessuto polmonare ed entrare in circolo. Il particolato si origina in condizioni di carenza di ossigeno e alta temperatura ed è costituito da aggregati di carbonio elementare su cui vengono adsorbiti composti organici, zolfo e ossidi metallici. Le dimensioni variano dalla scala micrometrica a quella nanometrica.

Il processo che conduce alla formazione del particolato è complesso, perciò la composizione chimica e le proprietà fisiche non sono ben definite. Da qui, la complessità nello stabilire uno standard di riferimento, limitato ad un *range* dimensionale. L'analisi delle emissioni di particolato è realizzata *off-line*, tramite cicli-motore prestabiliti. Il regolamento europeo Euro 6 definisce gli attuali limiti in termini di numero e massa di particolato per veicoli *light-duty* (su base km), il regolamento Euro VI per veicoli *heavy-duty* (su base kWh). La definizione del particolato è strettamente legata al metodo di campionamento, perciò specifiche dettagliate sono necessarie nel momento in cui vengono stabiliti i limiti di emissione. I test sono realizzati secondo il protocollo stabilito dal *Particulate Measurement Programme* (PMP).

Attualmente, la tecnica per la rimozione del particolato di impiego più frequente è il filtro antiparticolato, costituito da un monolite ceramico con canali alternati passante/cieco per intrappolare il particolato. La formazione di un *cake* di particolato aiuta nel processo stesso di filtrazione. La rigenerazione del filtro viene eseguita per mezzo della combustione del particolato accumulato principalmente da parte degli agenti O_2 e NO_2. Dal momento che la temperatura necessaria per la combustione (600 °C) è superiore rispetto alla temperatura del gas esausto (200-500 °C), si può impiegare un bruciatore aggiuntivo allo scarico (rigenerazione attiva) oppure rivestire il monolite con un catalizzatore (rigenerazione passiva). A questo scopo, si utilizzano spesso ceria e metalli preziosi.

Il presente lavoro di tesi verte sulla modellazione unidimensionale di una singola coppia di canali, assunti rappresentativi per l'intero filtro. Il modello è stato realizzato con l'ausilio del *software* GT-SUITE prodotto da Gamma Technologies, che mette a disposizione librerie di componenti per la simulazione di sistemi termici, meccanici, chimici, elettrici, magnetici e di controllo e opportuni solutori di equazioni differenziali che costituiscono il modello. Il progetto vuole contribuire alla possibilità di riproducibilità dei principali fenomeni che avvengono nel FAP.

I dati sull'ossidazione di particolato sono stati resi disponibili da un precedente lavoro sperimentale realizzato nei laboratori della divisione *Combustion and Propulsion Systems* presso la *Chalmers University of Technology*, avendo come scopo ultimo quello di creare un collegamento fra modelli di scala di laboratorio e di scala *real-engine*. Tramite l'utilizzo di GT-SUITE, è stato costruito un modello rappresentativo dell'apparato sperimentale impiegato per testare il FAP e successivamente calibrato per i livelli di caduta di pressione e di emissioni secondo i dati sperimentali selezionati, con ulteriore validazione del modello per differenti *set* di dati.

La cinetica di ossidazione del particolato sotto diverse condizioni sperimentali è stata grande oggetto di investigazione scientifica. L'ambiguità nella definizione della composizione del particolato e il meccanismo di reazione complesso hanno reso il problema di non facile risoluzione. I fattori che devono essere considerati nell'analisi sono: temperatura, natura e livello di concentrazione dell'ossidante, natura e composizione chimica del particolato (sintetico o *real-engine*), presenza di vapor d'acqua ed evoluzione della struttura superficiale. Le ricerche si sono spesso concentrate su condizioni operative significative per rappresentare le reali condizioni nel FAP, provando la validitá di alcuni risultati simili.

Lo schema cinetico tradizionalmente impiegato è quello globale, rappresentato dalle equazioni 2.1-2.5. Il particolato è rappresentato come carbonio elementare che reagisce con specie gassose ossidanti. Il modello cinetico è del tipo *power-law*, con opportuni ordini di reazione per le specie ossigeno e biossido di azoto. Inoltre, la dipendenza dalla temperatura è presente nella relazione di Arrhenius per la definizione della costante cinetica (equazione 2.8). Il progredire della reazione è considerato con il modello *shrinking-core* (equazioni 2.6-2.7), secondo cui ciascuna sferula di particolato è da considerarsi ossidata indipendentemente dalle altre che la circondano e le reazioni avvengono all'esterno di particelle non porose.

Il modello cinetico *power-law* è utile per ricavare con facilità valori a partire da dati sperimentali, ma è estremamente semplicistico. Per questo gli si preferiscono modelli dettagliati che, in analogia alle cinetiche di reazioni catalitiche eterogenee, prevedono *step* intermedi e la presenza di complessi superficiali. Dedicati esperimenti hanno rilevato sui siti superficiali la presenza di specie quali ossigeno molecolare adsorbito $C(O_2)$, ossigeno atomico adsorbito $C(O)$ e specie miste del tipo $C(NO)$ e $C(ONO_2)$, ognuna con diversa stabilità e reattività. In letteratura esistono molteplici schemi di reazione dettagliati che includono possibili *step* di reazione.

Discrepanze inoltre si hanno anche sull'applicabilità del modello *shrinking-core*, che secondo alcuni autori sarebbe adatto per la descrizione della reazione di ossidazione assistita da NO_2 solamente, mentre un modello di diffusione attraverso la porosità della particella dovrebbe essere sviluppato quando l'agente ossidante è O_2.

Nello sviluppo del presente lavoro, lo schema cinetico descritto dalle reazioni 2.21-2.26 e leggi 2.27-2.32 è stato implementato. Le reazioni descritte sono collegate al modello del filtro in un apposito *template* fornito da GT-SUITE. La massa di particolato è tra le specifiche da inserire nel filtro in base a quella ricavata dai dati sperimentali con possibilità di distinzione fra *soot cake* e *substrate wall*. Dal momento che il *software* impedisce un'irragionevole eccessivo carico di particolato nelle porosità del filtro (*substrate wall*), l'intera massa di particolato è stata confinata al *soot cake*. Tuttavia, le reazioni superficiali di adsorbimento e desorbimento possono essere definite solo per il *wall*. Una strategia è stata appositamente studiata per superare questa limitazione. Il particolato è ossidato nel *cake* formando una specie gassosa, che verrà in seguito adsorbita nel *wall* e da cui si origineranno le specie gassose emesse (CO, CO_2, NO). La specie gassosa intermedia che viene assorbita è stata indicata come CO, tuttavia distinzione dalla CO gassosa si è resa necessaria. Una specie apposita $COAr_{0.5\ (g)}$ è stata definita secondo le proprietà termodinamiche della specie $CO_{\ (g)}$ e peso molecolare di 48. Quindi è stato richiesto un aggiustamento della stechiometria e del bilancio di massa, perciò anche la definizione chimica del particolato è stata variata, introducendo una specie di peso molecolare 32, $CAr_{0.5\ (s)}$. Un fattore di 32/12 ha corretto la massa di particolato da introdurre nel *cake*. Quando la specie superficiale CO viene adsorbita sui siti liberi, si ha il simultaneo rilascio della specie $Ar_{0.5}$ di peso molecolare 20. Il sito attivo superficiale nel *wall* è definito come Z/Z_{CO} (libero/occupato).

In equazione 2.33, la legge cinetica globale applicata in una precedente analisi degli stessi dati sperimentali, che si può considerare come il punto di partenza nella definizione del meccanismo cinetico del corrente lavoro. In particolare, si è verificato che un modello globale non era sufficiente per catturare la complessità del meccanismo. Le prestazioni dei due schemi cinetici globale/dettagliato sono confrontate nelle figure B.2-B.7. Per il tracciamento delle curve, sono stati selezionati opportuni istanti in cui si è raggiunto lo stato stazionario. Come si può osservare facilmente, l'impiego della legge cinetica individuata in equazione 2.33 non consente neanche nel caso dei risultati sperimentali di ottenere un andamento lineare, come invece ci si attenderebbe. L'analisi permette di individuare inoltre eventuali effetti di mass-transfer. Dal confronto fra i risultati della simulazione e i dati sperimentali si evince che il modello così definito è adatto alla descrizione del simultaneo effetto di O_2 e NO_2, seppur non essendo indipendente dal livello di concentrazione della seconda specie, mentre quando una sola delle due specie ossidanti è presente, il modello risulta poco performante. Inoltre, i risultati della simulazione evidenziano una previsione soddisfacente per l'energia di attivazione nello schema che porta alla produzione di CO_2.

Le proprietà catalitiche performanti della ceria (CeO_2) per la reazione di ossidazione del particolato ne rendono il perfetto candidato per l'esecuzione della rigenerazione passiva del FAP. L'ossido catalitico è in grado di accumulare e rilasciare ossigeno, grazie alla proprietà caratteristica del cerio di modificare stato di ossidazione da Ce^{4+} a Ce^{3+} introducendo ossigeno nella struttura cristallina. Meccanismi paralleli sono stati individuati in presenza di O_2 o NO_2 come agente ossidante. Il dopaggio di CeO_2 con cationi quali La^{3+}, $Pr^{3+/4+}$, Zr^{4+} ha dimostrato aumentata stabilità termica, capacità di stoccaggio di ossigeno e mobilità delle specie ossigenate. L'importanza dell'area superficiale ed entità del contatto fra ceria e particolato sono stati investigati in appositi studi di laboratorio. I metalli del gruppo platinico possono essere considerati come elementi attivi per la reazione, aiutando nel processo di cattura e trasferimento di ossigeno dal bulk alla superficie della ceria. Essendo la cinetica della reazione catalizzata ulteriormente complicata da fenomeni superficiali, in letteratura non sono numerosi gli schemi cinetici proposti a questo proposito. Nel lavoro qui presentato, si è scelto di analizzare la cinetica della reazione non catalizzata seppur modellando una cinetica eterogenea dal momento che il particolato è da considerarsi contemporaneamente come reagente e specie attiva.

La prima parte del progetto, realizzata in precedenza rispetto a questo lavoro di tesi, è consistita nell'elaborazione e nell'esecuzione di esperimenti per l'investigazione dei parametri che intervengono nel *loading* del filtro. A partire da filtri antiparticolato di dimensione reale, piccoli FAP sono stati tagliati, montati in tubi d'acciaio e assemblati in quattro cartucce, ognuna con 6 mini-filtri. Diversi substrati sono stati impiegati, cordierite, SiC, SiC rivestito da CeO_2 e SiC rivestito da Pt/CeO_2. La cartuccia è stata montata parallelamente a un filtro reale. Il *loading* dei filtri è stato effettuato con un motore *heavy-duty* del tipo 11L Eu6 eSCR. La combinazione di cicli-motore stazionari e transitori è stata utilizzata con diverse ripetizioni in modo da poter distinguere una procedura di *loading* lunga e corta. Dalla pesatura dei filtri prima e dopo l'operazione si è ricavata la massa di particolato.

Nella seconda fase del progetto, anch'essa precedente al lavoro svolto nella presente tesi, 27 esperimenti di ossidazione del particolato sono stati realizzati sui substrati descritti precedentemente. Ciascun mini-filtro è contraddistinto da un codice numerico come indicato in tabella 5.2. Un protocollo standard è stato definito per l'ossidazione del particolato. Ciascun mini-filtro è stato portato in un forno, fino a raggiungere la temperatura di 400 °C. Attraverso una serie di stati stazionari, con aumento ogni volta di 50 °C, la temperatura è stata nuovamente aumentata fino a 600 °C. L'alimentazione è stata mantenuta costante al valore di 1.978 l/min, con N_2 come componente principale a cui impulsi di aria e miscela 0.5% NO_2/99.5% Ar sono stati applicati. Per ogni valore stazionario di temperatura, è stata realizzata una sequenza programmata di ossidazioni a due livelli rispettivamente di NO_2 (400 e 800 ppm) e O_2 (1000 e 4000 ppm). Nell'ultima parte degli esperimenti, per ottenere l'ossidazione totale del particolato una grande quantità di aria è stata inviata nel sistema. A 600°C, variando la portata in ingresso sono state realizzate misure di cadute di pressione, quindi il reattore è stato fatto raffreddare fino a temperatura ambiente.

Durante gli esperimenti, sensori di temperatura, cadute di pressione e CO, NO_x and CO_2 nel flusso in uscita sono stati impiegati per raccogliere dati rilevanti. I segnali forniti dagli analizzatori di concentrazione sono stati opportunamente rielaborati in modo da eliminare eventuali oscillazioni e interpolati. Dall'integrazione delle quantità di CO e CO_2 emesse si è ricavato il *loading* di ciascun filtro (equazioni 5.1-5.2).

Tra tutti gli esperimenti realizzati, l'esperimento 12 è stato scelto per calibrare i parametri del modello cinetico. Le caratteristiche del filtro sono: filtro di SiC non rivestito da catalizzatore, *loading* lungo e con catalizzatore di ossidazione (DOC) a monte. Il profilo di temperatura per l'esperimento in figura 5.2 evidenzia la presenza di due distinte fasi, ciascuna corrispondente a circa metà della durata dell'esperimento. Le condizioni operative applicate negli istanti compresi fra 8000 s e 19500 s sono state considerate adatte per la determinazione dei parametri cinetici.

Il modello realizzato con GT-SUITE è riportato in figura 5.7. Si tratta di un semplice *input-output*, un *template* fornito dal programma ha consentito la modellazione del filtro. L'utente inserisce le specifiche geometriche del filtro e le proprietà termiche, estrapolate da quelle fornite nella libreria per il tipo di substrato utilizzato. Inoltre, si specifica il *loading* e le reazioni di rigenerazione in appositi *template* che vengono collegati esternamente al filtro. Una semplificazione che è stata adottata nella definizione modello è l'imposizione della temperatura nel filtro, pari alla temperatura della corrente di alimentazione. L'esotermicità delle reazioni è stata considerata e si è imposta la condizione di adiabaticità, ma non si è definito un modello termico *ad hoc* per l'esperimento, forte semplificazione che può aver compromesso le prestazioni del modello. Invece, ci si è concentrati sulla flessibilità del modello, in modo da poterne estendere l'applicabilità a diversi *set* di dati sperimentali. Infatti, non vi è la memorizzazione di dati all'interno del modello stesso ma le specifiche in ingresso vengono lette da un foglio excel che può essere modificato dinamicamente tramite riscrittura. Questo permette da un lato di non avere una gran quantità di dati all'interno dello stesso modello e dall'altro di avere la possibilità di processare i dati sperimentali, per esempio selezionando uno specifico intervallo di interesse.

In totale, due modelli di filtro sono stati calibrati: filtro di cordierite e filtro di SiC. Inizialmente, si sono calibrati i parametri per definire il filtro precedentemente all'operazione di *loading,* utilizzando i dati di cadute di pressione raccolti a temperatura ambiente applicando diversi valori di portata entrante. I valori dei parametri ottimizzati con procedura automatica e manuale sono riportati in tabella 5.4. I parametri concernenti il *loading* di particolato, nello *step* successivo di calibrazione del modello, sono stati mantenuti ai valori di *default*, dal momento che non vi erano dati sperimentali disponibili (precedenti all'ossidazione) per effettuare un'ottimizzazione.

In seguito, ci si è concentrati sugli esperimenti di ossidazione. Ingenti sforzi sono stati spesi per la determinazione di un modello cinetico, così come definito precedentemente. Una volta stabiliti gli *step* di reazione, si è effettuata la calibrazione dei parametri cinetici tramite tre susseguenti ottimizzazioni. A causa delle peculiari condizioni sperimentali, la calibrazione per i parametri che coinvolgono le reazioni assistite da O_2 e da NO_2 è stata effettuata simultaneamente. Tramite procedura manuale di *trial-and-error* si sono individuati alcuni valori di energia di attivazione e di fattore pre-esponenziale consistenti con quelli di letteratura. Quindi, si è effettuata una prima ottimizzazione unicamente dei valori di fattore pre-esponenziale, una seconda per i valori di energia di attivazione e una terza ottimizzazione su un range ristretto nuovamente per i valori di fattore pre-esponenziale.

A complemento della procedura di ottimizzazione, si è esaminata l'influenza dei diversi parametri sull'errore complessivo, calcolato secondo l'equazione A.1. Nel corso della prima ottimizzazione, si è potuto verificare che i parametri pre-esponenziali (definiti come 10^{Ai}) più significativi sono A_1, A_4 e A_5, dei quali A_4 non è giunto a completa convergenza nel numero di iterazioni previste. Anche nel caso dell'energia di attivazione Ea_1 ed Ea_4 risultano essere determinanti nel calcolo dell'errore complessivo e giungono a convergenza nelle iterazioni previste. Nel corso della terza ottimizzazione, quando il range è stato ristretto, A_1 e A_5 continuano ad essere determinanti nel calcolo dell'errore totale, inoltre anche A_2 e A_3 hanno rilevanza a questo livello. Mentre A_1 dimostra buona convergenza, A_2, A_3 e A_5 sembrano necessitare di ulteriori iterazioni per la convergenza completa. In totale, l'analisi della procedura di ottimizzazione dimostra la rilevanza sull'errore totale della reazione di ossidazione da parte dell'ossigeno nel meccanismo. Inoltre, si evidenzia l'effetto sinergico dei vari parametri cinetici per la determinazione delle emissioni complessive.

I valori dei parametri ottenuti in seguito ad ottimizzazione sono presentati in tabella 6.1. La validità del modello può essere investigata dal confronto diretti fra i valori di emissione predetti e quelli simulati. Per quanto riguarda la specie NO (figura 6.3) si verifica che la simulazione prevede una conversione totale dell'NO_2 (rilevabile dai valori di emissione di NO, circa 400 e 800 ppm, gli stessi valori di concentrazione della specie ossidante applicati), a differenza di quanto accade per i dati sperimentali. Si hanno inoltre nel caso della simulazione dei sotto-livelli che evidenziano la presenza di meccanismi di produzione diversi a seconda che l'NO_2 sia alimentato da solo oppure in compresenza con O_2. L'andamento dei sotto-livelli è inversamente proporzionale ai livelli di O_2 iniettato. Inoltre, all'aumentare della temperatura, questo effetto è meno evidente. Si deve perciò considerare l'effetto dello *step* di reazione in equazione 2.26 che coinvolge indirettamente O_2 nella produzione di NO. In particolare, dal momento che l'effetto varia con la temperatura, il parametro di energia di attivazione sarà maggiormente influente. Il modello inoltre è in grado di catturare solamente cambiamenti bruschi fra i vari stati stazionari e non variazioni graduali angolari, imputabili al carattere "appiccicoso" della molecola di NO_2 nel sistema di alimentazione. Nel caso della CO_2 (figura 6.6), la predizione del modello è migliore, in particolar modo quando entrambe le specie ossidanti sono presenti e quando l'NO_2 è alimentato in concentrazione più alta. Di nuovo, questo effetto si può attribuire allo *step* di reazione 2.26. I dati sperimentali mostrano bordi non definiti che non trovano corrispondenza nelle brusche variazioni al raggiungimento di stati stazionari dei risultati della simulazione. Questo comportamento è meno evidente ad alta temperatura e suggerisce l'implementazione di parametri cinetici troppo dissimili per i vari *step* di reazione. Una buona corrispondenza fra risultati sperimentali e simulati si osserva invece quando l'ossigeno è iniettato da solo ad alta temperatura a diversi livelli di concentrazione. Al contrario, l'effetto dell'ossigeno a bassa temperatura e sottostimato.

Considerando la *performance* predittiva del modello nel complesso, si può notare che la migliore corrispondenza è stata raggiunta per la CO_2 e la peggiore per il CO. Il differente livello di concentrazione delle due specie potrebbe aver avuto influenza sulla procedura di ottimizzazione, dal momento che l'errore totale è determinato in prevalenza dai valori più alti di concentrazione, quelli appunto della CO_2. Una caratteristica del modello è inoltre la sottostima delle emissioni quando l'ossigeno è alimentato a bassa temperature, suggerendo la necessità di un miglior calcolo dei parametri cinetici dello *step* di reazione 2.21.

Il modello cinetico è stato concepito in modo che gli *step* cinetici 2.21 e 2.22 siano determinanti per il meccanismo di reazione e le reazioni di adsorbimento della specie superficiale e desorbimento dei prodotti 2.24, 2.25, 2.26 siano veloci in modo da non avere accumulo nel sistema.

In complemento all'analisi delle emissioni si sono valutate le prestazioni del modello considerando la previsione della conversione del substrato e del ricoprimento della specie adsorbita. Il *trend* di conversione rispetta quello sperimentale, riuscendo a catturare gli *step* successivi attraverso i quali la reazione si sviluppa (figura 6.10). Il parametro di ricoprimento superficiale θ_{CO} si attesta su valori infinitesimali, circa 10^6 volte minore dei valori di emissione, indice del fatto che non vi è accumulo della specie in superficie e il desorbimento dei prodotti è istantaneo, così come desiderabile (figura 6.2). Le curve sono state tracciate per il primo e l'ultimo volume in cui è stato discretizzato il reattore, presentando un lieve scostamento. Le oscillazioni che si creano per il primo volume di reattore possono essere attribuite al susseguirsi immediato delle reazioni, generando un'instabilità numerica. Le emissioni di CO (figura 6.8) sono largamente sottostimate a bassa temperatura e sovrastimate ad alta temperatura, risultato che suggerisce la necessità di diminuzione del valore di energia di attivazione della reazione che porta alla produzione della specie chimica. Le reazioni 2.21, 2.22, 2.23, 2.24 intervengono nella produzione di CO. Quando l'O_2 è iniettato dal solo nel sistema, la predizione del modello risulta essere peggiore rispetto agli altri casi.

Una volta calibrato il modello cinetico secondo i dati dell'esperimento 12, si è proceduto all'applicazione del modello nel caso di *set* di dati differenti, fornendo così una validazione del modello elaborato. Si deve sottolineare come questa analisi sia precoce, dal momento che il modello base necessita ulteriori perfezionamenti. Fatte queste precisazioni, si sono selezionati alcuni set di dati sperimentali che potessero fornire un confronto sensato con i dati considerati in precedenza. Si sono scelti perciò il filtro #14, substrato di cordierite, identiche condizioni di carico (*loading* lungo, DOC a monte), il filtro #21, substrato di SiC, *loading* corto con DOC a monte, il filtro #26 substrato di SiC, *loading* lungo senza DOC a monte e il filtro #11, SiC rivestito da ceria, identiche condizioni di carico. Le principali osservazioni che sono state effettuate a questo punto dell'analisi sono:

- *trend* del tutto similare per le emissioni di NO in tutti i *set* di dati, con eccezione nel caso del filtro #26, dove i sotto-livelli ottenuti al raggiungimento dei vari stati stazionari presentano un andamento crescente all'aumentare della concentrazione di O_2 iniettato, ovvero opposto rispetto agli altri casi; i migliori risultati si ottengono nel caso del filtro #11, che presenta identiche condizioni di carico del filtro #12
- *trend* simile a quello precedentemente osservato per le emissioni di CO_2, con *performance* predittive inferiori da parte del modello ad alta temperatura
- larga sottostima per le emissioni di CO, con eccezione del filtro di cordierite #14, in cui il *trend* ad alta temperatura è migliore
- le diverse condizioni di carico del filtro generano differenze nella reattività del substrato (diversi parametri cinetici, presenza di effetti di trasporto di materia) e presumibilmente nelle prestazioni del solutore (minore/maggiore quantità di *soot*)

- la natura del substrato (cordierite/SiC) provoca differenze nella temperatura raggiunta alla parete avendo perciò influenza sullo svolgimento delle reazioni
- in presenza del catalizzatore, non è del tutto corretta l'applicazione dello schema cinetico della reazione non-catalizzata dal momento che fenomeni quali *spill-over* di ossigeno dalla ceria e altre interazioni con il substrato catalitico sono non trascurabili.

In conclusione, il lavoro sviluppato ha rispettato gli obiettivi prefissati e di elaborazione di un modello integrato e flessibile di filtro anti-particolato nell'esame di diverse condizioni sperimentali. I precedenti modelli si limitavano all'analisi di una singola specie ossidante ad un livello di concentrazione prestabilito ed è proprio nel caso di compresenza delle due specie che il modello garantisce migliori risultati. Inoltre, le limitazioni del *software* impiegato sono state superate con successo. Il modello risulta semplice e necessita di ulteriore perfezionamento, ma non ha la pretesa di spiegare dettagliatamente i fenomeni complessi che intervengono realmente nel filtro, quanto piuttosto di fornire uno strumento in grado di stabilire un collegamento fra esperimenti di laboratorio e *real-engine*. La predizione del modello risulta discreta per le emissioni di NO e CO_2 e non ancora soddisfacente per le emissioni di CO. Comunque, è necessario un lavoro ulteriore per aumentare l'accuratezza anche nella predizione delle prime due specie. Nonostante la presenza simultanea di condizioni sperimentali diverse sia di gran interesse, come ad esempio la natura e il livello di concentrazione della specie ossidante, la temperatura, le condizioni di *loading* e la natura del substrato, dall'altro lato costituisce un grande limite per la complessità aggiunta nel cercare di ottenere risultati accurati.

Come prospettiva futura, si suggerisce un miglioramento dello schema di reazione, in particolar modo legando direttamente la produzione di CO alla concentrazione degli ossidanti, la calibrazione distinta dei parametri cinetici per le varie specie, utilizzando i valori implementati come valori di prima ipotesi ed eventualmente separando i casi in cui la singola specie ossidante è alimentata da sola, l'elaborazione di un modello termico per il filtro e l'analisi più approfondita dei fenomeni di *mass-transfer*, eventualmente riconsiderando l'inapplicabilità del modello *shrinking-core*. Gli andamenti delle cadute di pressione e della conversione per il modello sono considerati con buona approssimazione fornire migliori risultati quando la predizione del modello sulle emissioni sarà maggiormente significativa.

Indice

1. Introduction

1.1 Background

Diesel engines are a widespread technique for transportation and heavy machinery applications. High fuel performances compared to engine torque output and durability over the years are the reasons why there is still massive reliance on diesel engines. Nevertheless, the high pressure and temperature levels in the cylinder are at the origin of problems in terms of pollutant emissions. As a consequence of the ongoing stringent legislation, pollutant issues still need to be faced completely. For road vehicles, levels of CO, total hydrocarbons (THC), NO_x, NH_3, particulate mass (PM) and number (PN) are regulated. Pre and post-combustion technologies have been developed in order to meet the required limits.

Analysis of particulate matter removal technique is the main subject of this thesis, the present work dealing with diesel particulate filter, a well-established particulate matter aftertreatment technology. On the other hand, it is important to mention that prevention on some extent on particulate formation has been achieved with fuel composition tuning and advanced injection control (timing, pressure).

1.1.1 Particulate Matter Characterization

Particulate matter (PM) is a serious environmental pollutant with dangerous health effects. Particulate matter is a complex species, including aggregates of elemental carbon (soot) with adsorbed organic compounds, sulphur and metal oxides.

Soot is originated under fuel-rich conditions at high temperatures in case of insufficient oxygen supply.

The hydrocarbons undergo the subsequent steps of pyrolysis, nucleation, surface growth, coalescence and agglomeration during soot formation. Pyrolysis generates soot precursors, mainly unsaturated hydrocarbons, polyacetylenes, and polycyclic aromatic hydrocarbons (PAH). Nucleation is the process of particle synthesis from gaseous reactants: small-size hydrocarbons combine to form large aromatic molecules. Then, hydrocarbons from gas phase start depositing on spherule surface, increasing surface area. The process of surface growth is more relevant for small particles since the content in radical sites is higher. Collision in between particle leads to a decreased particle number and increased particle size. PM formation is accomplished with the adsorption of organics and partially oxidized hydrocarbons on soot surface. [1]

The schematic representation is provided in figure 1.1.

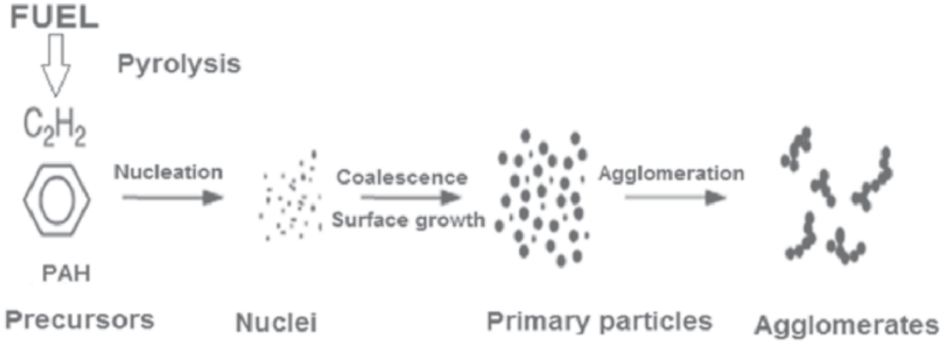

Figure 1.1. Schematic representation of particulate formation during typical combustion process, from [2].

Emitted particles size spans in the nano and microscale. Particles of such dimensions can penetrate the human respiratory system and can be accumulated into pulmonary region. Particles of 20 nm size have been shown to accumulate the most on alveola, eventually penetrating the alveolo-capillary membrane and entering the systemic circulation.

Research has been carried out in order to demonstrate the correlation in between particulate matter and respiratory disorders among the possible health effects. Detailed information on epidemiological and toxicological studies can be found in 2009 EPA report [3].

1.1.1.1 Emission Standards

According to the previously explained complex process that leads to PM formation, it is clear that PM chemical composition and physical properties are not well-defined, depending on factors such as type of fuel, engine, operating conditions and upstream diesel oxidation catalyst (DOC). The optimization of the combustion process in the engine and the implementation of the aftertreatment system providing reduction in PM mass generate as side-effect a change in particle nature (increase in organic volatile fraction).

PM chemical analysis is carried out off-line after exhaust sampling and PM extraction, however composition possibly results altered during measurement procedure due to contamination with organic substances. No single measurement method can be used for defining completely PM chemical composition, the main techniques have been reviewed by Maricq [4].

PM emission regulations do not define a specific chemical composition and physical description is limited to categories according to particle dimension range.

Particulate matter emission is restricted for heavy duty diesel engines (road vehicles) by European regulation EC 595/2009 and further amendment EC 133/2014 (Euro VI) as summarized in table 1.1.

Table 1.1. Particulate emission limits for road vehicles according to Euro VI regulation [5].

	PM (mg/kWh)	**PN (#/kWh)**
WHSC	10	$8.0 \cdot 10^{11}$
WHTC	10	$6.0 \cdot 10^{11}$

With latest European regulation entrance into force, the first limit for particle number has been introduced and, on the other hand, a drastic reduction in particle mass limit has been established. However, standard testing cycles for emissions have been changing throughout the regulation development process, resulting in the possibility of rough comparison only.

Test cycle standards World Harmonized Stationary Cycle (WHSC) and World Harmonized Transient Cycle (WHTC) have been agreed within United Nations Economic Commission of Europe (UNECE) since Euro VI standards formulation. WHSC combines thirteen modes of engine speed and load, while WHTC consists in a test drive of 1800 s with several motoring segments. Both test cycles are based on typical worldwide heavy-duty engines driving conditions. Euro VI standards also require on-board devices to check performance of emission control system and to identify system failures. [6]

The definition of particulate matter is intimately related to the sampling method, therefore detailed specification must be given in establishing diesel emissions regulation.

PM volatile fraction can desorb into the gas phase, condense on existing solid particles or nucleate forming new particles according to temperature and surrounding conditions. Particulate trapping technology causes a removal of solid particles while volatile substances remain in gas phase. For high supersaturation degrees, with temperature reduction, nucleation of volatile material becomes predominant over condensation since the solid fraction of the material has been reduced. Therefore, two different particle types develop: large-sized solid particles (soot) and low-sized volatile material. It has been shown that typically PM has a bimodal size distribution, with large number of small particles and low number of larger particles, containing most of the mass. Health effects need also to be considered differently due to dissolution of volatile material into the surroundings.

PM gravimetric analysis is mainly driven by particles deriving from accumulation phenomena, while particle number concentration (PN) result mainly depends on small nuclei. [7]

Two main points to retain while establishing particle emission regulations are the measurements reproducibility and the relevance respect to health effects. No particle standard exists for comparison, thus making the procedure not straightforward. Volatile fraction is removed before analysis and excluded from measurements for practical reasons.

Emitted particles number and mass tests are realized according to a specific protocol elaborated by the Particulate Measurement Programme (PMP) working group of the UNECE Working Party on Pollution and Energy (GRPE). [8]

Diesel engine PM is sampled from exhaust gas, diluted with clean air and collected on a filter. Dilution is relevant in order to reduce particle concentration and temperature, preventing condensation and nucleation of the organic phase that would instead occur with direct cooling. Dilution ratios are employed so that the temperature of the exhausts should not exceed 47 °C. Flow dilution tunnel is used with the possibility of a total (constant volume sampler, CVS) or partial dilution (partial flow dilution sampler, PFDS) of the exhaust. A cyclone can be added to remove coarse particles. The collected sample is then weighted. The major drawbacks of the gravimetric measurement method are the possibility of non-constant composition of the sampled species as a consequence of condensation/evaporation of volatile substances or particle coagulation and the absence of transient behaviour data during engine cycle.

In figure 1.2, PM schematic measuring asset is shown and change in distribution of particle size is pointed out.

In the combustion chamber, primary particles of 10-30 nm are formed. In the exhaust pipe, coagulation occurs as a consequence of high temperature. In the dilution tunnel, exhausts are mixed with dilution air and nuclei of volatile material particles develop. Coarse particles derive from non-combustion processes.

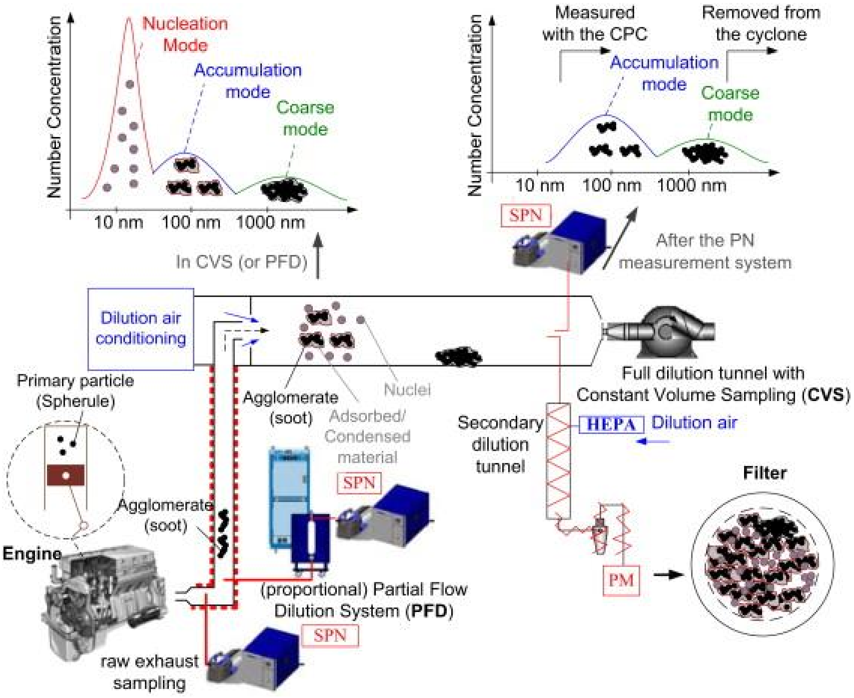

Figure 1.2. Sequence of particle transformation from the engine to the measurement system, adapted from [9].

Particle number concentration measurement is obtained from condensation particle counter (CPC). CPC is connected to the flow dilution tunnel. The exhaust is preconditioned with heating and dilution for volatile species removal, PN counter accounts for particles with dimensions comprised in between 23 nm and 2.5 µm, relevant for their possible health effect. Coarse and nanoparticles are therefore excluded from measurements. [7,8]

1.1.2 Diesel Particulate Filter

Filtration technique is considered the current most feasible solution in order to limit particulate emissions for road vehicles. Diesel particulate filter (DPF) is a wall-flow ceramic monolith with many axial parallel and alternatively plugged channels intended to trap particulate. Silicon carbide and cordierite are common materials for the filter.

The exhaust gas enters the open channels and flows to the adjacent cells through porous walls. Filtration in the clean filter is due to soot deposition in the pores of the material (depth filtration), then soot cake layer formation is accomplished and its contribution to the entire filtration mechanism becomes predominant (cake filtration).

1.1.2.1 Filter regeneration

Regeneration is needed as a consequence of the arisen pressure drop across the filter with increased fuel consumption. During regeneration, soot is oxidized to CO_2 by O_2 and NO_2, the latter coming from upstream DOC. In case of oxygen depletion, total oxidation of soot is hindered and increase in CO emissions occurs.

Soot oxidation reactions arise at temperatures above 600 °C, however diesel exhaust typical temperatures are comprised in between 200 °C and 500 °C [10]. Two main strategies are employed for overcoming the problem in filter regeneration, namely active and passive, or a combination of both is also common.

Active regeneration consists in rising the temperature of the exhaust through an energy source. Dedicated sensors monitor the soot cake formation. Engine throttling is able to increase the exhaust temperature only to a certain extent, resulting into lower overall air-to-fuel ratios and having as drawback increased HC and CO emissions. External energy supply is also used. A differential pressure sensor detects when a certain limit for pressure drop across the filter is exceeded and sends a signal to the engine central unit (ECU), which, in turn, activates a diesel burner placed in the exhaust. As an alternative to the burner, an electric resistance can be employed.

Passive regeneration technique relies on catalysts during normal engine operation. A schematic representation of this technique is provided by Johnson Matthey in figure 1.3. Catalytic species can be introduced as additives in the fuel or the porous substrate can be washcoated with Ceria (CeO_2) or noble metals. Ceria is active in lowering soot oxidation operated by oxygen, while Pt provides catalytic activity for NO, CO and HC oxidation reactions. However, passive regeneration alone fully depends on driving cycle and in some cases adequate temperatures for regeneration are not met. Full passive regeneration regime is desired for non-road and heavy-duty vehicles, thus avoiding the need for extra power. Continuously Regenerating Trap (CRT®) system by Johnson Matthey consists in a Pt-catalysed substrate placed upstream the filter which generates NO_2 that oxidizes the collected soot.

Passive-active technique combination results in a decreased fuel penalty caused by active regeneration and in the possibility of performing low temperature regeneration. [1]

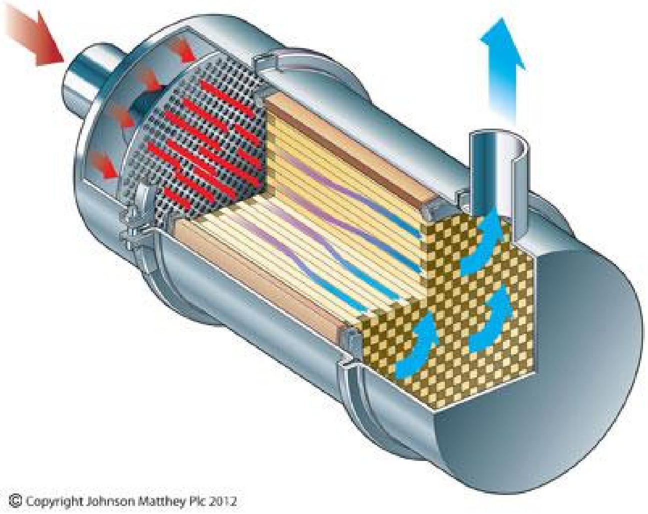
© Copyright Johnson Matthey Plc 2012

Figure 1.3. Schematic representation of a passively regenerating DPF.

Oxygen is naturally present in the exhausts and reacts at high temperature, therefore its contribution is relevant mainly in active regeneration systems. Nitrogen dioxide operates at lower temperatures, namely when a catalyst is present. NO_2 mainly derives from catalytic oxidation of NO increasing NO_2:NO ratio. The effect of oxidation enhancement is thermodynamically limited at high temperatures by NO_2 decomposition.

It is clear that DPF is a complex system involving multiphase reactions, material transport and separation processes on spatial and temporal multiscale levels [10]. In the present work, 1-D approach has been considered, describing phenomena occurring in a single channel as representative for the entire filter.

1.1.3 Maritime Emissions Regulation

Currently no emission regulation for particulate matter exists for marine vessels. Allowable NO_x and fuel sulphur content have been established by International Maritime Organization (IMO) with MARPOL Annex VI [11].

Fuel sulphur content is regulated to the level of 0.1% for Emission Control Area (ECA) and 3.5% elsewhere. ECA includes Baltic sea, North Sea, US and Canada costs. As an alternative to the use of low-sulphur fuel, exhaust gas cleaning systems such as scrubbers are also permitted, given that performances are the same. A dedicated study has compared the use of different low sulphur content oils and exhaust gas cleaning system, the latter case being proven to be efficient in PM removal at lower costs [12].

Traditional techniques implemented for vehicles are not suitable due to specific fuel quality and engine conditions. Passive regeneration is the only alternative viable as a consequence of the low pressure drop level across the filter. Also, heavy fuel oil has high sulphur and heavy metal (V, Ni, Fe, Na) content. The developed catalyst should therefore consider the interaction with these components, namely metals can act as fuel-borne catalysts and ash content is high in the form of metal oxides and sulphates. Pt cannot be used as catalyst due to sulphur poisoning effect, while NO_2 formation is inhibited. In the recent past years, a Pd, V_2O_5/SiC sulphur-resistant filter catalyst has been developed by Haldor Topsoe [13].

1.2 GT-SUITE software

The model is created on GT-SUITE CAE software from Gamma Technologies. The software provides component libraries for simulation of flow, thermal, mechanical, chemical, electrical, magnetic and control systems. In particular, it is possible to develop 0D, 1D and 3D models for simulation of engine powertrain with integrated or stand-alone aftertreatment systems. In addition, optimization features and distributed parallel computing tools are provided.

1.3 Methods and Objective

The project is focused on giving contribution to DPF governing mechanisms reproducibility.

Data on soot oxidation were available from previous experimental work carried out in Chalmers Combustion and Propulsion Systems division laboratories. First, a model of DPF testing experimental asset is built with the help of the software GT-SUITE. Then, analysis and calibration of the model on pressure drop and emissions experimental data are performed, with simultaneous validation for different sets of data.

Laboratory models have the advantage of being predictable, but they often lack applicability on real-systems. The use of synthetic soot in the experiments differs significantly from real-engine particulate in the results, since effects such as operating conditions are neglected.

One of the goals of the project is to provide a new approach for aftertreatment analysis with a cross-over in between laboratory-scale and real systems.

Simulations are useful tools for a better understanding over the multiple factors acting on the phenomena. The exact mechanisms at the basis of DPF activity still need to be understood completely, even if practical effectiveness has been proven. Also, establishing an overview of several operating conditions is the purpose of the whole study, in order to be able to obtain general validity results.

2. Soot Oxidation

Extensive research has been performed over the past twenty years on soot oxidation kinetics under different operating conditions. Ambiguity in soot composition and complex reaction mechanism make the process of kinetic modeling not straightforward. Given that the elaboration of general applicability theory is not achievable, different experimental works have proven the validity of similar results.

The synergistic effect of several factors need to be considered in the analysis: temperature, nature and concentration levels of the oxidants, soot exact chemical composition, presence of water vapour and evolution of carbon surface structure. Dedicated formulation of experiments should therefore be conducted. It is relevant to point out that experimental analysis is often limited to restricted parameter ranges that are significant for real aftertreatment operating conditions.

First, an overview on traditional laboratory experimental equipment is given: existing literature kinetic data have been extrapolated from such assets. Then, kinetic mechanisms proposed in literature are reviewed. Finally, the kinetic mechanism implemented in GT-SUITE model is presented.

2.1 Experimental Methods

In order to get a better understanding over the mechanisms which act on regeneration reactions in DPF, it is important to identify reaction characteristics for both individual spherules and soot cake bed as a whole. Reproducibility of data is also fundamental, leading thus to frequent substitution of the diesel sample with synthetic model soot.

Several experimental assets have been developed, regardless of the specific oxidizing agent used. [14] Experiments can be run isothermally or through temperature programmed oxidation (TPO). With TPO, oxidants are fed while sample temperature is raised slowly. Collections of data over steady-state and transient behaviours exist.

Fixed beds and thermogravimetric analysis are the most employed techniques for investigating soot oxidation. Diluting soot with some inert solid helps in preventing excessive temperature rise and in enhancing the contacts with the oxidant. [15]

2.2 Reaction Kinetics

Global, semi-global and detailed kinetic mechanisms are discussed.

Reactions occurring in DPF that are have not been included in the described mechanism are: NO oxygen operated oxidation to NO_2, hydrocarbons oxidation and combined O_2-NO_2 oxidation. Reported literature works provide different levels of complexity in the reaction mechanism.

2.2.1 Global Kinetics

Global power-law kinetics is often used to describe soot oxidation reaction rate, making possible a simple estimation of the reaction parameters from experimental studies.

Soot is modelled as elemental carbon (C) reacting with oxidant gas species according to the simple single-step reaction mechanism presented in equations 2.1-2.4.

$$C_{(s)} + 0.5\ O_{2\,(g)} \rightarrow CO_{(g)} \quad (2.1)$$

$$C_{(s)} + O_{2(g)} \rightarrow CO_{2\,(g)} \quad (2.2)$$

$$C_{(s)} + NO_{2\,(g)} \rightarrow CO_{(g)} + NO_{(g)} \quad (2.3)$$

$$C_{(s)} + 0.5\ NO_{2\,(g)} \rightarrow CO_{2\,(g)} + 0.5\ NO_{(g)} \quad (2.4)$$

Reaction rate follows the general expression presented in equation 2.5.

$$-\frac{dC}{dt} = k[O_2]^{n_{O_2}}[NO_2]^{n_{NO_2}} \quad (2.5)$$

The terms in the kinetic expressions are the concentrations of the gaseous species. n_{O2} and n_{NO2} are oxygen and nitrogen dioxide reaction orders, respectively. Literature reports oxygen reaction order varying from 0.5 to 1. For NO_2 oxidation, nitrogen dioxide reaction order is not significantly different than 1. [15,16,17]

Due to its simplicity, the global kinetic model does not consider detailed phenomena such as adsorption and desorption of surface species. Global kinetics is useful for predicting carbon consumption but fails in the simulation of carbon activation or product selectivity (CO, CO_2). Applicability is therefore limited to a narrow experimental parameters range. A sequence of elementary reaction steps should instead be preferred.

2.2.1.1 Shrinking Core Model

The number of available active sites (N_t) to be included in reaction rate expression is defined in the equation 2.6. λ is the surface concentration of active sites and S_a represents the carbon specific surface area.

$$N_t = \lambda S_a \quad (2.6)$$

Specific surface area is in turn a function of conversion ξ, according to equation 2.7:

$$S_a = S_{a,0}(1 - \xi)^{n_C} \quad (2.7)$$

$S_{a,0}$ is the initial carbon surface area and n_C the carbon reaction order. Therefore, with increased conversion, the number of sites available for reaction and reaction rate are decreased.

n_C is assumed in several studies to be equal to ⅔ since this value reflects the decreasing radius of non-porous mono-dispersed spherical particles, the so-called shrinking core model. Each identical spherule is considered to be oxidized independently, contacts in between spherules are neglected. Surface reaction occurring at the exterior of non-porous particles is the rate-determining step, with reaction front propagating from the periphery to the centre. [16]

Other models describing reaction progress differently to the shrinking core theory have been elaborated.

Zhdanov at al. [18] compared 3-D shrinking core and 2-D model performances in describing soot oxidation and fitting experimental data. According to 2-D model, a spherule is shaped as disk-like pellet composed of several carbon sheets, with reaction front propagating from sheet periphery to the centre. Also, a better fit to experimental data has been shown for models taking into account particle size distribution. Indeed, the results obtained in this case are physically meaningful. Expression of spherule volume is therefore substituted with average value obtained from integration of a distribution function.

2.2.1.2 Reaction Rate Constant

Temperature dependence for reaction rate constant is taken into account with Arrhenius equation (equation 2.8)

$$k = A \cdot e^{-\frac{E_a}{RT}} \tag{2.8}$$

where A is defined as the pre-exponential factor and E_a as the activation energy for the reaction. Typical activation energy for oxygen reaction is reported in literature to be 140-170 $kJmol^{-1}$, but the whole range 102-210 $kJmol^{-1}$ is covered. Lower values are reported for nitrogen dioxide reactions. [15]

Wang-Hansen *et al.* [19], providing an alternative to detailed kinetics, expressed in an unconventional way the progress of the reaction, with conversion dependence for activation energy. Dispersive kinetic approach was applied.

2.2.2 Semi-global Kinetics

Fewer data currently exist in literature about kinetic parameter estimation for surface reaction detailed scheme in soot oxidation. Surface kinetics is modelled in analogy with heterogeneous catalytic reactions.

Semi-global models consider more than one explicit reaction step while the steps are not necessarily elementary. Intrinsic kinetics neglects transport processes.

Semi-global kinetics is presented for O_2-aided oxidation only, yet a similar analysis can be extended to NO_2-aided oxidation. The reactions listed in the global kinetic mechanism are expanded into further lumped reaction steps. Surface complexes formation is considered.

2.2.2.1 Langmuir-Hinshelwood Kinetics

Langmuir-Hinshelwood kinetics is employed for heterogeneous catalysed bimolecular reactions where interaction in between the reactants occur after adsorption on the surface. In the specific case of soot oxidation, Langmuir-Hinshelwood mechanism describes oxygen adsorption on a vacant site and further reaction with carbon. Oxygen adsorption can occur either dissociatively or non-dissociatively. In case of non-dissociative adsorption, reaction scheme for O_2 oxidation is listed in equations 2.9-2.10.

$$C + O_{2\,(g)} \rightarrow C(O) \tag{2.9}$$

$$C(O) \rightarrow CO_{(g)} \tag{2.10}$$

Activation energy for desorption has been attested to be considerably higher than activation energy for adsorption. The model however does not provide a general accurate description for experimental data, but it is again limited in the application to defined temperature and concentration ranges.

2.2.3 Detailed Kinetics

Several reaction mechanisms have been developed and validity has been tested against several experimental assets. It is clear anyway that each mechanism on its own is not able to capture totally the complexity of the reaction.

Agreement in literature is found on process development through two fundamental subsequent steps: oxygen is transferred from the gas phase to the surface with formation of a solid complex and the surface complex is then decomposed, with a carbon atom release from the surface.

Temperature programmed desorption (TPD) and gravimetric experiments have shown the formation of surface oxide complexes. Surface oxide species include adsorbed molecular oxygen $C(O_2)$, adsorbed mobile molecular oxygen $C(O_2)_m$, adsorbed oxygen atoms C(O) or adsorbed mobile oxygen $C(O)_m$. When NO_2 is also present, mixed surface species are formed.

Surface oxygenated carbon complexes are attributed to different functionalities: quinone, ether, anhydride, carbonyl, phenol, lactone, carboxyl. In the NO_2 oxidation, nitro and nitrite groups are represented by C(NO) surface species, eventually containing acidic functionality represented by $C(ONO_2)$. [20]

The relative importance of the single elementary steps to be included in the detailed reaction mechanism has been debated. Here some representative mechanisms have been selected in between the ones proposed in literature for O_2 and combined NO_2-O_2-assisted oxidation, respectively.

Soot oxidation with oxygen has been largely investigated. Li and Brown [21] proposed the sequence listed in equations 2.11-2.15:

$$*C + O_{2\,(g)} \leftrightarrow C(O_2) \quad (2.11)$$

$$C(O_2) \rightarrow C(O) + CO \quad (2.12)$$

$$C(O) \rightarrow C(O) \quad (2.13)$$

$$*C + O_{2\,(g)} \rightarrow CO_2\text{, via } C(O) \quad (2.14)$$

$$*C + O_{2\,(g)} \rightarrow CO_2\text{, via } C(O_2) \quad (2.15)$$

where *C denotes a free carbon site active surface carbon, while $C(O_2)$ is a dioxygen surface complex, instable at high temperatures (>600 K) and C(O) a stable surface species. Slow transformation in between the surface species has also been also suggested, resulting in the coupled reaction step in equation 2.16:

$$2\ *C + O_{2(g)} \leftrightarrow 2\ C(O) \quad (2.16)$$

Gaseous CO and CO_2 are generally described originating from surface oxides desorption, both as equilibrium steps, or combined desorption and oxygenated surface species formation. Direct interaction in between surface carbon and oxygen has been considered, too. [22] Also, interactions in between surface species have been included among the possible steps in the oxidation mechanism.

Carlsson has developed an extended reaction mechanism, speculating the effect of additional reactive pre-adsorbed oxygen species and reactive carbon species [22].

Briefly, the presence of different types of carbon sites having different stabilities and reactivities has been detected with the formation of different types of oxide complexes and functional groupings having different stabilities and reactivities. These surface species can migrate, diffuse, interact with gaseous oxygen or with each other. Distribution in activation energy has been conjectured by Campbell and Mitchell [23] for characterization of surface species. The study has also determined the need for a minimum of four-site approximation of distribution in order to get significant result from the proposed detailed kinetic model.

Reaction mechanism with NO_2 and soot has been studied alone and in combination with O_2. Also, the effect of NO and NO_2O has been investigated in the NO_x oxidizing mixture. For brevity, here the results with NO_2 and O_2 only are presented.

It is significant to underline that a common trait in between the authors is the enhancement of NO_2-aided oxidation in the presence of O_2.

Setiaboudi and co-workers [24] have analysed combined O_2 and NO_2 oxidation and have implemented the reaction steps in equation 2.17-2.18 for taking into consideration NO_2 effect:

$$*C + NO_{2\,(g)} \leftrightarrow C(O) + NO \tag{2.17}$$

$$CO + NO_{2\,(g)} \rightarrow C(O)(O) + NO \tag{2.18}$$

where C(O), C(O)(O) are surface oxide complexes.

Clarification for the proposed reaction mechanism is also provided. Oxide complexes which are present on diesel soot are generally unreactive to oxygen. NO_2-soot reaction forms of oxygen-containing intermediates. O_2 reacts with the NO_2-generated intermediates, yielding less stable intermediates or directly producing gaseous CO and CO_2. C(O)(O) species is considered to be relatively unstable.

Jeguirim *et al.* [25] have proposed for NO_2 adsorption and interaction with pre-adsorbed surface oxide complexes the two additional steps of equations 2.19-2.20

$$*C + NO_{2\,(g)} \rightarrow C(NO_2) \tag{2.19}$$

$$C(O) + NO_{2\,(g)} \rightarrow C(ONO_2) \tag{2.20}$$

The last reaction represents O_2-NO_2 cooperative effect. Gaseous CO and CO_2 derive then directly from surface species $C(ONO_2)$.

Muckenhuber and Grothe [26] have also reported from spectroscopic analysis the presence of the mixed complex C(ONO) deriving from NO_2 direct adsorption on a vacant site.

In GT-SUITE model, a three-step semi-global mechanism involving a single surface species has been applied. A single type of carbon site is used in the description of the carbon surface. Detailed discussion of the reaction mechanism implementation is provided in the section below.

2.3 Literature Overview

Pioneer work on uncatalyzed O_2 soot oxidation has been carried out by Neeft *et al.* [16]. A global reaction mechanism was proposed, with parameters fitting experimental data. Reaction order was found to be close to 1 for oxygen and range of 0.65-0.80 when synthetic soot was examined. The presence of water vapour was also considered as influencing factor on CO/CO_2 selectivity. Despite the application of global kinetics, the authors pointed out that models relating the evolution of carbon specific surface area to conversion are too simple if an accurate description of the complex phenomena is desired. Indeed, carbon available surface area is likely to increase with conversion due to opening of occluded pores as a consequence of hydrocarbons desorption or partial oxidation and the reaction is reported to take place not only on the surface, but throughout the entire particle. Previous TEM analysis on soot morphology change during oxidation was carried out by Ishiguro *et al.* [27].

Messerer *et al.* [17] provided a comprehensive Langmuir-Hinshelwood model for real soot oxidation with NO_2 and O_2 under the whole range of typical conditions for the exhaust. A kinetic model based on parallel reactions operated by O_2 and NO_2 without non-linear interferences at the surface was defined. Reported activation energy values separate adsorption for O_2 40-50 $kJmol^{-1}$ and 100-110 $kJmol^{-1}$ for the chemical reaction. Shrinking core model was considered consistent with experimental data.

Jung *et al.* [28] reported a uniform spherule shrinkage, establishing soot as non-porous to O_2. Thighe *et al.* [29], in analysing soot oxidation by NO_2 determined the equivalence of oxidation throughout a soot porous particle with reasonably neglected mass transfer or on the exterior of a porous particle. Representation of soot as one porous particle is assumed to be equal to the model of an ensemble of tiny spherules burning independently.

Controversy therefore arises on whether shrinking core model can provide significant results from kinetics modeling. Comparing NO_2 and O_2 oxidation mechanisms, Strzelec *et al.* [30] showed that NO_2 reacts immediately in contact with the surface while O_2-aided oxidation is in total slower due to solid-phase diffusion through the pores. The difference arises from the oxidant attack mechanism to soot nanostructure, resulting in predominant external oxidation for NO_2 and internal oxidation for O_2. Therefore, shrinking core model prediction is good for NO_2 reaction only, where diffusion through the pores is neglected.

Based on this result, the reaction mechanism for O_2-NO_2 mixtures has been analysed by Seong and Choi [31], establishing that NO_2 species leads the oxidation pathway.

From experimental observation, Echavarria *et al.* [32] have examined the process of soot primary particle fragmentation, describing it as a consequence of simultaneous internal burning and preferential burning on the so-called bridge sites, or necks in between primary particles. Internal burning behaviour and the importance of soot nanostructure have been investigated trough high resolution transmission electronic microscopy (HR-TEM).

So far, uncatalyzed reaction mechanism has been discussed. DPF is however often coated in order to achieve regeneration during engine normal operations. Ceria (CeO_2) has shown catalytic activity for soot oxidation and activity can also be tuned according to the catalyst structure. [33] Pt can be added to the Ceria catalyst to increase CO_2:CO ratio. Further details on catalytic soot oxidation are discussed in a dedicated chapter.

2.4 GT-SUITE Kinetic Model

GT-SUITE is a powerful tool for aftertreatment simulations since it provides the user a comprehensive fluid dynamics model for flow and reactions. Templates are available for real-system components. However, practical limitations have been faced in reactions implementation.

The purpose was to develop a software representation of the laboratory setting in a sufficiently simple manner without losing accuracy for results. The model consists plainly in a continuous flow fed to the DPF filter with pre-loaded soot.

Regeneration reactions are defined in a dedicated SurfaceReactions template, with the possibility of separate implementation for soot cake layer and substrate wall layer. For heterogeneous reactions, solid phase contains the available sites for the reaction. If present, catalytic sites can be defined with fixed site density, while for soot reactions, carbon species is considered both as a site for reaction and as a reactant, with concentration changing during the reaction.

Reactions implemented in the soot cake require soot as one of the reactants, no adsorption/desorption of surface species is allowed. Surface reactions not involving soot are allowed in substrate wall layer. The oxidation reaction scheme has needed therefore some elaboration before being used in the model. The first idea with these premises was the implementation of the entire reaction scheme in the wall layer, redistributing soot loading entirely in the porous wall. However, filter porosity and permeability defined with the analysis on clean filter prevent from non-reasonable excessive soot loading in substrate wall layer.

An opportune strategy has been elaborated to overcome this limitation. Cake layer soot is oxidized to a gaseous species which is adsorbed in substrate wall layer. Surface reactions and desorption of the oxidation products are implemented too in the substrate wall layer. Again, definition of the gaseous species that needs to be adsorbed is not straightforward. Ideally, the species chemical formula would be CO, but distinction from the CO, product of the oxidation reaction, is required. A dummy species $COAr_{0.5\ (g)}$ has been defined with CO thermodynamically properties and molecular weight of 48. Also, stoichiometry and mass balance need to be adjusted in the reactions. Definition of soot is modified accordingly, thus becoming a 32-molecular weight species, and soot loading is opportunely scaled with 32/12 factor.

The implemented reaction scheme in particulate filter model is presented below (equations 2.21-2.26).

Soot cake layer reactions

$$\text{soot}_{(s)} + 0.5\ O_{2\ (g)} \rightarrow COAr_{0.5\ (g)} \tag{2.21}$$

$$\text{soot}_{(s)} + NO_{2\ (g)} \rightarrow COAr_{0.5\ (g)} + NO_{(g)} \tag{2.22}$$

Substrate wall layer reactions

$$COAr_{0.5\ (g)} \rightarrow CO_{ads} + Ar_{0.5\ (g)} \tag{2.23}$$

$$CO_{ads} \rightarrow CO_{(g)} \tag{2.24}$$

$$CO_{ads} + 0.5\ O_{2\ (g)} \rightarrow CO_{2\ (g)} \tag{2.25}$$

$$CO_{ads} + NO_{2\ (g)} \rightarrow CO_{2\ (g)} + NO_{(g)} \tag{2.26}$$

Soot oxidation to $COAr_{0.5\ (g)}$ species is implemented in cake layer. $COAr_{0.5\ (g)}$ is adsorbed in substrate wall layer with gaseous 20-molecular weight $Ar_{0.5}$ release. Carbon surface site Z/Z_{CO} is identified in substrate wall layer, with relative coverage characterization. Initial coverage is equal to 1 for the empty surface site Z, while for the surface site Z_{CO} filled with the adsorbed species it is equal to 0.

The implemented kinetics in particulate filter model is presented below (equations 2.27-2.32).

Soot cake layer kinetics

$$r_1 = A_1 \cdot e^{\frac{-Ea_1}{T}}[O_2]^{0.8}[C]^{2/3} \tag{2.27}$$

$$r_2 = A_2 \cdot e^{\frac{-Ea_2}{T}}[NO_2][C]^{2/3} \tag{2.28}$$

Substrate wall layer kinetics

$$r_3 = A_3 \cdot [COAr_{0.5}] \cdot \theta_Z \tag{2.29}$$

$$r_4 = A_4 \cdot e^{\frac{-Ea_4}{T}} \cdot \theta_{CO} \tag{2.30}$$

$$r_5 = A_5 \cdot e^{\frac{-Ea_5}{T}} \cdot [O_2] \cdot \theta_{CO} \tag{2.31}$$

$$r_6 = A_6 \cdot e^{\frac{-Ea_6}{T}} \cdot [NO_2] \cdot \theta_{CO} \tag{2.32}$$

where θ_Z and θ_{CO} are the surface coverages and [C] is defined as mass of loaded soot per unit reactor volume (g/l).

Previous work carried out on the same experimental data had the purpose of developing a global kinetic mechanism. 0.8 reaction order has been determined for oxygen and 1 for nitrogen dioxide. Shrinking core model has been applied, the reaction rate expression resulting in the equation 2.33. [34]

$$-\frac{dC}{dt} = A \cdot e^{-\frac{E_a}{RT}} \cdot [O_2]^{0.8}[NO_2] \cdot m_{C,0}(1-\xi)^{2/3} \tag{2.33}$$

Arrhenius plots for the examined experiment are presented in Appendix B.

For the detailed mechanism proposed in the model, steps 2.21 and 2.22 have been considered to be rate-determining.

The influence of upstream DOC on theoretically calculated kinetic parameters has also been investigated. Activation energy for DPF oxidation reactions is increased if upstream DOC is present. DOC removes HC from exhausts HC and CO oxidising them to CO_2, resulting in an increased soot loading. Activation energy is increased, attesting lower reactivity, since less hydrocarbons are adsorbed on soot. Selectivity in between CO and CO_2 is also affected, as CO amount is higher when DOC is present (lower amount of adsorbed hydrocarbons). Long loading results in a lower overall reactivity, internal mass transfer resistance effect has been blamed.

The use of a soot population balance for differently aged PM is also suggested from this analysis. [34]

2.4.1 Numerical Solver

Solver for chemical reactions in the SurfaceReaction template has been selected in between the ones provided.

2.4.1.1 BDF Solver

ParticulateFilter template with activated diffusion model forces the use of Backward Differential Formulation (BDF) implicit robust ODE solver, which is able to handle stiff ODE problems. Tolerances are set to default values.

For each time step, the solver first calculates the flow along the channel length with quasi-steady state assumption. From pressure, temperature and velocity solutions, soot mass retained in the filter and species concentrations are calculated using the ODE solver. Thermal properties for the soot cake layer are set to default values.

Diffusion model is activated. Diffusion is taken into account in inlet and outlet channels, soot cake layer and wall. Soot cake layer is discretized in 10 intervals (default value). The diffusion model uses quasi-steady state mass transfer model. Effective diffusivity is calculated based on mixture diffusion model. Equations for channel, soot cake layer, and wall layer are solved in a coupled way. [35]

3. Catalyst Effect

As previously mentioned, diesel particulate filter regeneration is achieved through soot oxidation. Passive regeneration technique employs a catalyst in order to decrease the activation energy needed for regeneration reaction and therefore meet the required temperature during engine normal operations.

Among the possible oxidation catalysts, CeO_2 has shown good performances at lower costs. Therefore, intense research is being carried out in order to increase the catalyst performances. Ceria is able to store and release oxygen, due to the cerium peculiar property to switch in between Ce^{4+} and Ce^{3+} oxidation states introducing oxygen in the crystalline structure. Two mechanisms through which the catalytic action takes places have been identified, the so-called "active oxygen" and "NO_2-assisted" mechanisms, as summarized in figure 3.1.

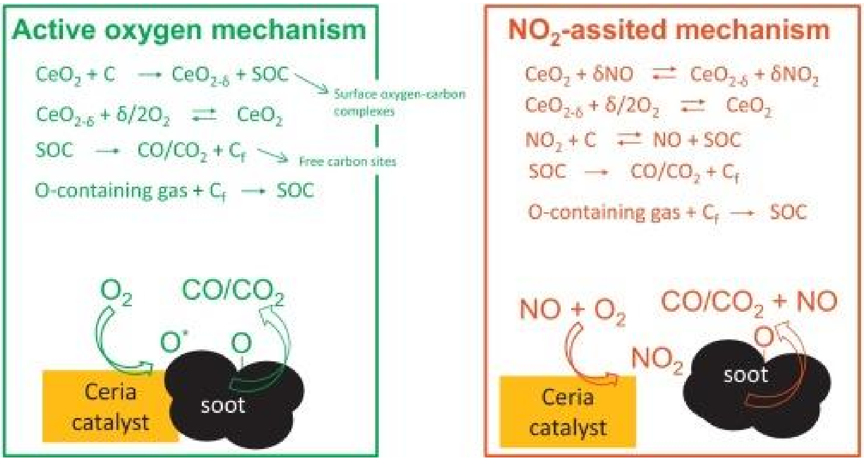

Figure 3.1. Scheme of ceria-catalysed soot oxidation mechanism, from [35].

In O_2-rich exhaust, exchange in between CeO_2 and gas phase oxygen occurs, forming highly reactive oxygen species for soot oxidation. At temperatures above 300 °C, ceria catalyses NO oxidation to NO_2, with the creation also in this case of surface oxygen-carbon complexes. Doping ceria with suitable cations (La^{3+}, $Pr^{3+/4+}$, Zr^{4+}) increases thermal stability, oxygen storage capacity and oxygen mobility. Nevertheless, some side-effects should be considered when changing CeO_2 physicochemical properties. [36]

The main factors affecting pure and doped ceria activity have been identified as surface area/crystal size, surface composition and surface properties. Higher surface area is favourable for NO oxidation to NO_2 and active oxygen transfer.

The entity of catalyst-soot contact is also of great importance. In general, "loose" and "tight" contact conditions can be obtained through different catalytic preparation techniques, the second being more favourable for the oxidation reaction. However, "tight" contact is also less representative of the real contact conditions since catalyst and soot particles dimensions can be significantly different. [10]

The catalyst shape also affects catalyst-soot contact. The influence of topological and textural properties of several nanostructures has been studied by Piumetti *et al.* [33], resulting in the role of the highly reactive surfaces (110) and (111), abundant in nanocubic structures. In another study, temperature is considered to be directly related to the surface-sensitivity to the reaction [37].

3.1 Precious Metals

Platinum-group metals (PGMs) are widely employed as oxidation catalysts in the automotive sector. Platinum is used in diesel oxidation catalyst, three-way converter and lean NO_x trap, for instance.

Concerning DPF system, Pt acts not only on soot oxidation reaction directly, lowering activation temperature at 250-350 °C, but also on CO and NO oxidation intermediate reactions. Pt catalytic effect for CO oxidation to CO_2 is strongly related to the morphology of the support. Contrarily, NO Pt-catalysed oxidation is still enhanced but poorly affected by the support.

Pt/CeO_2 soot oxidation has been described acting through three steps:

- O_2 dissociative adsorption on two Pt adjacent active sites
- oxygen spillover from Pt sites to CeO_2 surface
- reaction in between soot and active oxygen species.

Pt intervenes in capturing and transferring oxygen from the bulk phase to ceria surface. Also, when analysing soot oxidation in the absence of NO, structure-dependence (support) is predominant, making Pt catalytic activity less significant than morphology. [38]

The redox mechanisms involving CeO_2 and Pt during soot oxidation are schematized in figure 3.2. It can be seen that, in the contemporary presence of O_2 and NO_2, ceria stores NO_2 in the form of nitrates below 400 °C, which are then released at higher temperatures. [10]

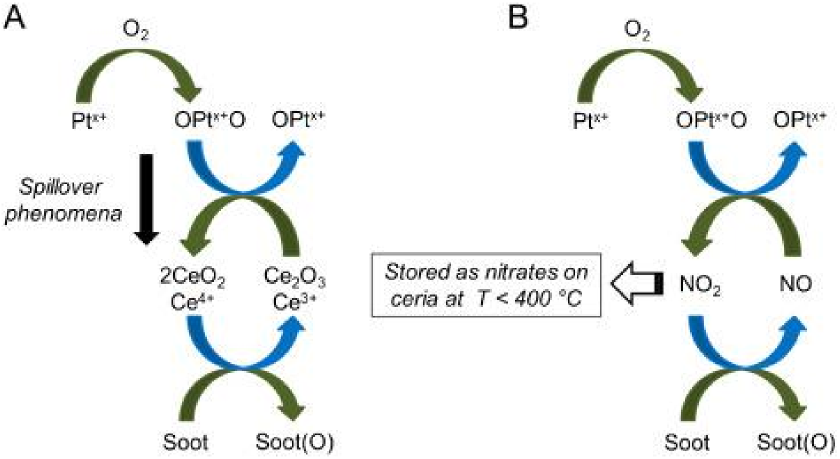

Figure 3.2. Scheme of Pt/CeO_2-catalyzed O_2 (figure A) and NO_2 (figure B) soot oxidation mechanism [10].

If great effort was put in order to elaborate an effective kinetic mechanism for uncatalyzed soot oxidation, detailed kinetics has not been reported yet for the catalytic reaction, due to the high complexity of the system analysed.

4. ParticulateFilter Governing Equations

The governing equations for the flow model provided by Gamma Technologies are listed below (equations 4.1-4.5). [35]

4.1 Mass and Heat Transport

Solid phase energy

$$\psi_s \frac{\partial T_s}{\partial t} = \frac{\partial}{\partial z}\left(f_{sb}\lambda_{sb}\frac{\partial T_s}{\partial z}\right) + hS\left(T_g - T_s\right) - \sum_{j=0}^{nrct} \Delta H_j\, r_j + \frac{P}{V} + h_x S_x (T_x - T_s) \qquad (4.1)$$

Gas phase energy

$$\epsilon \rho_g v C_{pg}\frac{\partial T_g}{\partial t} = hS\left(T_s - T_g\right) \qquad (4.2)$$

Continuity

$$\frac{\partial}{\partial t}\left(\rho_g v\right) = 0 \qquad (4.3)$$

Momentum

$$\epsilon\frac{\partial p}{\partial z} + \epsilon\rho_g v\frac{\partial v}{\partial z} = -Sf_f\frac{1}{2}\rho_g v^2 \qquad (4.4)$$

Mass

$$\epsilon\rho_g v\frac{\partial \omega_g}{\partial z} = k_{m,i}S\left(\omega_{s,i} - \omega_{g,i}\right) \qquad (4.5)$$

Nusselt number (equation 4.6) and friction factor (equation 4.7) for the wall-flow monolith are determined assuming fully-developed laminar flow in squared channels with solid impermeable walls.

$$Nu = 2.98 \qquad (4.6)$$

$$C_f Re = 14.2 \qquad (4.7)$$

Heat and mass transfer coefficients are related to Nusselt and Sherwood number, respectively (equations 4.8-4.9).

$$h = Nu\frac{\lambda_g}{D_h} \qquad (4.8)$$

$$k_{m,i} = Sh\frac{\rho_g D_{i,m}}{D_h} \qquad (4.9)$$

Reaction-diffusion modeling is obtained with definition of species effective diffusivity coefficient D_{eff} as in equation 4.10.

$$\frac{1}{D_{eff,i}} = \frac{\tau}{\epsilon}\left(\frac{1}{D_{m,i}} + \frac{1}{D_{Knudsen,i}}\right) \qquad (4.10)$$

List of symbols
ψ_s = effective heat capacity of reactor [J/m^{3}K]
T_s = temperature of gas at catalytic surface [K]
z = axial length [m]
f_{sb} = solid fraction of substrate
λ_{sb} = thermal conductivity of substrate [J/msK]
h = heat transfer coefficient [W/m^{2}K]
S = surface area per reactor volume [m^{-1}]
T_g = temperature of bulk gas in reactor channels [K]
ΔH_j = enthalpy of reaction j [J/mol]
r_j = reaction rate of reaction j [mol/m^{3}s]
P = power input [J/s]
V = reactor volume [m^3]
h_x = external heat transfer coefficient [W/m^{2}K]
S_x = external surface area per reactor volume [m^{-1}]
T_x = external temperature [K]
ϵ = void fraction of reactor
ρ_g = density of bulk gas in reactor channels [kg/m^3]
v = velocity [m/s]
C_{pg} = heat capacity of gas [J/kgK]
p = pressure [Pa]
$\omega_{g,i}$ = mass fraction in bulk phase of species i
$\omega_{s,i}$ = mass fraction at the surface of species i [W/m^{2}sK]
$k_{m,i}$ = mass transfer coefficient for species i [kg/m^{2}K]
Nu = Nusselt number
λ_g = thermal conductivity of gas [J/msK]
D_h = reactor hydraulic diameter [m]
Sh = channel Reynolds number
C_f = skin friction coefficient
$D_{eff,i}$ = effective diffusion coefficient for species i [m^2/s]
τ = tortuosity, $\tau = 3$
$D_{m,i}$ = mixture diffusion coefficient for species i
$D_{Knudsen,i}$ = Knudsen diffusion coefficient for species i

4.2 Pressure Drop

Pressure drop model is based on wall-flow filter with symmetric channels. Collection model in soot filtration allows to describe soot loading with changed properties for loaded filter and soot cake formation.

Pressure drop is calculated from seven different contributions, presented in equations 4.11-4.16: contraction, friction in inlet channel, soot cake layer, ash layer, filter wall, friction in outlet channel and expansion. For the developed model, the presence of ash has been neglected and therefore ash model has not been activated ($\Delta P_4 = 0$). The location of the pressure drop contributions is schematized in figure 4.1. It is important to point out that, in real cases, as a consequence of ash accumulation in the filter, effective filtration length is reduced. The parameters that appear in the equations have been tuned according to clean filter measured pressure drop.

The expressions listed below are valid for symmetric channel configuration and 0D model, extension to 1D model is obtained through axial integration. [35]

Contraction

$$\Delta P_1 = \frac{\xi_{contraction}\rho_{in}U_{in}^2}{2} \tag{4.11}$$

Friction in the inlet channel

$$\Delta P_2 = \frac{\mu Q}{2V_{trap}}(D + w_{wall})^2 \frac{4FL^2}{3(D-2w_{soot})^4} \tag{4.12}$$

Soot cake layer

$$\Delta P_3 = \frac{\mu U_{w,1}(D-2w_{soot})}{2k_{soot}} \ln\left(\frac{D}{D-2w_{soot}}\right) + \beta_{soot}\rho w_{soot}U_{w,1}^2 \tag{4.13}$$

Filter wall

$$\Delta P_5 = \sum_i \left(\frac{\mu U_{w,2}w_{slab,i}}{k_{wall,i}} + \beta_{slab}\rho w_{slab,i}U_{w,2}^2\right) \tag{4.14}$$

Friction in the outlet channel

$$\Delta P_6 = \frac{\mu Q}{2V_{trap}}(D + w_{wall})^2 \frac{4FL^2}{3D^4} \tag{4.15}$$

Expansion

$$\Delta P_7 = \frac{\xi_{expansion}\rho_{out}U_{out}^2}{2} \tag{4.16}$$

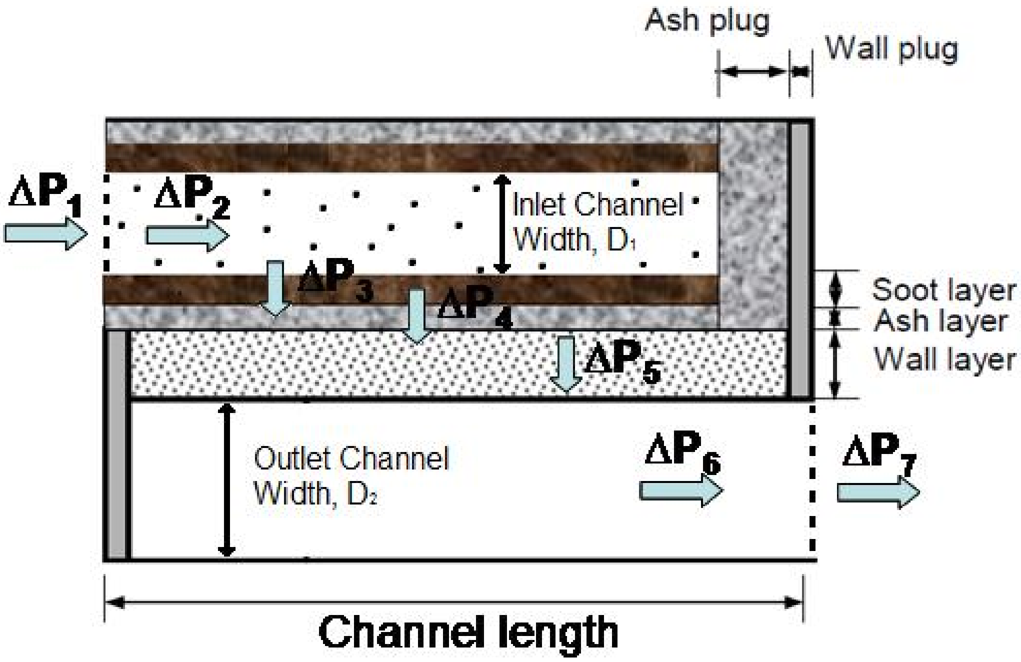

Figure 4.1. Pressure drop individual contributions in single channel DPF, adapted from [35].

Gas flow through porous wall is generally described with Darcy´s law, delineating a velocity linear dependence for pressure drop. In the case of high filtration velocity, an extra quadratic term considers local flow inertial losses. Parameters permeability *k* and Forchheimer coefficient *β* therefore describe completely the flow.

List of symbols

$\xi_{\mathrm{contraction}}$ = contraction pressure drop coefficient

$\xi_{\mathrm{expansion}}$ = expansion pressure drop coefficient

ρ_{in} = gas density at inlet [kg/m^3]

ρ_{out} = gas density at outlet [kg/m^3]

ρ = gas density in filter [kg/m3]

U_{in} = inlet gas velocity [m/s]

U_{out} = outlet gas velocity [m/s]

$U_{\mathrm{w,1}}$ = soot layer inlet velocity [m/s]

$U_{\mathrm{w,2}}$ = substrate wall velocity [m/s]

μ = gas viscosity [Pa·s]

Q = inlet volumetric flow rate [m^3/s]

V_{trap} = total filter volume [m^3]

D = channel width [m]

w_{soot} = soot cake layer thickness [m]

w_{wall} = substrate filter wall thickness [m]

F = channel pressure drop correlation, for laminar flow in square channel, $F=28.454$

L = channel length [m]

k_{soot} = soot cake layer permeability [m^2]

β_{soot} = Forchheimer constant in soot cake layer [1/m]

β_{wall} = Forchheimer constant in substrate wall layer [1/m]

$w_{slab,i}$ = thickness of each discretized slab in the filter substrate layer [m]

$k_{slab,i}$ = loaded filter substrate wall permeability of discretized slab i [m^2]

i = filter wall discretization interval number

4.3 Flow Solver

For stand-alone exhaust aftertreatment models, quasi-steady state flow solver is selected in order to reduce computational time using large time steps, as longer time scale analysis is feasible compared to engine simulation.

Quasi-steady state approximation allows to replace substantial derivative with spatial derivative. Residence time of the gas in the reactor is in fact considerably lower compared to other time scales. The user is able to define master time step for the simulation, inside the quasi-steady state solver features. In general, a reasonable choice for master time step is a value lower or equal to the frequency of measured data. 1 s has been chosen as it roughly corresponds to the frequency of the input data. When chemical reactions are present, sub-time-stepping is considered internally for every chemistry solver.

5. Methods

The present work is part of a more extensive project on diesel particulate filter analysis, bridging laboratory and real-engine size scales.

5.1 Preliminary Work

The first part of the project consisted in the elaboration and in the execution of experiments for the investigation of different parameters on soot loading. A peculiar experimental asset was elaborated specifically in order to obtain a comprehensive description over the problem. Small DPFs were cut from full-size filters. Uncoated cordierite, uncoated SiC, CeO_2 coated SiC and Pt and CeO_2 coated SiC substrates have been employed. The small reactors were mounted on steel tubes and assembled into four cartridges with 6 mini-DPFs each. Experimental sampling setup for one cartridge is shown in figure 5.1.

Filter loading was performed with a full-size engine. 11L Eu6 eSCR heavy duty diesel engine with Euro VI diesel fuel was employed on the test bench. Different loading conditions corresponded to short/long cycle and eventual presence of an upstream DOC.

A combination of steady state operation and transient cycle for the engine was used, the number of repetitions being different for short and long loading case. The cartridge containing the mini-DPFs was mounted in parallel to a full-size DPF. Weighting of the samples at the end of the procedure gave the loaded particulate amount for DPF.

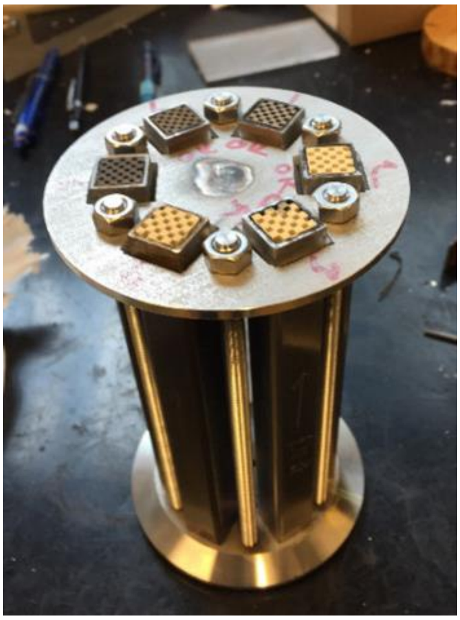

Figure 5.1. One cartridge containing six mini-DPFs employed in the experiments.

The geometrical characteristics of the different substrates are resumed in table 5.1.

Table 5.1. Geometrical characteristics of the different substrates.

Substrate	Cell Density (cpsi)	Length (in)	Wall (milin)	Washcoat (µm)	Pt (g/ft^3)
Cordierite	200	6	12	0	0
SiC	300	6	10	0	0
CeO_2/SiC	300	6	10	50	0
Pt/CeO_2/SiC	300	6	10	50	40

Uncoated cordierite and SiC filters are examples of uncatalyzed substrates. They have been studied as probe substrates in order to build the DPF model. The other substrates can be used with proper tuning for model validation.

In the second step of the project, a set of 27 different oxidation experiments was carried out on the loaded mini-DPFs. Each loaded mini-DPF was identified with a numerical code (1 to 27), corresponding to specific substrate and applied loading characteristics. Table 5.2 summarizes the coding system.

Table 5.2. Clarification on the coding system used for the oxidation experiments according to substrate nature and soot loading conditions.

	Cordierite	SiC	CeO_2/SiC	Pt/CeO_2/SiC	
Long loading	14	12	11,13	15	w DOC
	1,2,3	26	4	27	no DOC
Short loading	25	21,24	22	23	w DOC
	20	19	18	16,17	no DOC

Each mini-DPF was transferred into an oven. Temperature was gradually increased from room temperature to 400 °C, and, through subsequent 50 °C steps, to 600 °C.

A constant flow rate of 1.978 l/min was set for the feed, with N_2 as main component, to which pulses of air and 0.5% NO_2/99.5% Ar mixture was added. Total oxidation of the loaded soot was desired and in the last part of the experiments a great amount of air was flushed. At 600 °C, pressure drop measurements with varying total flow rates were carried out. The reactor was then left cooling down at ambient temperature.

5.2 Input Data Description

Temperature, pressure drop and outlet CO, NO_x and CO_2 sensors were used to collect relevant data during the experiments.

Inlet oxidant flows were applied through mass flow controllers. The effect of the oxidants was analysed at high and low concentration levels through subsequent steps. Volumetric flow values were set to reach 1000 and 4000 ppm for oxygen and 400 and 800 ppm for nitrogen dioxide. The pulse sequence is represented in the figure 5.2 for two specific temperature levels with data from experiment no.12. Oxygen level is gradually increased throughout three steady states when no nitrogen dioxide is present. Nitrogen dioxide is then fed at two different levels in combination with all the oxygen levels and alone. Oxygen-only feed is again applied at two different levels.

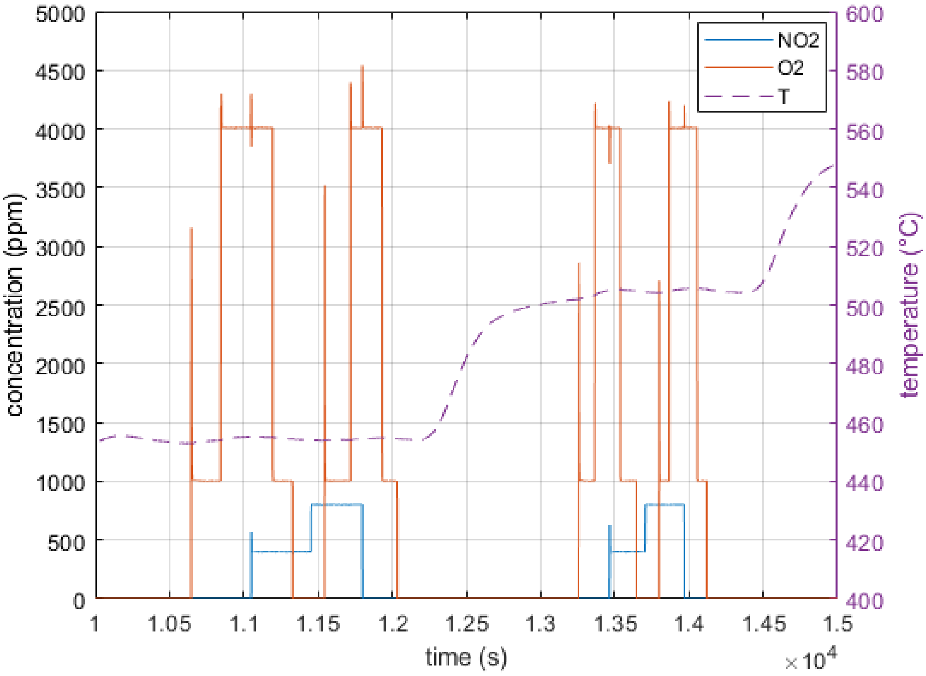

Figure 5.2. Zoom of oxidant levels injection at two different temperatures, filter #12.

A wrong calibration of the flow rate provided at the inlet through the mass flow controllers led to miscalculations in the set values, resulting in the application of slightly different levels for the oxidants from the experiment no.13 onward. This error could have affected the theoretical calculation of the kinetic parameters for oxidation reactions, however the experiment used for developing the software-based kinetic model has been selected properly in order to have the desired values for the levels of the oxidants.

5.2.1 Filter #12

Among all the experiments performed, experiment no.12 has been chosen to build the model. The concentration profiles are sufficiently smooth and the operating conditions range is broad so that it has been considered a good candidate for parameter estimation. Long loading and no upstream DOC are the soot loading characteristics for the uncoated SiC filter.

The temperature profile in figure 5.2 shows two distinct phases occurring in the experiment development, each one approximately corresponding to half of the total time duration. Temperature is ramped from ambient level, then stepped until 400 °C as described previously and finally decreased until ambient temperature level is reached again. This phase corresponds to the system cooling down. Temperature is again increased and subsequent steps are analysed at 400 °C, 600 °C, 500 °C and 650 °C. Through each step, the oxidants pulse sequence is applied.

Since the first half of the experiment is considered to be representative enough for the reaction temperature analysis, the model formulation has been realized on the first 19500 s, used for parameter estimation. In this way, the software total computational time is also decreased. During the tuning of kinetic parameters, the first 8000 s of the simulation have been excluded, as the temperature profile trend in the time interval 8000-19500 s in figure 5.3 is suitable for such analysis.

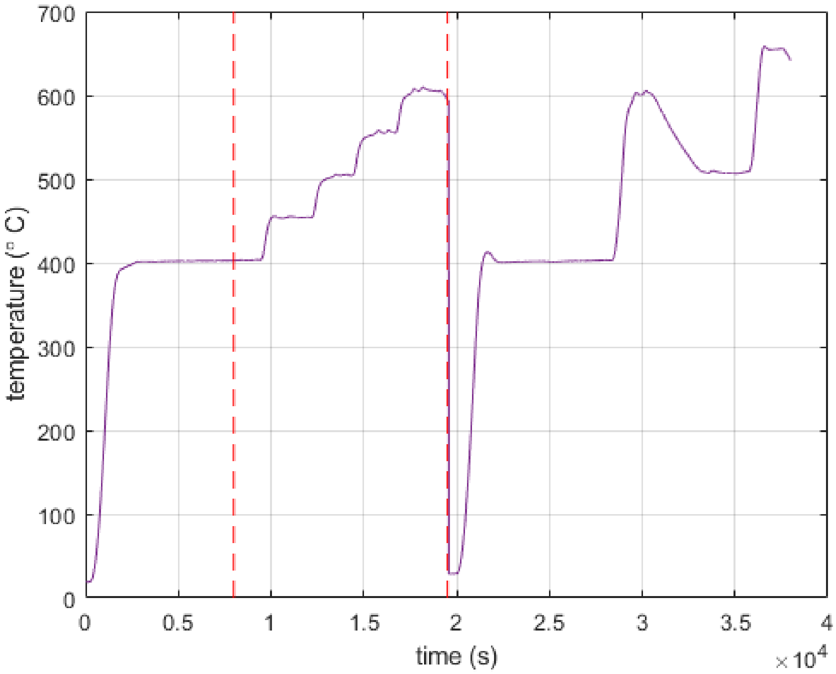

Figure 5.3. Temperature profile for filter #12 registered by a thermocouple placed approximately at the centre of the reactor. The selected time interval for model definition is highlighted.

Inlet oxygen and nitrogen dioxide inlet volume flows are plotted together for the first half of the experiment in figure 5.4.

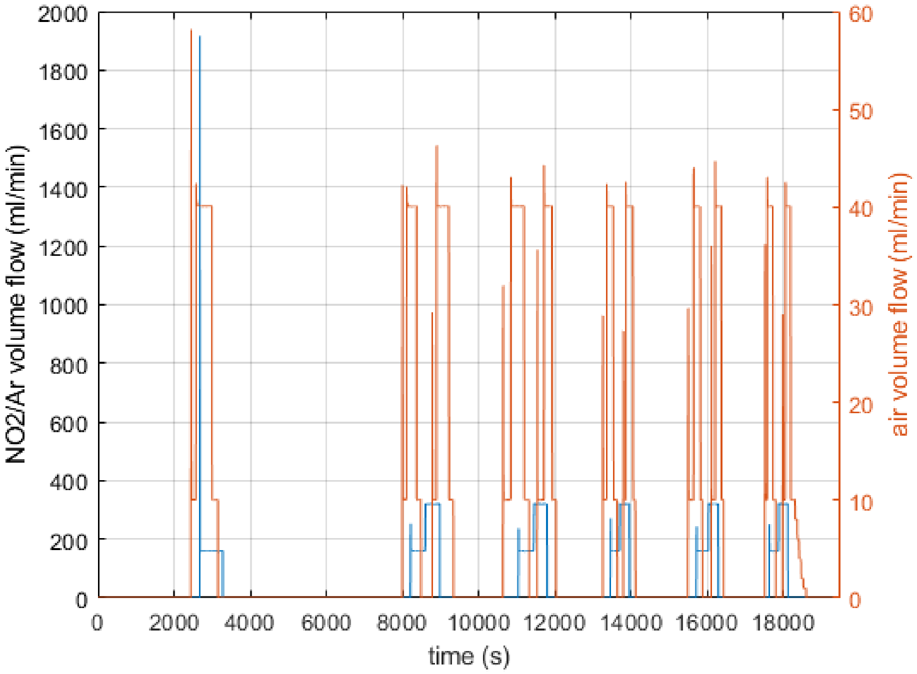

Figure 5.4. Inlet oxidant flow rates, filter #12.

The flow rate profiles show spikes at the beginning of the injections due to inertial effects when mass flow controllers are opened. The first spike is particularly high when NO_2/Ar mixture is injected (almost doubling the total inlet flow rate). These abrupt changes in composition are at the origin of instability for the model, increasing the complexity in computation.

The programmed sequence of oxidants injection is applied regularly after approximately 8000 s.

Due to the sudden changes in composition, total inlet gas flow rate is not exactly constant to 1.987 l/min value. Also, at the end of the experiment different total flow rate values have been applied flushing air into the system. The single flow rates registered by the mass flow controllers have been summed in plot in figure 5.5.

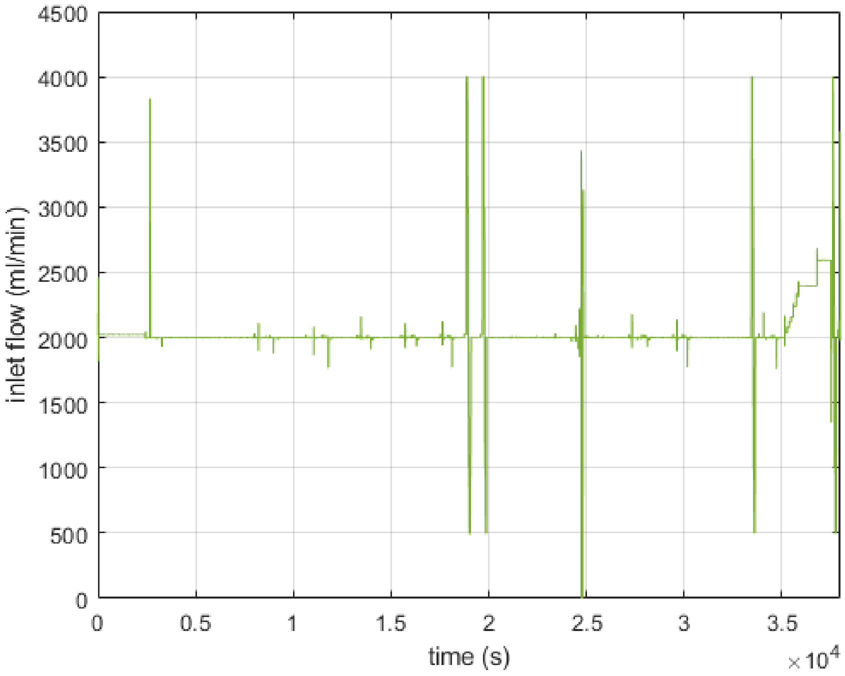

Figure 5.5. Calculated total gas inlet flow rate, filter #12.

CO, NO_x and CO_2 outlet concentrations were registered and the resulting signals were smoothed. Interpolation in the smoothed signals has been carried out in order to reduce the error due to experimental data scattering while estimating kinetic parameters.

From integration of the CO and CO_2 emitted amounts, soot mass and DPF loading were calculated with the assumption of 100% conversion according to the equations 5.1 and 5.2.

$$m_C = \int_0^N 12 \cdot (CO + CO_2)_{ppm} \cdot 10^{-6} \cdot q \frac{101325}{298R} dt \tag{5.1}$$

$$\text{loading} = \frac{m_C}{V} \tag{5.2}$$

The soot amount in the first column in table 5.3 has been introduced in the mini-DPF model, with an opportune scaling factor, as explained in the previous section.

Table 5.3. Soot mass and DPF loading for filter #12.

Soot mass (g)	Soot loading (g/l)
0.2048	9.32

An important indicator for the model effectiveness is the good prediction of the oxidation advancement through soot conversion. It can be seen in figure 5.6 that roughly half of the soot is converted in the first half of the experiment. The steps in soot conversion profile correspond to the oxidant injection intervals.

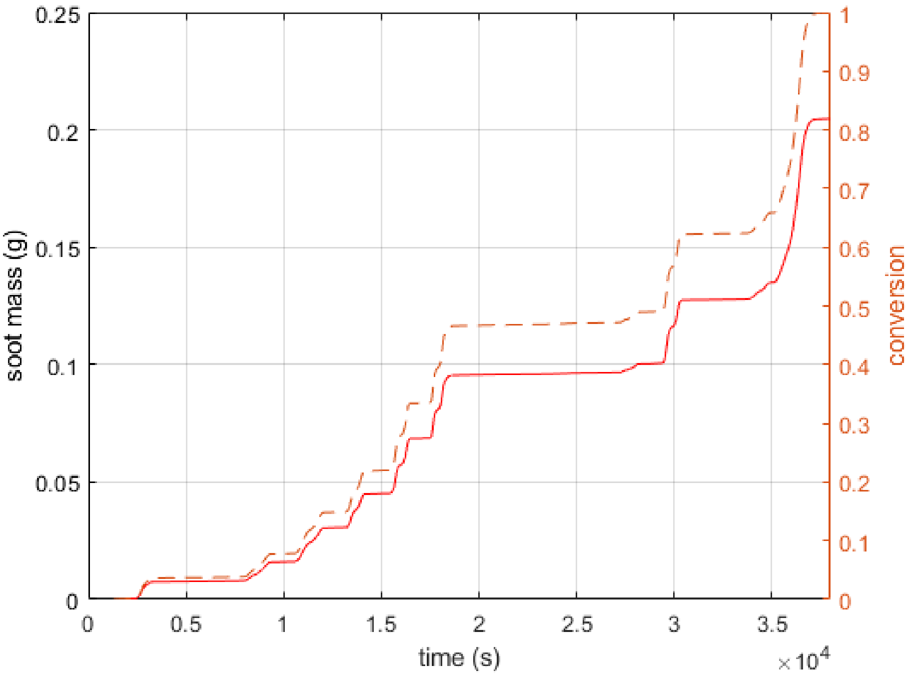

Figure 5.6. Soot mass conversion profile.

5.3 Model Description

A picture of the comprehensive model for DPF regeneration is provided in figure 5.7.

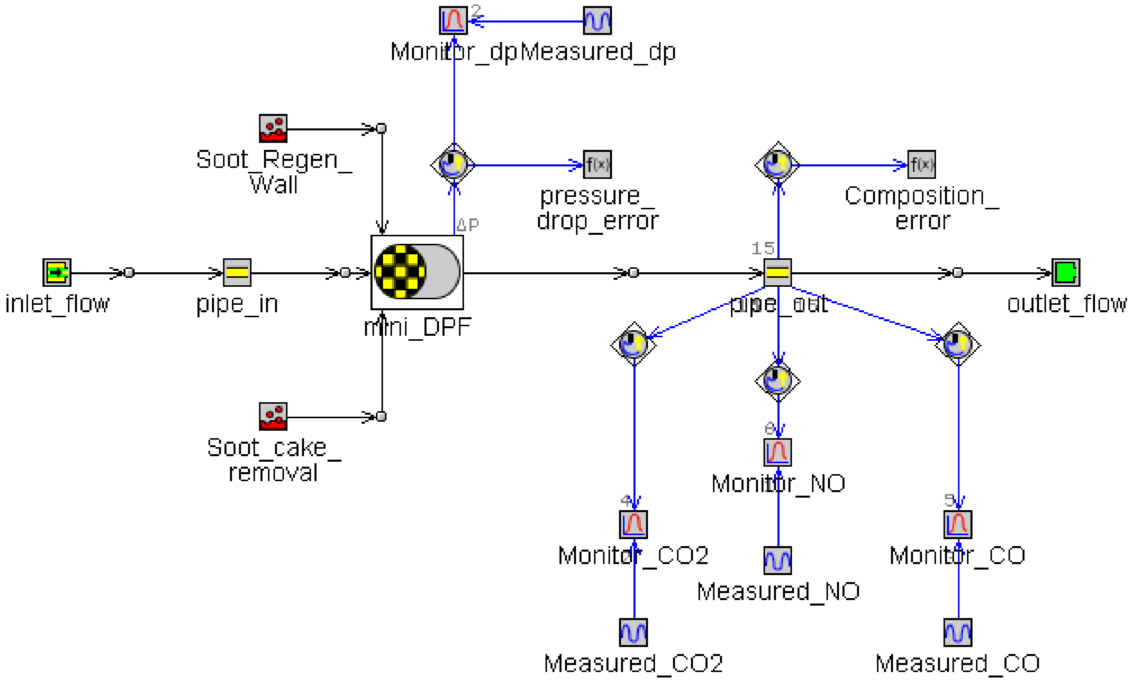

Figure 5.7. GT-SUITE model for mini-DPF.

ParticulateFilter template provided by GT-SUITE has been employed in the model. Only one pair of channels is modelled, being representative for all the filter channels. The user is able to define a specific geometry for the filter, the number of channels, filter diameter, channel length and wall thickness (figure 5.8). ParticulateFilter template is used in the definition of the filter geometry and thermal properties only. Soot loading is modelled through a Filtration reference object which is referred inside ParticulateFilter template. Regeneration is modelled through SurfaceReactions reference model. ParticulateFilter template and Filtration and SurfaceReactions reference models have been used together for complete DPF item modeling.

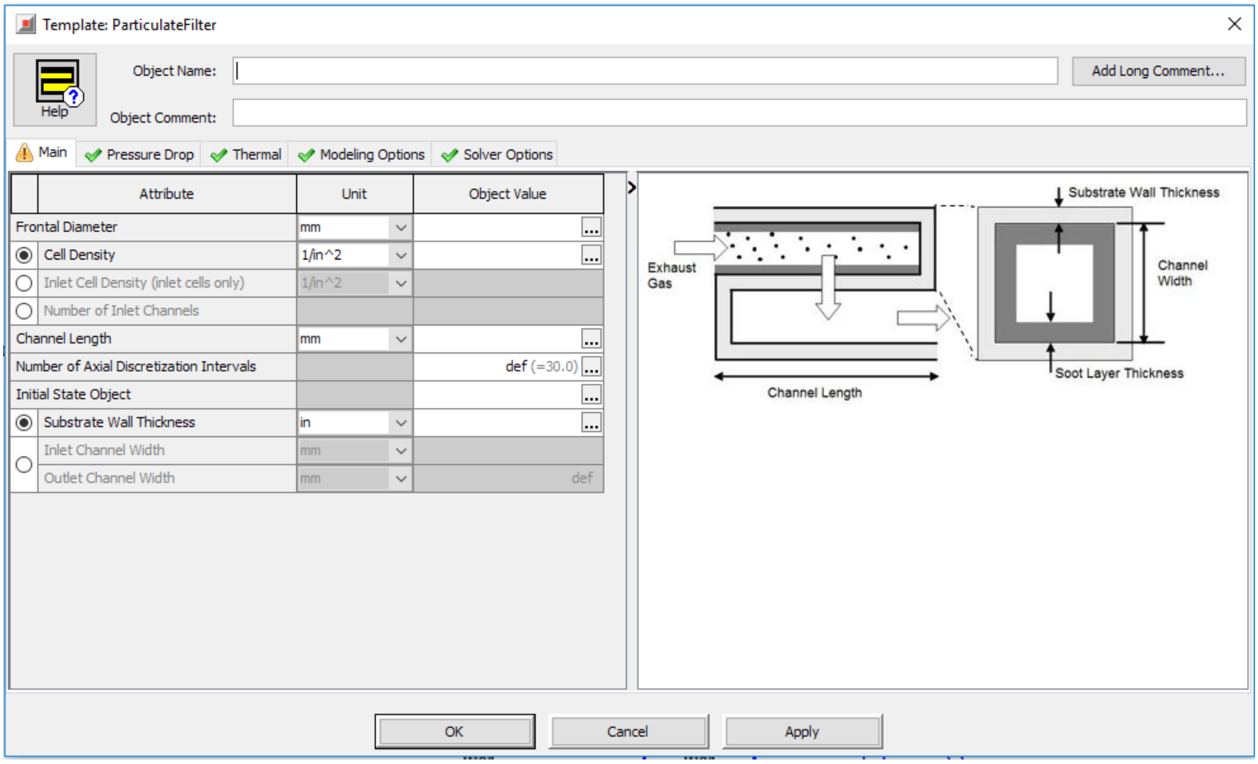

	Attribute	Unit	Object Value
	Frontal Diameter	mm	
●	Cell Density	1/in^2	
○	Inlet Cell Density (inlet cells only)	1/in^2	
○	Number of Inlet Channels		
	Channel Length	mm	
	Number of Axial Discretization Intervals		def (=30.0)
	Initial State Object		
●	Substrate Wall Thickness	in	
○	Inlet Channel Width	mm	
	Outlet Channel Width	mm	def

Figure 5.8. ParticulateFilter template: required geometrical inputs.

Orifice connections simulate the flow resistance. Pressure losses are due to friction in channels and to the flow resistance in the pores. Zero thermal losses are assumed for the inlet and outlet pipes.

Only a single flow constitutes the model input, the changes in composition have been defined according to the data registered by the mass flow controllers. Pressure for the inlet flow has been set to atmospheric value and temperature equal to the inner reactor temperature, according to the profile already presented in figure 5.2.

An important requirement for the model has been its flexibility since multiple experimental data have needed to be handled. The model is able to read its input data from an excel sheet which can be dynamically modified through data overwriting, thus avoiding the data storage inside the model itself. The dynamical rewriting of the inputs is also convenient for the possibility of processing experimental raw data in a suitable form and for selecting the intervals that need to be considered during kinetic parameters optimization.

A major simplification has been used in the model formulation: temperature change due to the exothermic reactions has been modelled but not taken into account for kinetic parameter estimation. However, this assumption is strongly limiting the model effectiveness. Heat transfer between gas and substrate is modelled in the ParticulateFilter template with the definition of the filter walls material properties from a standard GT-SUITE material library. Adiabatic conditions are assumed for the reactor.

Filter regeneration is modelled through the SurfaceReaction reference model for substrate wall and soot cake layer. The implemented kinetic model description can be found in the previous chapter on soot oxidation.

For heterogeneous reactions, solid phase contains the sites for the reaction. Soot is considered both as a reactant and as an active site, fixed site density of 100 mol/m^3 has been assumed.

5.3.1 Work Overview

5.3.1.1 Pressure Drop Model

In total, two filter models have been created, being representative of the cordierite and silicon carbide substrates. The filter geometrical and physical parameters for the uncoated and coated silicon carbide are identical, provided a change in monolith side dimension due to increased thickness inside walls when ceria is present.

Each model has initially been built tuning the physical parameters for the clean filter: permeability, pore diameter, filter porosity, contraction and expansion coefficients and Forchheimer constant. Experiments no.20 and 21 have been used for parameters calibration for the cordierite and SiC filters, respectively.

Permeability parameter establishes a linear relationship in between pressure drop and flow rate at low flow rates. Additional quadratic behaviour is considered with expansion/contraction pressure drop coefficients and Forchheimer constant. Pressure drop tests were performed at both high and ambient temperature with different inlet flows. The ambient temperature pressure drop trend against volume flow is shown for both filters in the specific experiments considered in figure 5.9.

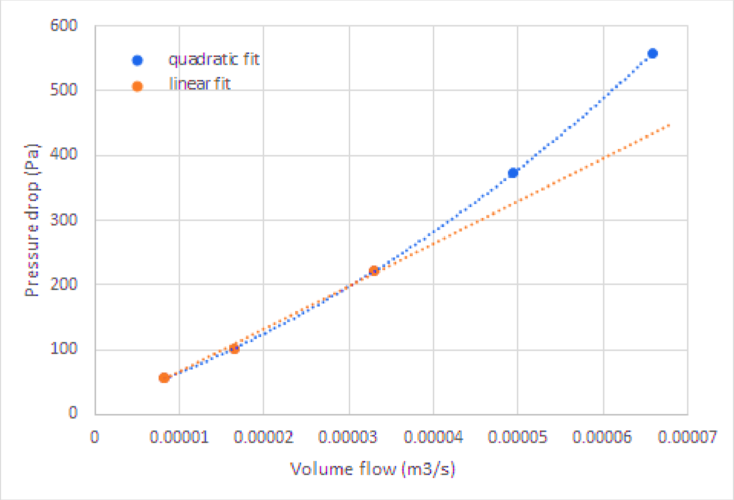

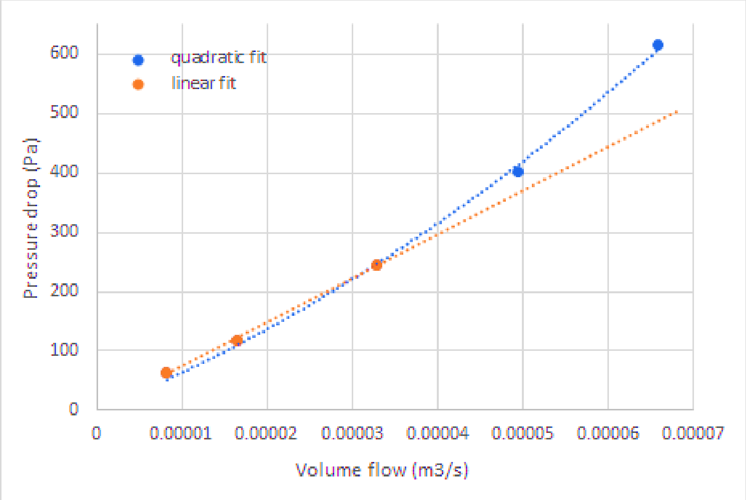

Figure 5.9. Clean filter pressure drop steady-state values against inlet flow for cordierite (top) and SiC (bottom) filters: linear and quadratic data fit for different volume flows.

It has been verified with manual tuning of the parameters that the effect of the expansion/contraction coefficients over pressure drop quadratic behaviour is minimal, instead Forchheimer constant is a strongly affecting parameter.

Calibration of the previously listed model parameters has been therefore carried out. The selected time span for the experiment considered ambient temperature and complete soot oxidation conditions, that are referred to as clean-filter conditions. Software-aided optimization has been performed and the obtained values are presented in table 5.4.

Table 5.4. Optimized parameters for clean cordierite and SiC filters.

	Cordierite	**SiC**
Porosity	0.577	0.499
Pore diameter (mm)	27.1	17.4
Permeability (mm)	$8.55 \cdot 10^{-8}$	$5.39 \cdot 10^{-8}$
Forchheimer const (1/m)	$2.47 \cdot 10^{10}$	$6.8 \cdot 10^{10}$
Expansion/contraction coefficient	1.3	0.64

The results are in agreement with literature proposed ranges and they have proven to be meaningful also against validation. The plots 5.10 and 5.11 capture the relevant time span for clean-filter conditions displaying calibration and validation cases.

Since no experimental data were available for comparison in the soot loading procedure, soot packing density, soot porosity, soot permeability and percolation constant were set to the default values proposed by GT-SUITE.

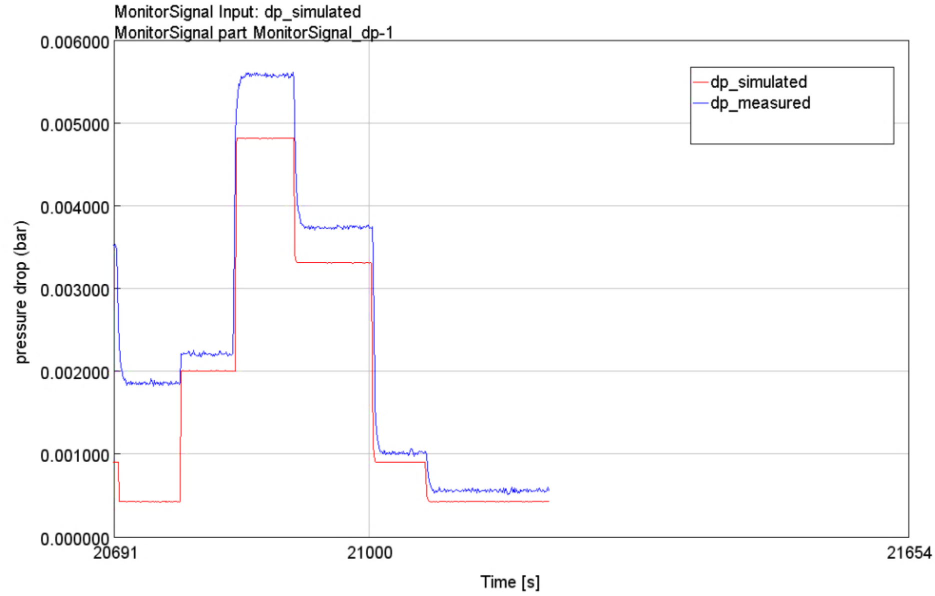

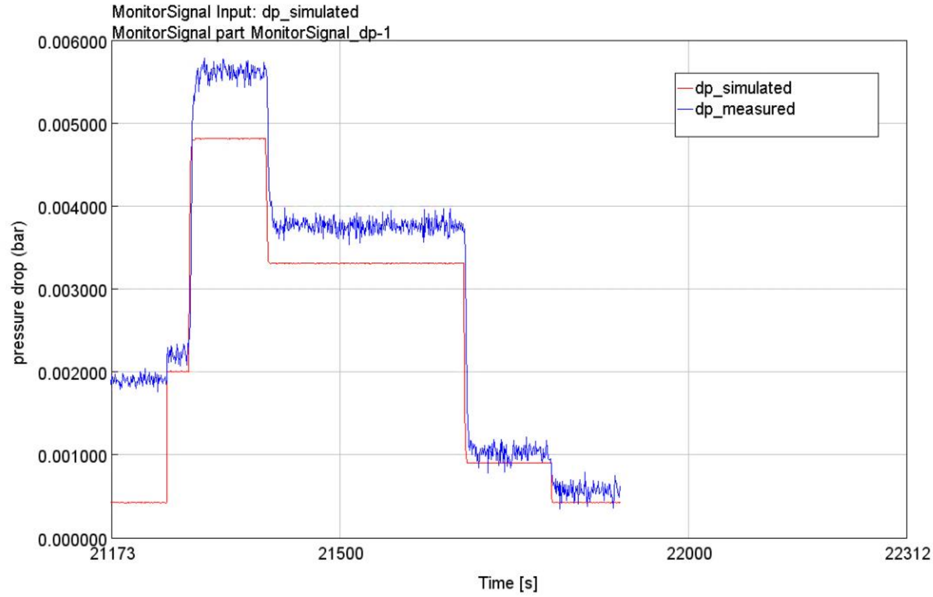

Figure 5.10. Clean filter pressure drop prediction for cordierite model: top, experiment no.20; bottom, experiment no.25.

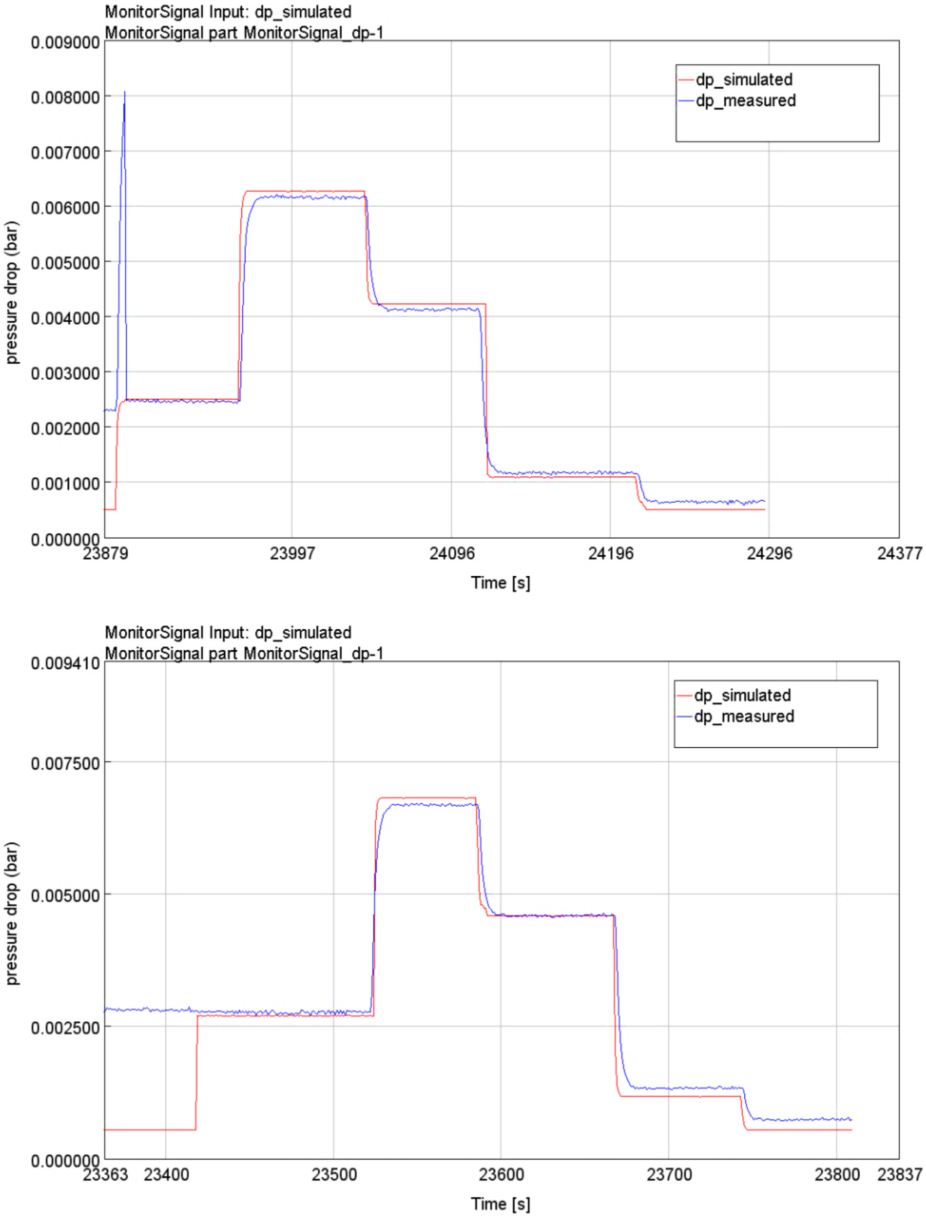

Figure 5.11. Clean filter pressure drop prediction for SiC model: top, experiment no.21 (uncoated); bottom, experiment no.22 (coated).

5.3.1.2 Kinetic Model

Once established the reaction mechanism and the kinetic model, which is schematically represented in figure 5.12, kinetic parameter estimation has been carried out.

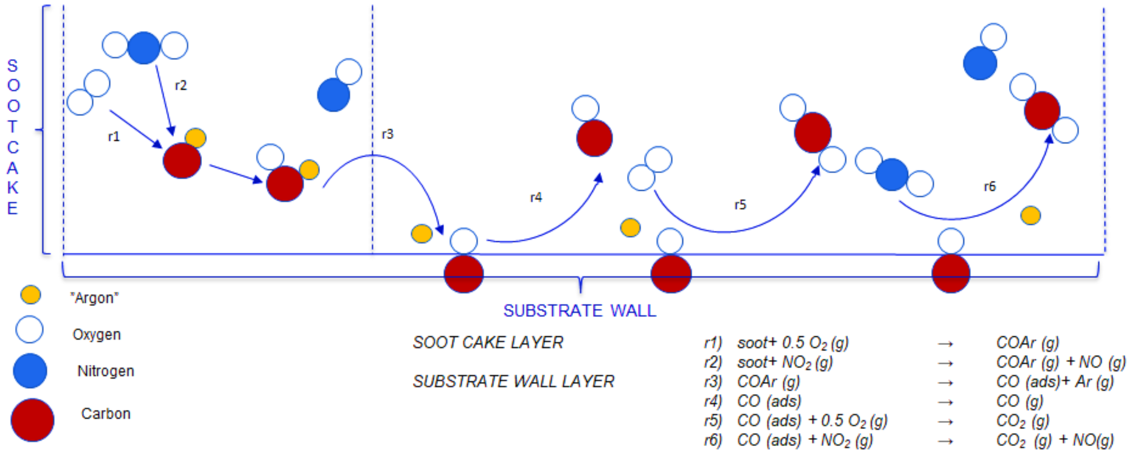

Figure 5.12. Schematic representation of the implemented reaction mechanism.

The recommended procedure suggests calibration of kinetic parameters for NO_2 oxidation first and then for O_2 reaction. However, the simultaneous occurring of both reactions has been considered while estimating parameters in the present work due to the peculiar experimental conditions applied. A suggestion for further work would be the development of the kinetic model selecting the intervals were NO_2 only is fed and calibrating parameters for the low-temperature reaction according to NO emissions. It is important to underline that this procedure can be applied when a good kinetic model is already established and kinetic parameters have already been estimated, or at least their correct range.

Since no previous work was carried out on the given data, trial-and-error procedure has been applied for parameter estimation while the whole reaction set was implemented. Also, a deep speculation has been required before elaborating an efficient reaction and kinetic scheme.

Values for activation energies in the oxidation reactions have been taken from literature in the first instance, proving good applicability to the case. Pre-exponential factors have been subsequently optimized over a large range. Optimization process has been then carried out for activation energies, with a narrow optimization range for the parameters. Activation energy values search is performed in a restricted range due to the parameter physical meaning, instead pre-exponential factors can combine many physical parameters, from this the arisen search complexity. Then, a third optimization over a restricted interval for pre-exponential factors with the optimized values for activation energy has been performed. Optimization variables and sensitivity plots are collected in Appendix A, while simulation results are discussed in the next section.

The model has been extended to the entire duration of the experiment no.12, as a first verification step. Then, since one of the objectives for the work was to establish a flexible kinetic model for the entire set of experiments, validation has been subsequently carried out using different inputs. Experiment no.14, 21, 26 and 11 inlet conditions have been used. All simulation results are presented in the next section. In table 5.5, the steps through which the project was developed are resumed for clarification.

Table 5.5. Schematic workplan.

Model Calibration	Model Verification	Model Validation
Filter #12 (8000-19500 s)	Filter #12 (19500-37500 s)	Filters #14, #21, #26, #11

6. Results

6.1 Mini-DPF Model

Kinetic parameters values obtained after optimization with the previously discussed procedure are listed in table 6.1.

Table 6.1. Optimized Arrhenius parameters for the implemented kinetic model.

i	$\boldsymbol{A_i}$ **(10^{Ai})**	**Ea_i**
1	$1.46 \cdot 10^9$	149.9
2	$1.71 \cdot 10^5$	68.5
3	$5.25 \cdot 10^9$	-
4	$3.82 \cdot 10^7$	99.1
5	$5.61 \cdot 10^8$	61.8
6	$5.57 \cdot 10^5$	11.6

The implementation of the surface kinetic mechanism needs a check of its performances, which cannot be achieved simply looking at the emissions plots. Total soot conversion into the gaseous species $COAr_{0.5}$ is demanded. Then, total adsorption via CO_{ads} species must occur, with ideally no $COAr_{0.5}$ escaping in the outlet flow.

Monitoring the composition of the outlet flow, it is seen that no $COAr_{0.5}$ species is present.

Surface species coverage θ_{CO} is plotted against time in figure 6.1.

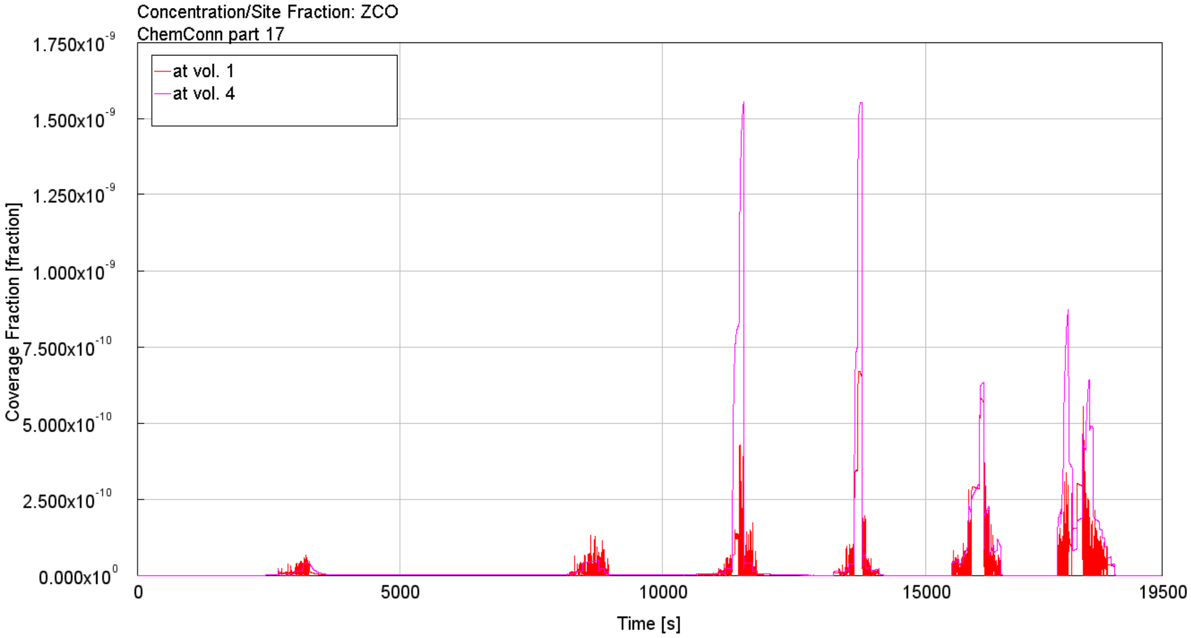

Figure 6.1. Surface species coverage θ_{CO} plot, filter #12.

The plot shows a trend following the inlet oxidant feeds. The coverage values are also low enough, around 10^6 times lower than the emission levels, ensuring that the imposed kinetics for the adsorption is effective for the prediction. Coverage is plotted in the first and last reactor volumes, a different trend is observed, with higher values for the latter. This can be linked to different reactivity for reactor volumes, since looking at reaction rates plots it can be seen that conversion is generally higher in the first volume and then progressively decreasing. However, the difference remains small. Also, the oscillating trend points out that in the first volume numerical instability is verified: this can be due either to a numerical effect such as simulation time step and reactor discretization length, or to reactions happening simultaneously. It can be concluded anyhow that, with the optimized values for the kinetic parameters, the desired reaction path is met, with no accumulation of the surface species. There is always space for the gaseous compound to adsorb over soot active sites.

NO, CO_2 and CO emissions plots, together with error evaluations, are presented below.

Only the first 19500 s are presented in the plots in order to have a better visualization of the results. Applying the kinetic parameters to the instants following the first 19500 s can be considered already as a first form of verification, since, as previously reported, during the model elaboration this time interval has been neglected. Inlet conditions for temperature and oxidants concentration are plotted together in figure 6.2.

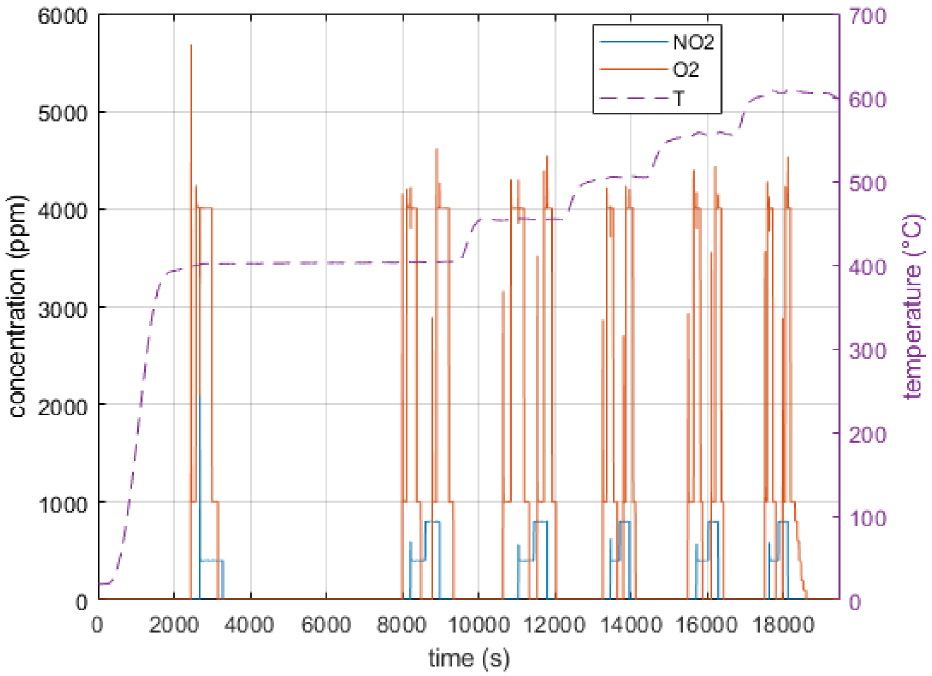

Figure 6.2. Temperature profile and pulses injection sequence for filter #12 between 0-19500 s.

6.1.1 Emissions

6.1.1.1 NO_x

The developed kinetic model only considers NO emissions in between the possible nitrogen/oxygen compounds. However, during the experiments, the sensor detected both NO_x and NO emissions, from which NO_2 amount was derived. Therefore, a minor amount of NO_2 is also present, possibly deriving from NO_2/NO decomposition equilibrium in the presence of oxygen. The emissions resulting from the simulation are compared for both NO only (figure 6.3, scatter plot figure 6.4) and NO_x (figure 6.5) measured data.

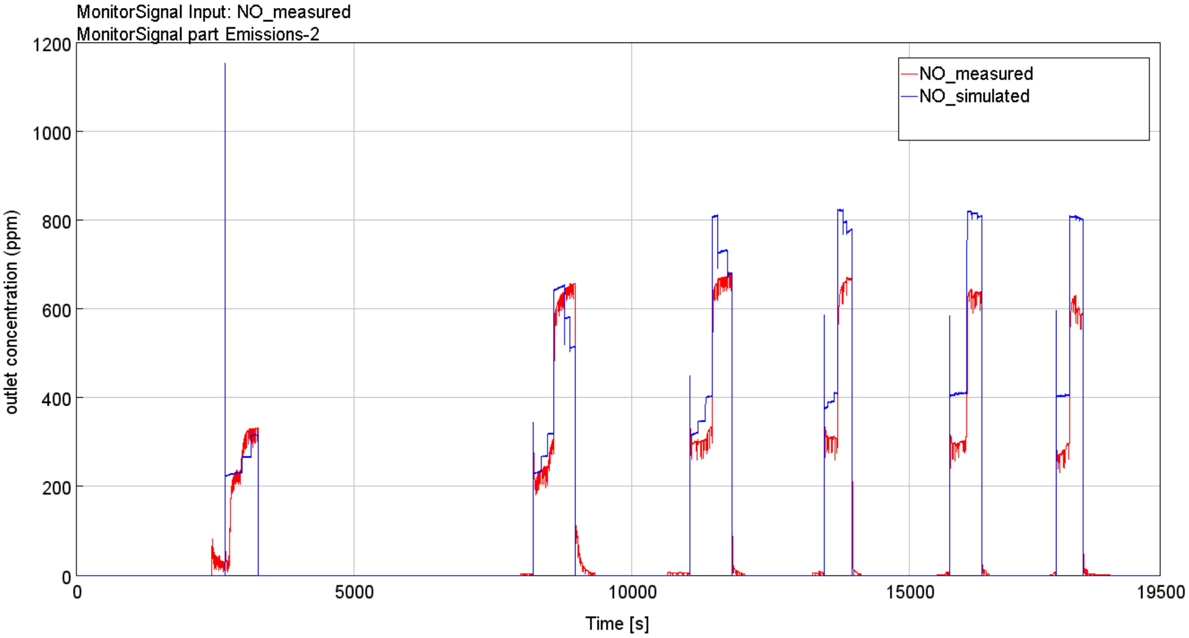

Figure 6.3. NO emissions: comparison in between measured and simulated data, filter #12.

The plot in figure 6.3 shows that two levels for NO emissions are present, corresponding to 400 and 800 ppm for NO_2 injections. NO_2 to NO conversion is not total, instead, for experimental data. Looking at simulated data, for the lower temperature values, some sub-levels appear with progressive increase at low level (400 ppm) and decrease at high level (800 ppm). These steps point out a different mechanism in NO production depending whether nitrogen dioxide is fed alone or oxygen is also present. The overall trend for NO emissions is inversely proportional to O_2 injection levels. For the measured data set, the difference in between combined oxidants and NO_2 action only is less evident. Also, at high temperatures this behaviour fades. A plausible explanation can be driven considering the effect of reaction 2.26 where NO is produced involving indirectly O_2 in the reaction path. Further exam of the kinetic parameters for this reaction can be therefore carried out based on these considerations. Activation energy seems to be the most affecting parameter due to the different effect with temperature.

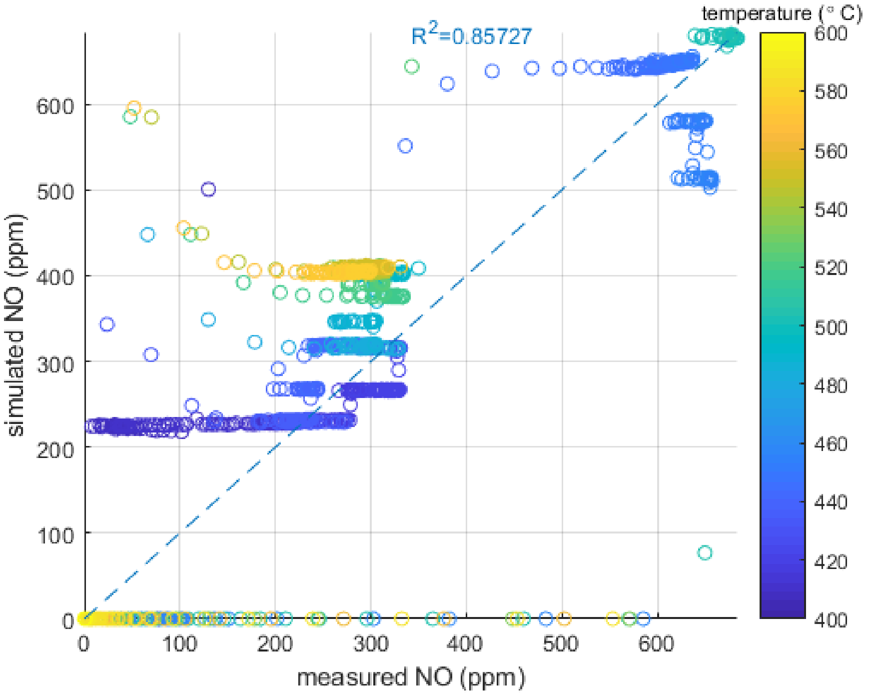

Figure 6.4. NO emissions scatter plot and determination coefficient, filter #12.

As a whole, NO emissions are overestimated with increased effect at higher temperatures. The model also makes sharp predictions along the subsequent steady states, without considering angles gradual variations, possibly due to the "sticking" trait of NO_2 molecule in the experimental apparatus. For taking this into account, properly designed effects could be added to the basic kinetic model. The measured data does not seem to be affected by the sudden opening of the mass flow controllers creating spikes, contrarily to what happens for the simulated data. The relative error meaninglessly increases in these time instants.

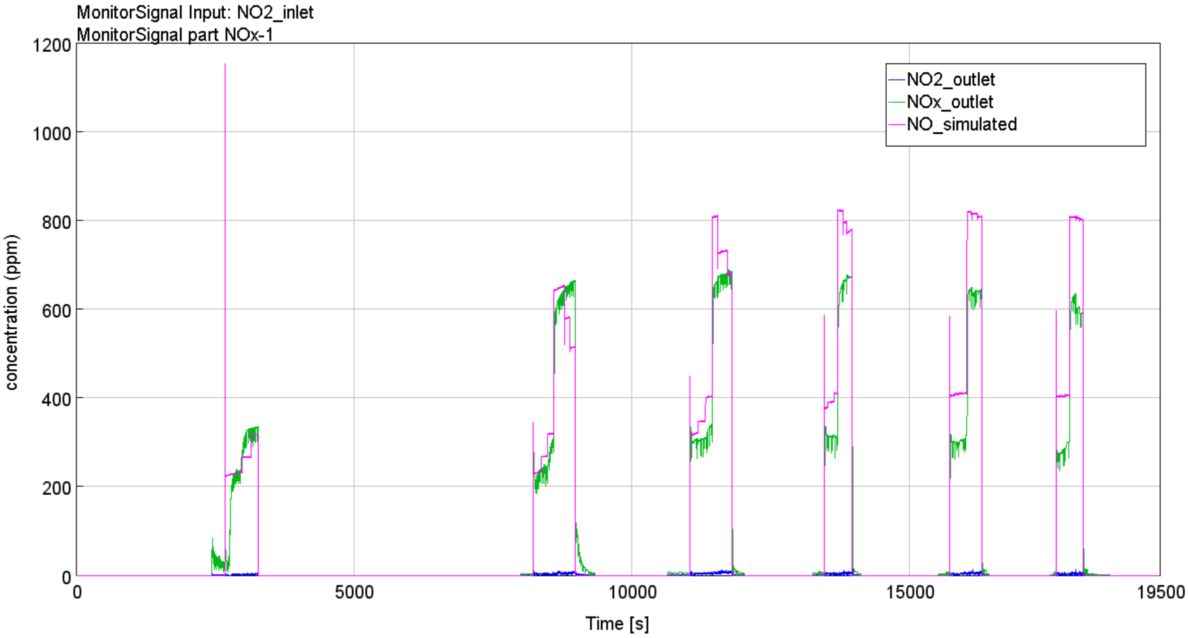

Figure 6.5. Comparison in between measured NOx and NO2 with simulated NO emissions, filter #12.

NO_x plot in figure 6.5 shows that the NO_2 emitted amount is minimum compared to NO for all temperature levels.

6.1.1.2 CO_2

CO_2 emissions trend is plotted in figure 6.6, with related scatter plot in figure 6.7.

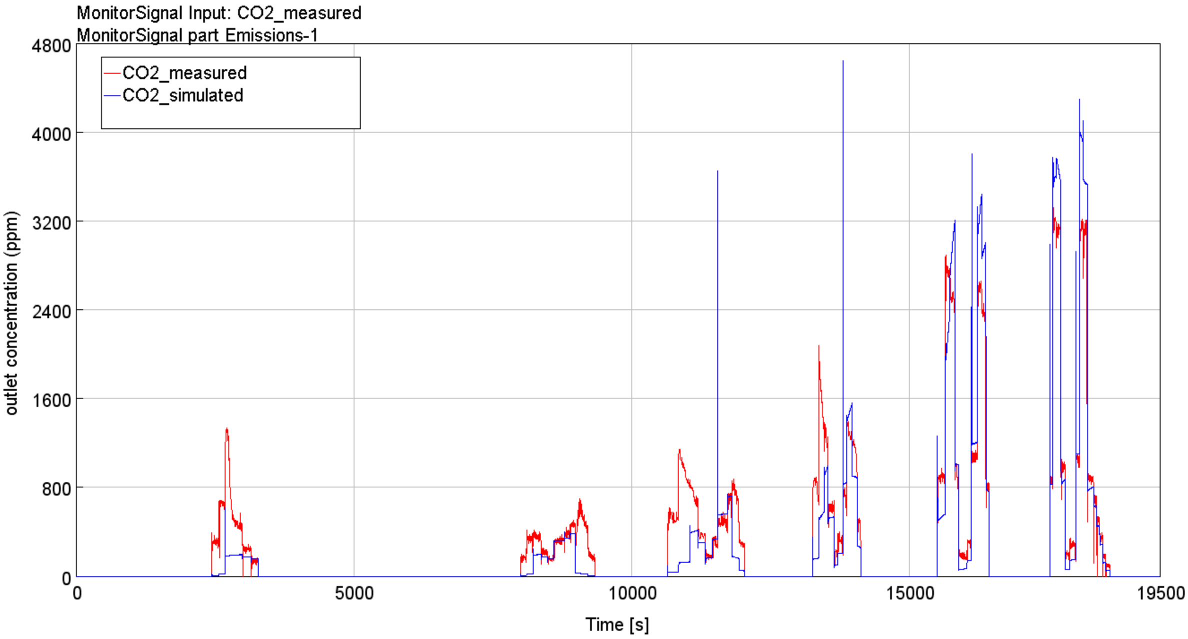

Figure 6.6. CO_2 emissions: comparison in between measured and simulated data, filter #12.

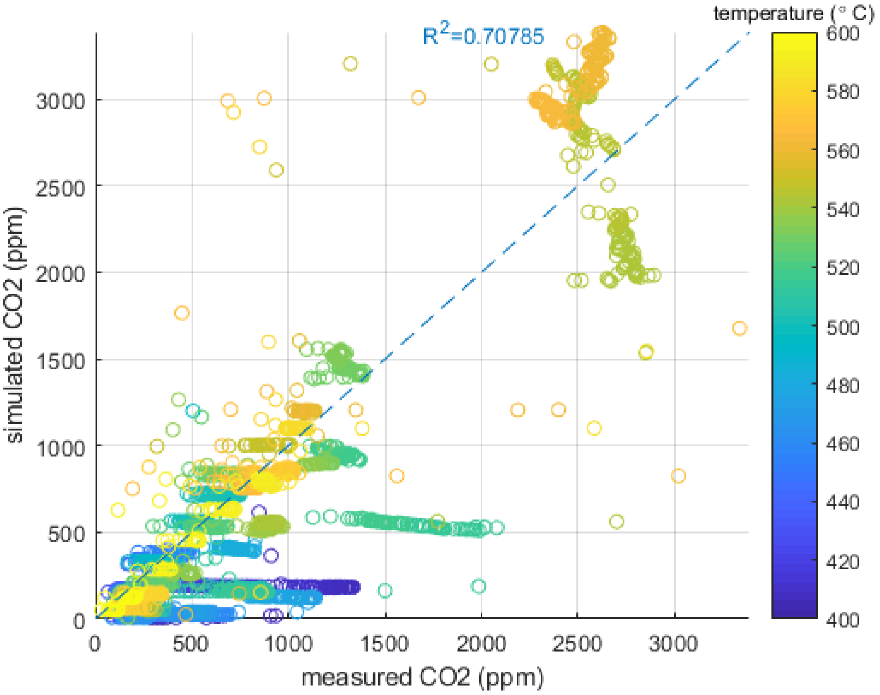

Figure 6.7. CO_2 emissions scatter plot and determination coefficient, filter #12.

CO_2 prediction is overall good, in particular with combined O_2 /NO_2 when the latter is at high level. Again, this can be due to the effect of the reaction 2.26.

The measured data seem to have blurred borders which are not corresponding to the sharp changes for different oxidant levels obtained from the simulation. The different behaviour is less evident at high temperatures. This may suggest that the implemented kinetic parameters for the different reactions are too dissimilar. Very good trend is observed when oxygen alone is injected at high temperatures, since the pulse sequence for the last step is slightly different. However, oxygen effect at low temperatures is underestimated.

6.1.1.3 CO

Figure 6.8 and 6.9 show CO emissions trend.

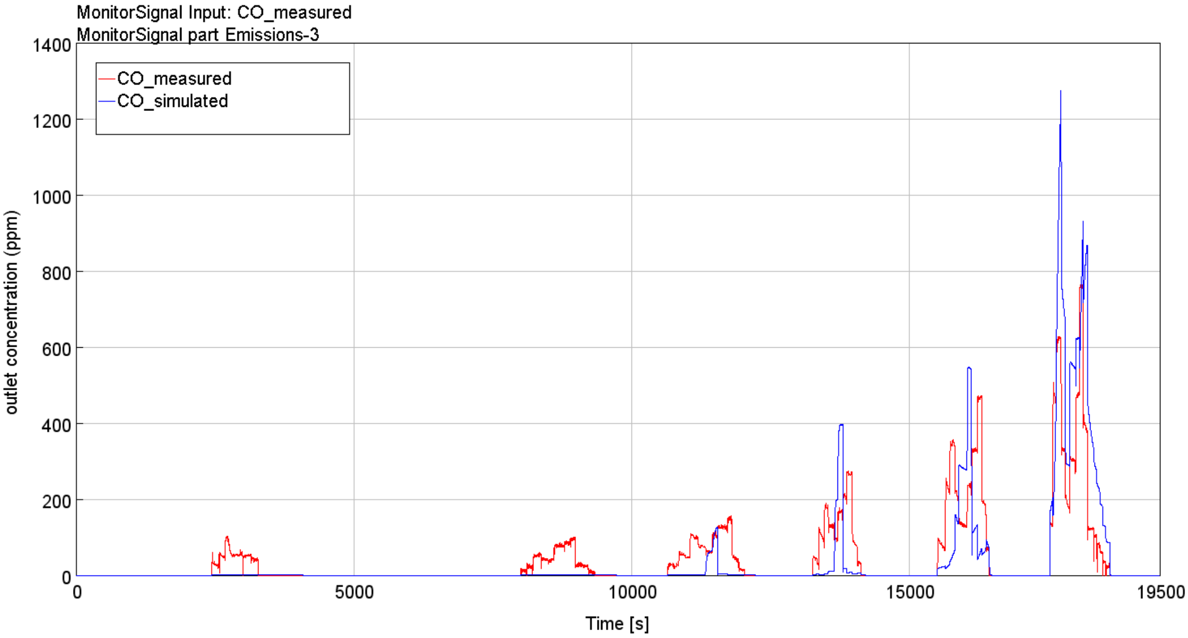

Figure 6.8. CO emissions: comparison in between measured and simulated data, filter #12.

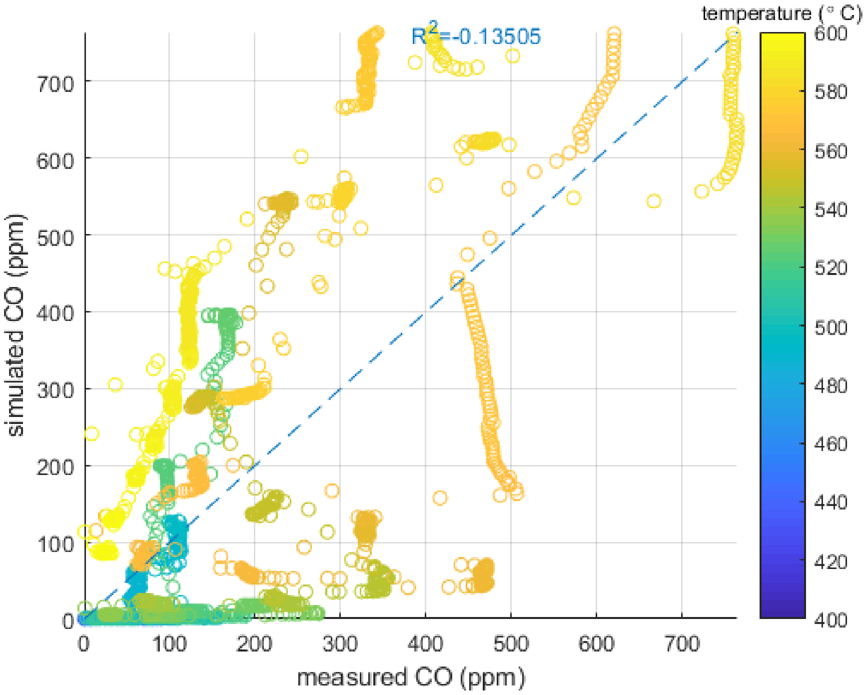

Figure 6.9. CO emissions scatter plot and determination coefficient, filter #12.

CO is highly underestimated at low temperatures and overestimated at high temperatures, suggesting activation energy value for CO reaction needs to be decreased. However, when tuning reaction parameters for the surface reactions scheme implemented, it is fundamental to select which one has the main effect on the model prediction performance. Reactions 2.21, 2.22, 2.23, 2.24 intervene in CO production.

When oxygen only is fed into the system, the emissions prediction looks worse compared to the other cases. The measured data show that borders are sharper compared to CO_2 data, suggesting a more pronounced difference in kinetic parameters for the different reactions in this case. The negative value obtained for determination coefficient R^2 states the poor prediction of the model for this species.

6.1.1.4 Conversion

Soot conversion plot (in figure 6.10 for the entire duration of the experiment) attests that total soot conversion is effectively achieved. Looking at the first half, the model slightly underestimates conversion, possibly due to the poor CO prediction. It is also important to notice that plot has been drawn from half of the filter: soot is converted differently along the entire volume. The filter length has been discretized into 4 intervals, the calculated conversion is higher in the first volume and progressively lower for the subsequent volumes. The simulated results suggest that reactions are developing at the beginning of the reactor itself. The diffusion properties of the oxidants can be determining for this analysis. Decreasing discretization length reduces the difference, though the chosen value has been chosen as a good match in between accuracy of the results and reasonable computational time.

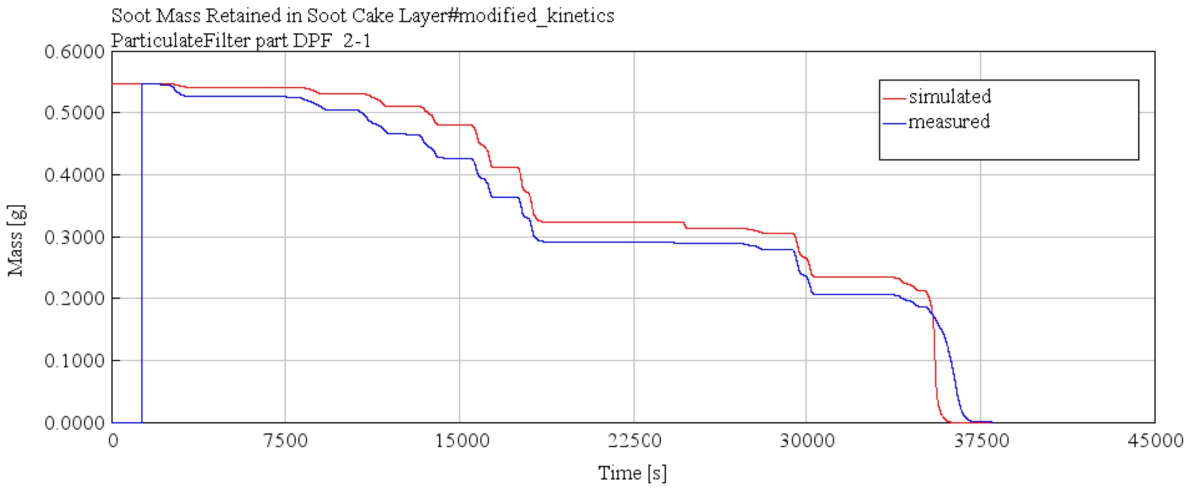

Figure 6.10. Soot conversion in soot cake layer: comparison in between measured and simulated data, filter #12.

Looking at the performances of the model as a whole, it can be noticed that the fit is best achieved for CO_2, while the worst prediction is obtained for CO. Based on the observation of a colleague, it is pointed out that, during parameter optimization, the total error that the software is trying to minimize results mainly affected by the highest levels of the species involved. CO_2 and CO levels are not accidentally the highest and the lowest, respectively, among the emissions considered.

Underprediction with oxygen at low temperatures seems also to be a characteristic for the model, suggesting the need of better tuning for reaction 2.21 parameters.

The model has effectively been built so that the oxidation reactions 2.21, 2.22 determine the mechanism and surface specie adsorption and products desorption 2.24, 2.25, 2.26 are fast enough in order not to have any accumulation in the system, as proven in figure 6.1. It has been verified with manual tuning of the parameters that kinetics for reaction 2.23 has not significant influence on the model performance, as soon as it does not allow CO_{ads} accumulation.

6.2 Verification

A first verification for the model is realized extending the plots for the entire length of the experiment, provided the different temperature profile and oxidant injection sequence represented in figure 6.11.

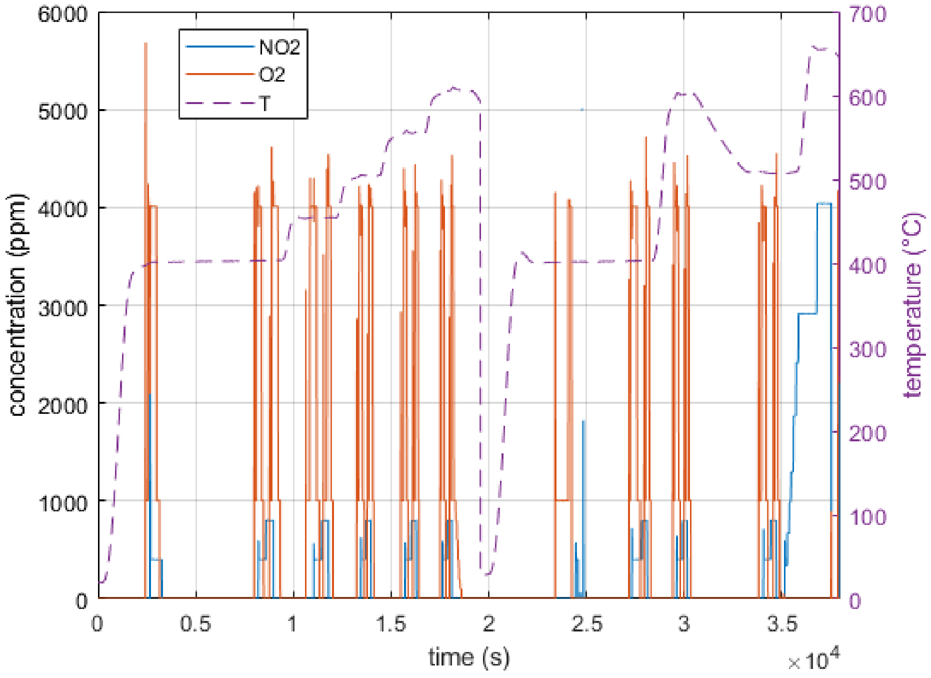

Figure 6.11. Temperature profile and pulses injection sequence for filter #12 between 0-37500 s.

Emission trend for the last part of experiment no.12, once that the kinetic model is applied are represented in figure 6.12, for NO emissions, 6.13, for CO_2 emissions and 6.14, for CO emissions.

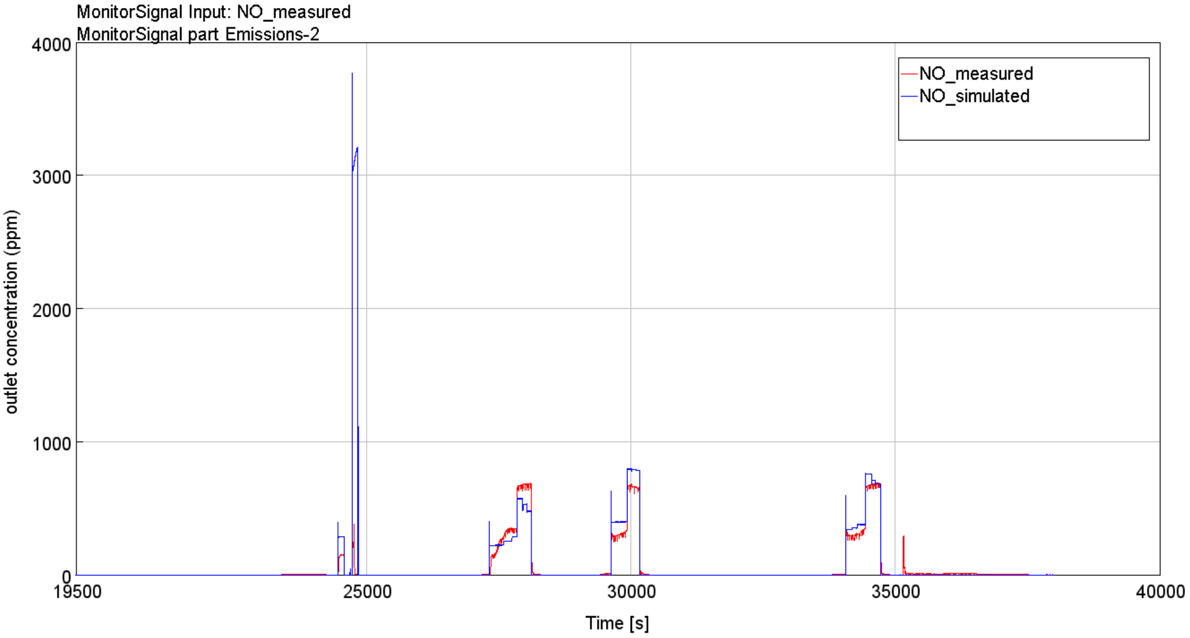

Figure 6.12. NO emissions in between 19500-37500 s instants, filter #12.

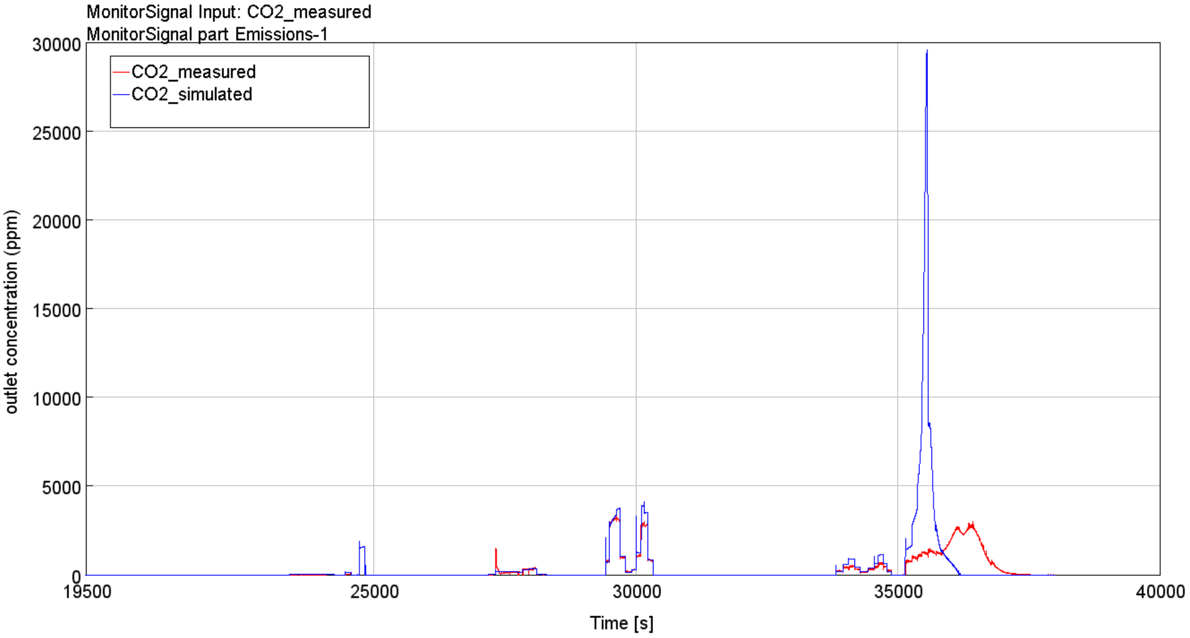

Figure 6.13. CO_2 emissions in between 19500-37500 s instants, filter #12.

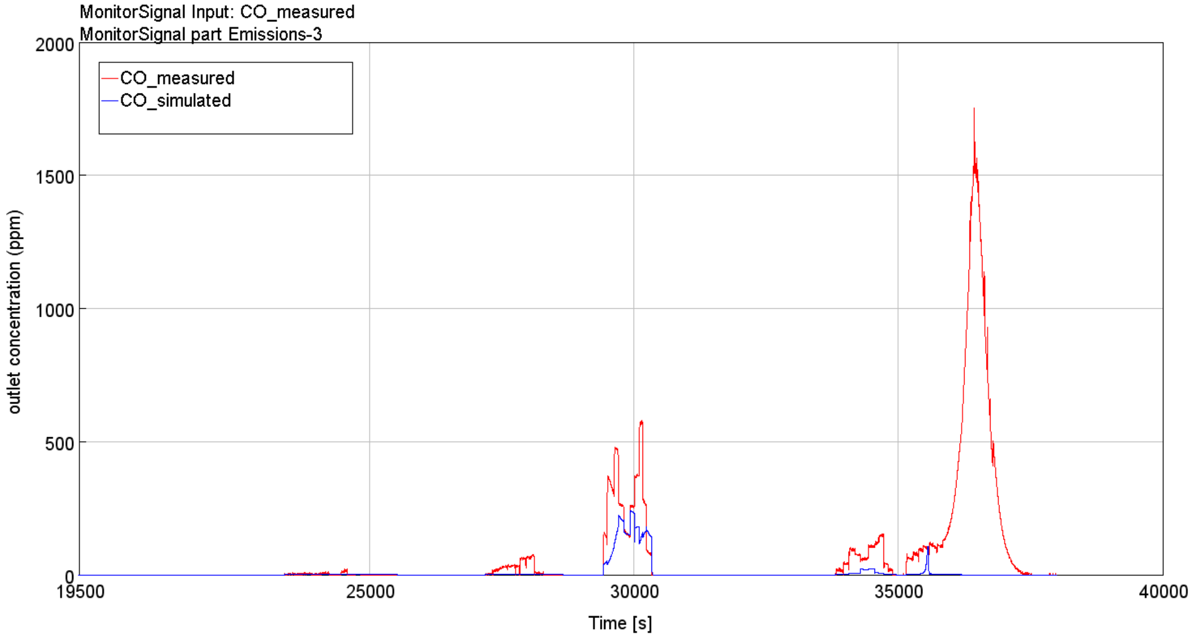

Figure 6.14. CO emissions in between 19500-37500 s instants, filter #12.

The plots are showing a non-dissimilar fit to the one obtained for the original model, since also here temperature is applied through subsequent steps. Once again, the mechanism captures best the behaviour for high temperatures.

The CO/CO_2 prediction in the time interval 35000-37500 s is not significant since the experimental purpose was to obtain complete oxidation of the loaded soot and the oxidant injections were carried out differently from the previously applied protocol (air was fed at different levels in the mass-flow controller instead of NO_2). NO emission at around 25000 s is due to the spike for NO_2 injection that is not captured by the experimental data.

6.3 Validation

6.3.1 Cordierite Filter

Experiment no.14 has been selected for validation of the kinetic model since loading conditions are same of experiment no.12: long loading with upstream DOC. The specific inlet conditions for the experiment are represented in figure 6.15.

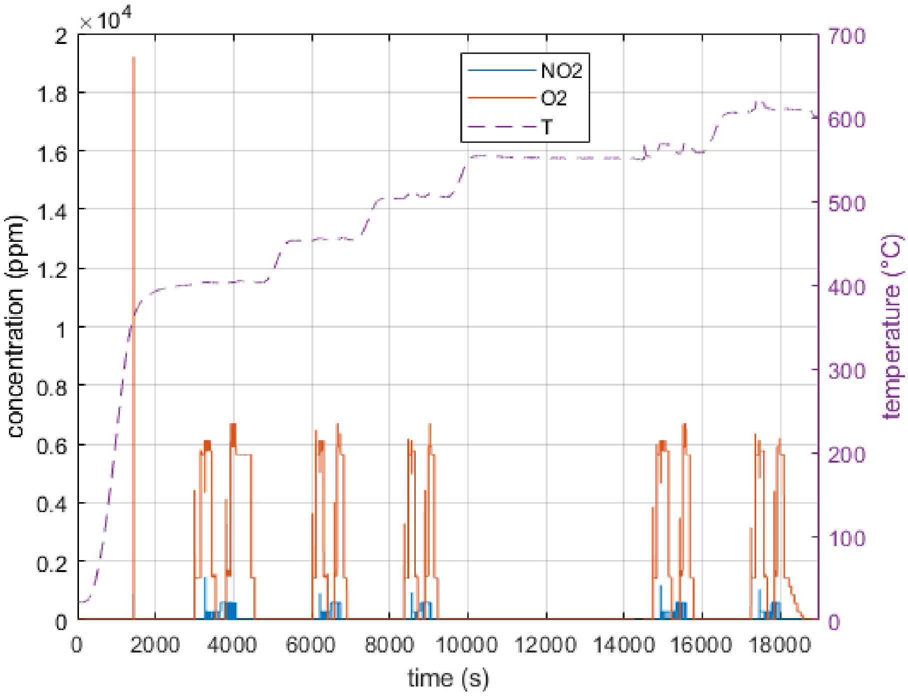

Figure 6.15. Temperature profile and pulses injection sequence for filter #14.

The same observations for filter #12 can be extended to this experiment concerning NO emissions (figure 6.16, scatter plot figure 6.17). However, the vertical bars reflect a different trend for the NO_2 injections, since many smaller steady states were applied instead than single low/high level injections. It is surprising that this behaviour is not captured by the measured data, suggesting that oxidation effect is dragged when NO_2 is not directly present. Also, lower NO_2 levels were applied, around 300 and 600 ppm; total NO_2 conversion is achieved also in this case. O_2 levels are slightly different than in the previous case, being around 1500 and 5500 ppm.

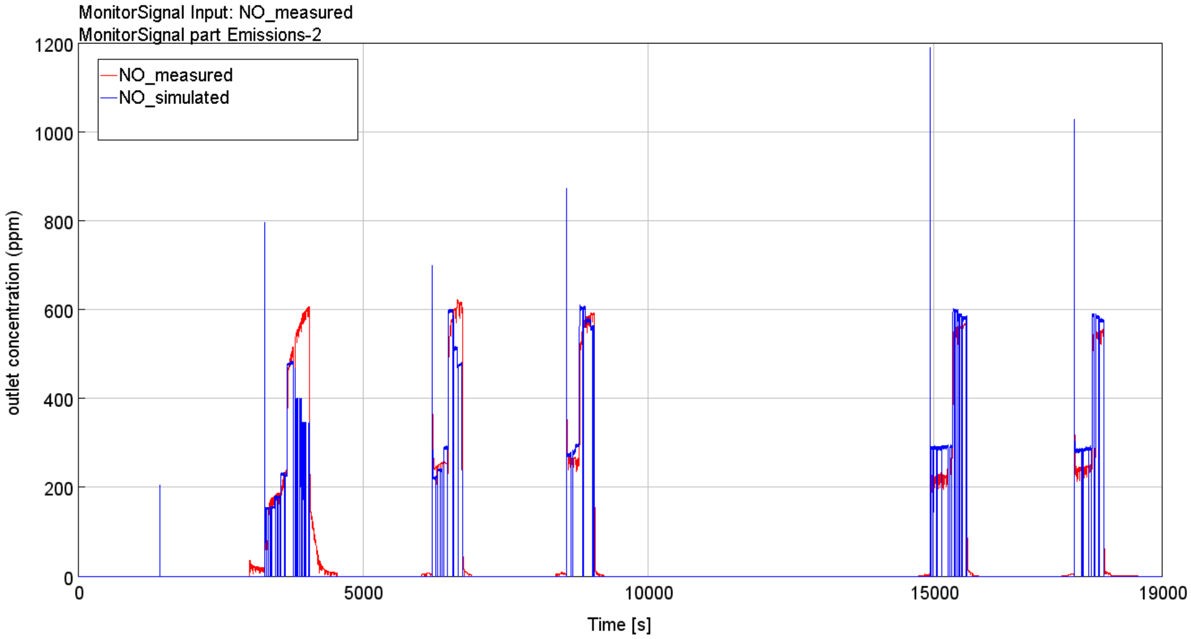

Figure 6.16. NO emissions, cordierite filter: comparison in between measured and simulated data.

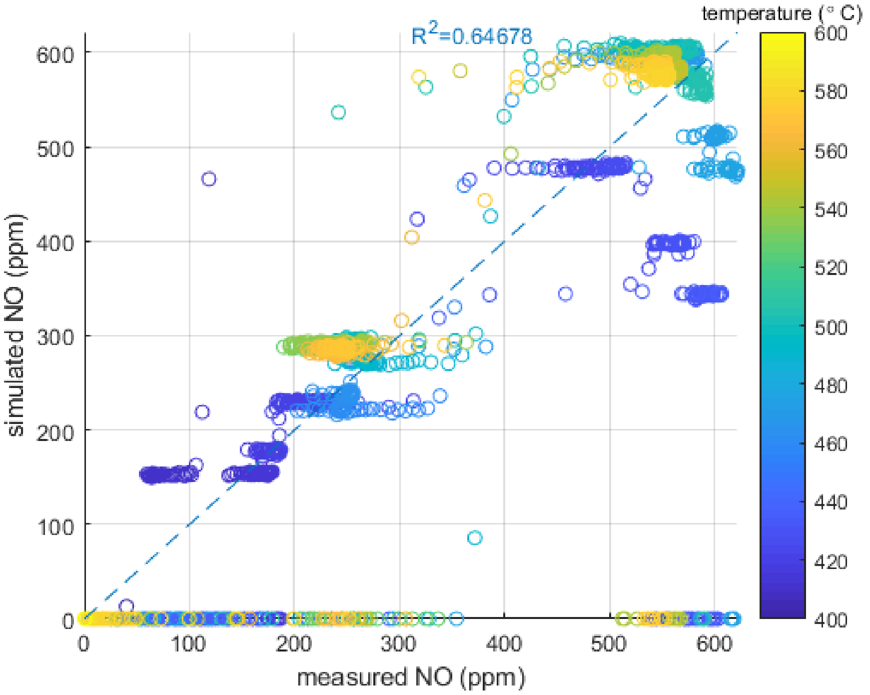

Figure 6.17. NO emissions scatter plot and determination coefficient, cordierite filter.

For CO_2 and CO emissions (figure 6.18 and 6.20, respectively, scatter plots figure 6.21,6.22) the trend developed for the original model is kept. However, the oxygen-driven pattern at high temperature is not as good as in the previous case when considering CO_2 emissions, and surprisingly better for CO. A possible explanation could be the different wall temperature developed as a consequence of the different thermal properties of the involved materials, with consequences on the reactions that originate the two gaseous species.

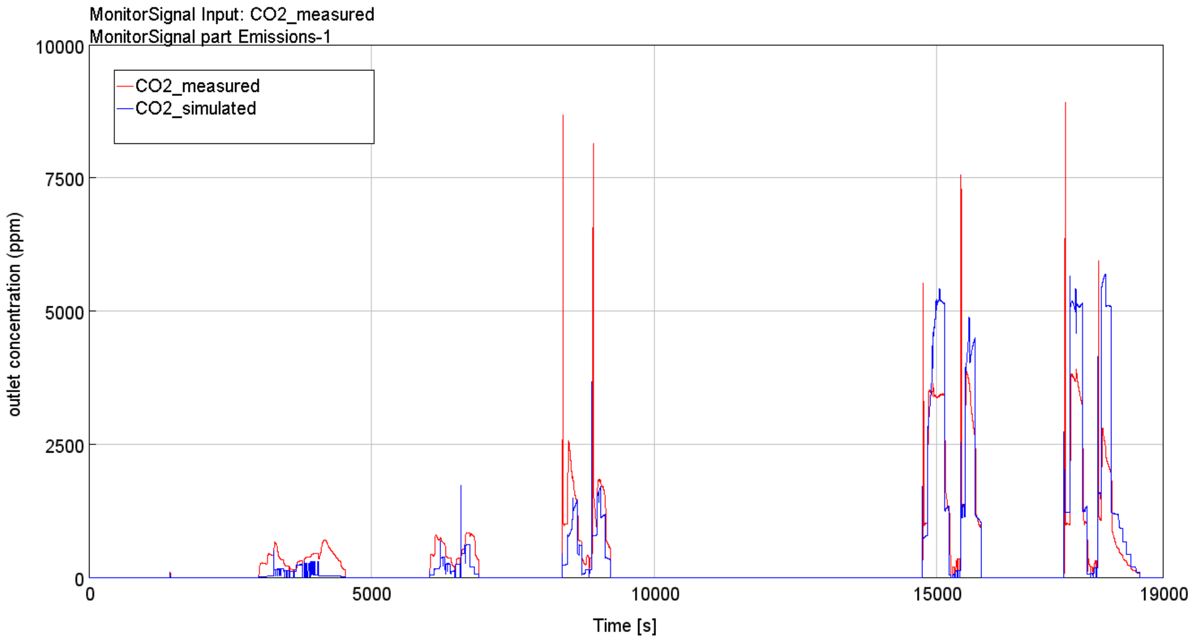

Figure 6.18. CO_2 emissions, cordierite filter: comparison in between measured and simulated data.

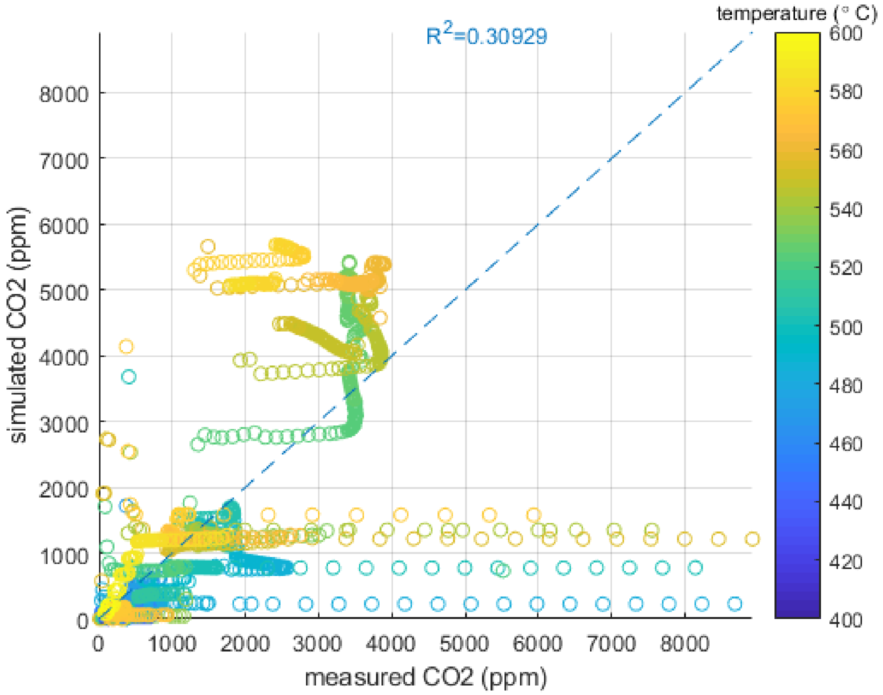

Figure 6.19. CO_2 emissions scatter plot and determination coefficient, cordierite filter.

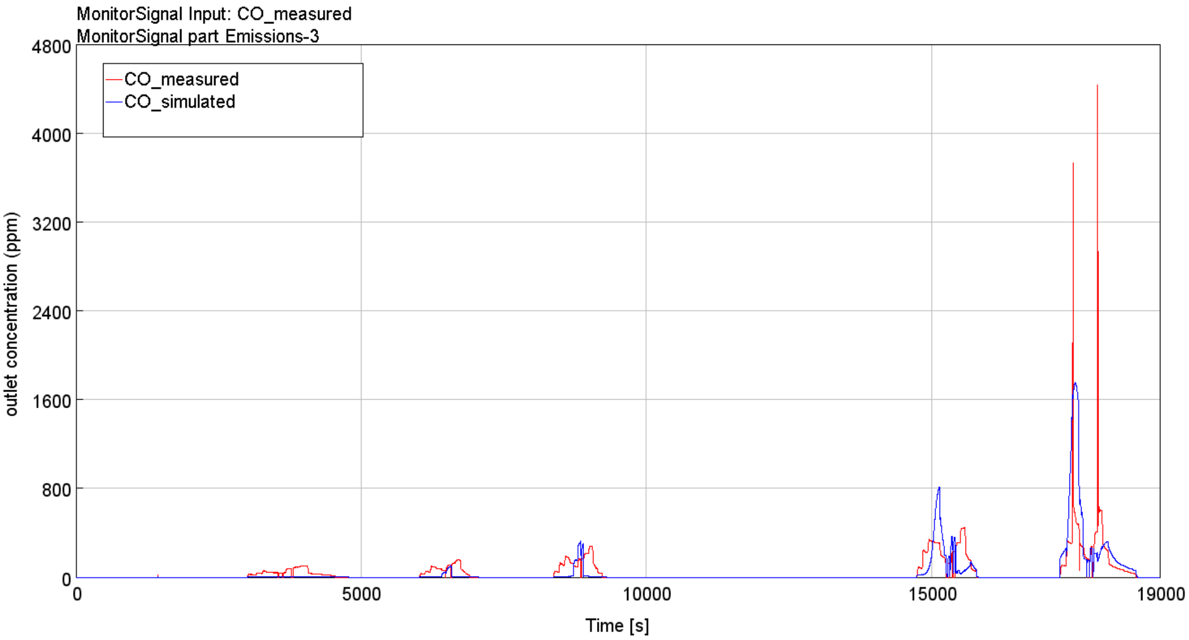

Figure 6.20. CO emissions, cordierite filter: comparison in between measured and simulated data.

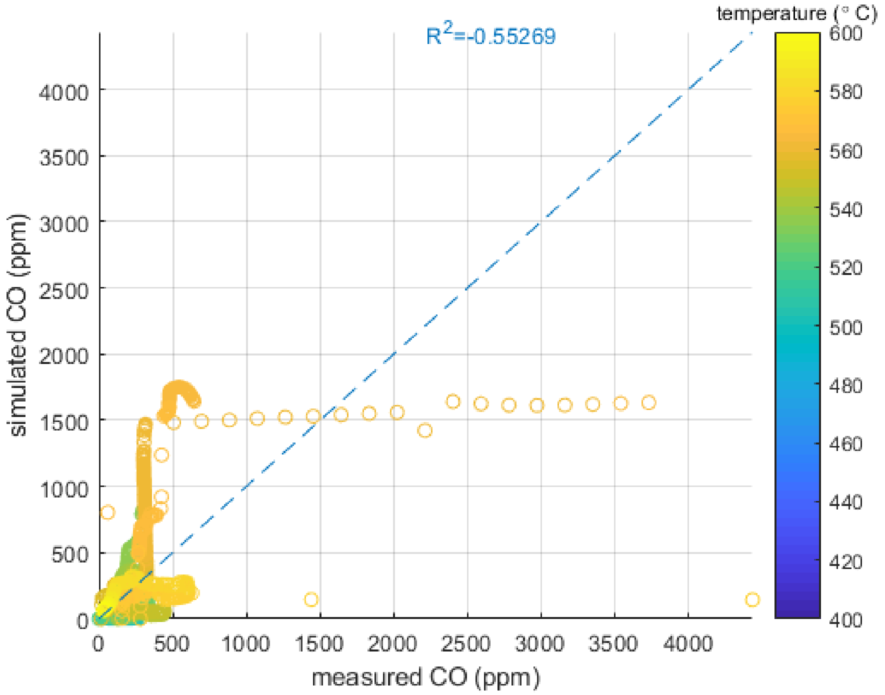

Figure 6.21. CO emissions scatter plot and determination coefficient, cordierite filter.

6.3.2 SiC Filter

Two experiments have been chosen to validate the model created for uncoated and one experiment for ceria-coated SiC filter.

The effect of different loading conditions is examined together with the performances of the model for the uncoated filter. Filter #21 was loaded with upstream DOC under short loading conditions. Filter #26 was loaded without upstream DOC under long loading conditions.

Filter #11 is coated with ceria, loaded with upstream DOC under long loading conditions.

6.3.2.1 Short Loading

The imposed inlet conditions are plotted in figure 6.22. At low temperature, the different shape of the emission is to be ascribed to a different pulse sequence applied.

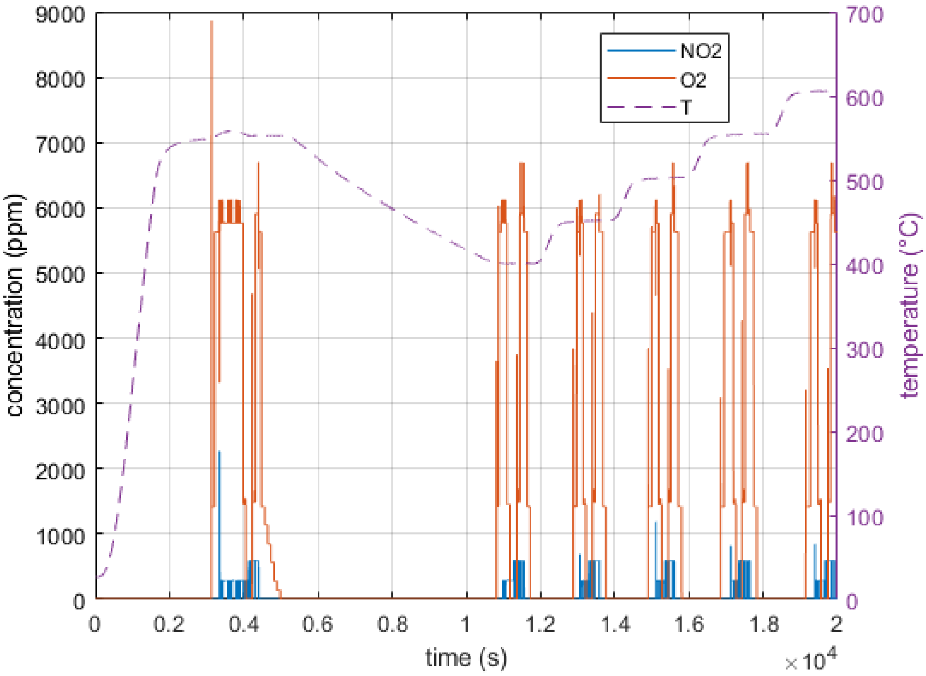

Figure 6.22. Temperature profile and pulses injection sequence for filter #21.

NO prediction (figure 6.23, scatter plot figure 6.24) seems to work in the same similar trend as in the previous cases.

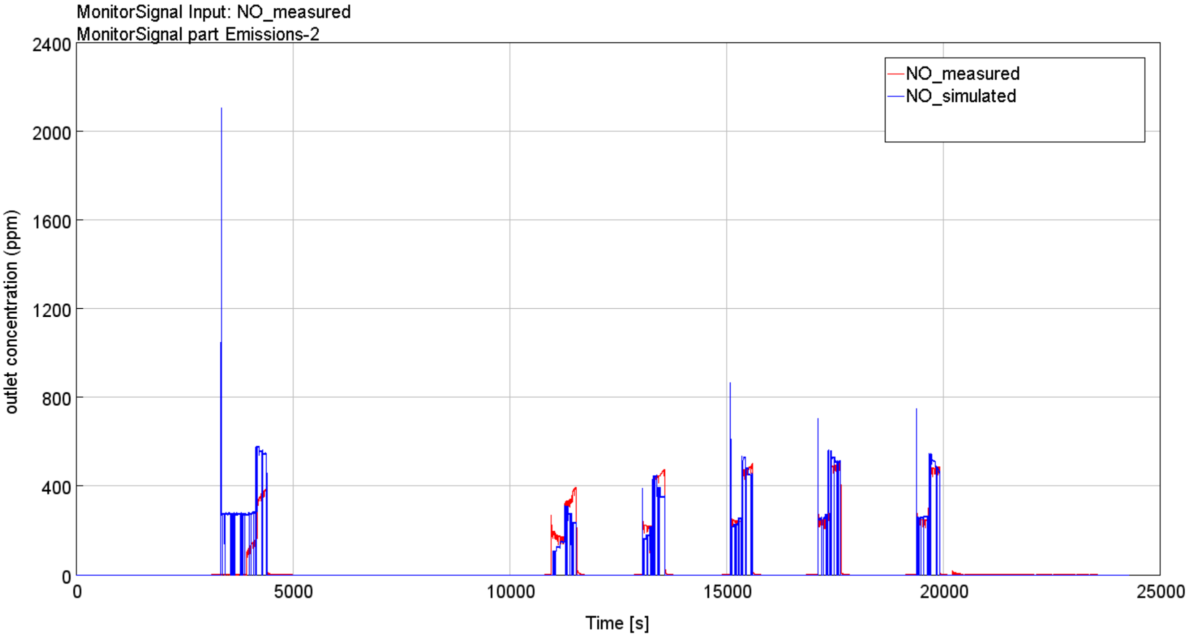

Figure 6.23. NO emissions, silicon carbide filter, short loading conditions: comparison in between measured and simulated data.

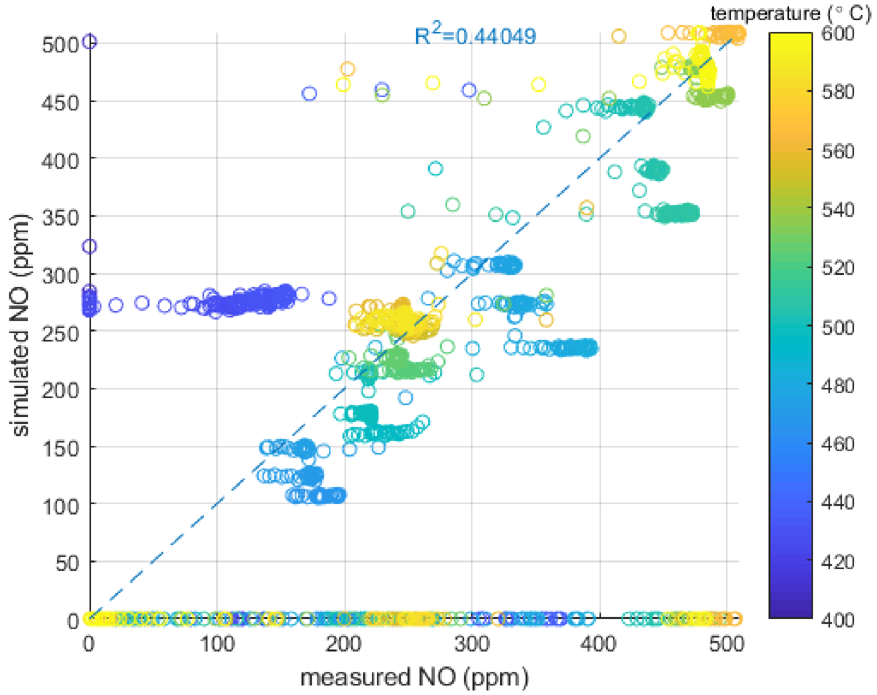

Figure 6.24. NO emissions scatter plot and determination coefficient, silicon carbide filter, short loading conditions.

CO_2 (figure 6.25, scatter plot figure 6.26) shows good performance for low and middle temperature, with good fit when oxygen alone is applied. High overestimation is instead occurring for high temperature, with worse prediction than the ones obtained for the original model.

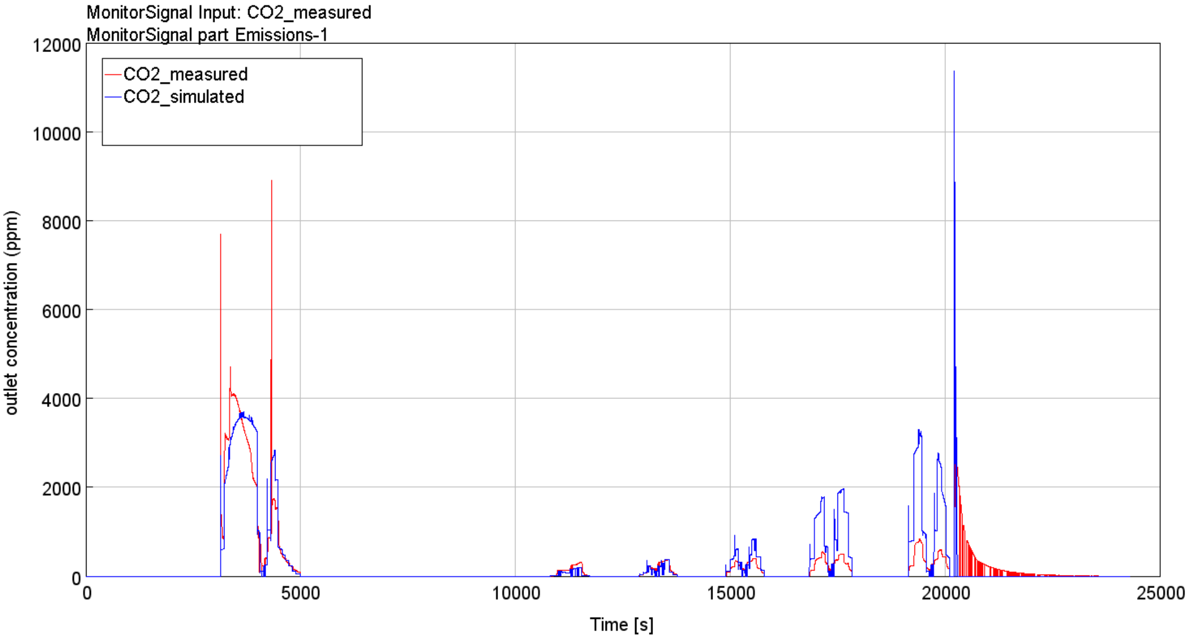

Figure 6.25. CO_2 emissions, silicon carbide filter, short loading conditions: comparison in between measured and simulated data.

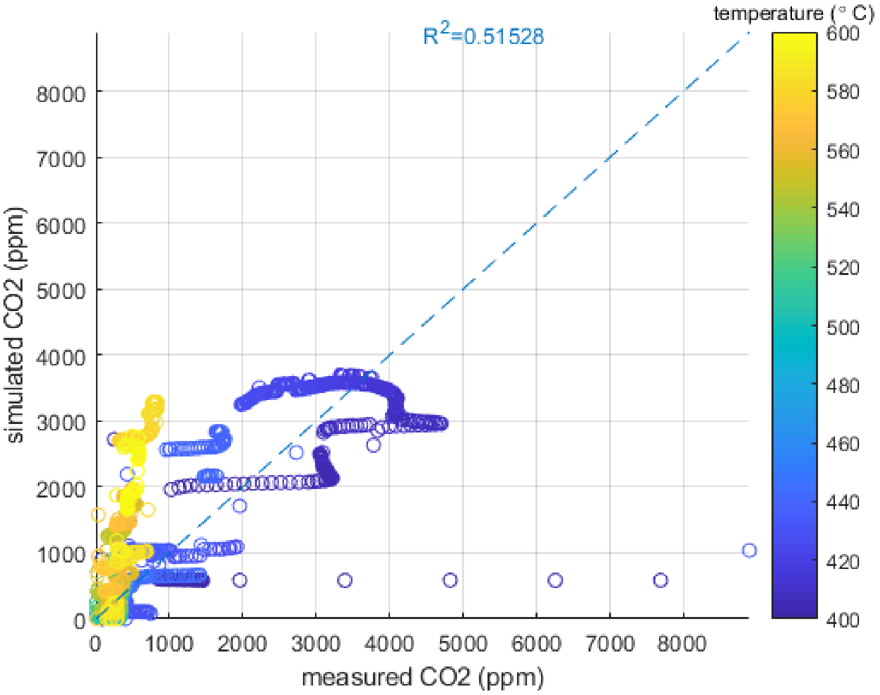

Figure 6.26. CO_2 emissions scatter plot and determination coefficient, silicon carbide filter, short loading conditions.

For CO (figure 6.27, scatter plot figure 6.28), underprediction is verified for every temperature interval and oxygen pattern for CO does not seem to work effectively, since the step trend at low temperatures is not captured properly. A possible explanation is that the implemented mechanism is not well indicating the CO_2/CO selectivity. Once again, the last time intervals are neglected in the analysis due to the different experimental conditions. From the previous study on experimental data, the short loading condition was considered to be responsible for higher reactivity or lower activation energies, due to possible mass-transfer effects. This behaviour finds correspondence in CO_2 emissions prediction, since the implemented mechanism can be considered good enough for discussing about the relevance of the results. Also, the difference arises since soot of different nature is loaded for filter #12, being aged, i.e. pre-oxidized.

In the simulation analysis, it can be pointed out that the short loading condition corresponds to lower loaded amount of soot being the cause of different performances of the solver.

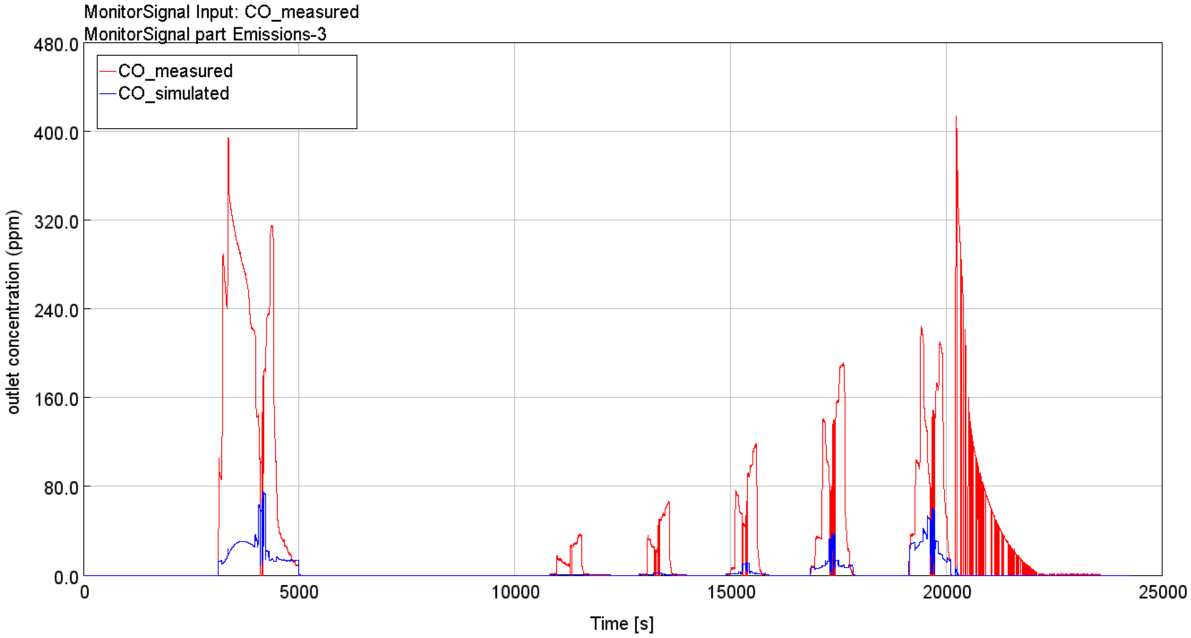

Figure 6.27. CO emissions, silicon carbide filter, short loading conditions: comparison in between measured and simulated data.

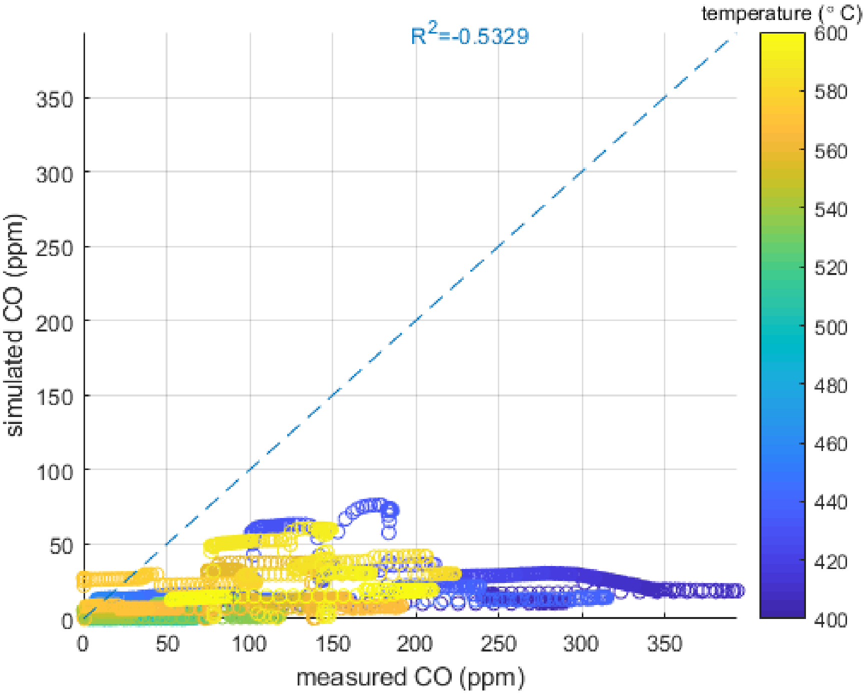

Figure 6.28. CO emissions scatter plot and determination coefficient, silicon carbide filter, short loading conditions.

6.3.2.2 No DOC

Inlet conditions for the experiment are plotted in figure 6.29.

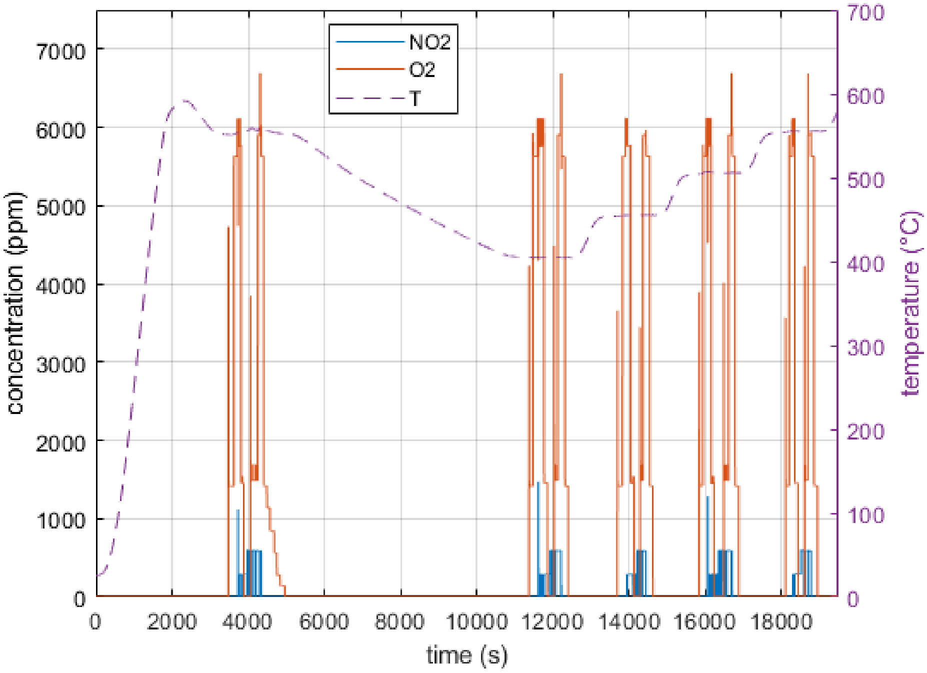

Figure 6.29. Temperature profile and pulses injection sequence for filter #26.

For NO emissions (figure 6.30, scatter plot figure 6.31), the implemented mechanism does not seem able to capture at low temperature the different levels originated by the simultaneous presence of the oxidants, since it is predicting only two levels corresponding to NO_2 injections. At higher temperature, the several levels are highlighted but the trend is quite different from the one observed for experimental data, for which there is a progressive flattening with temperature increase. Again, this can arise from reaction 2.26. It is interesting how in this case the trend is opposite compared to filter #12 model.

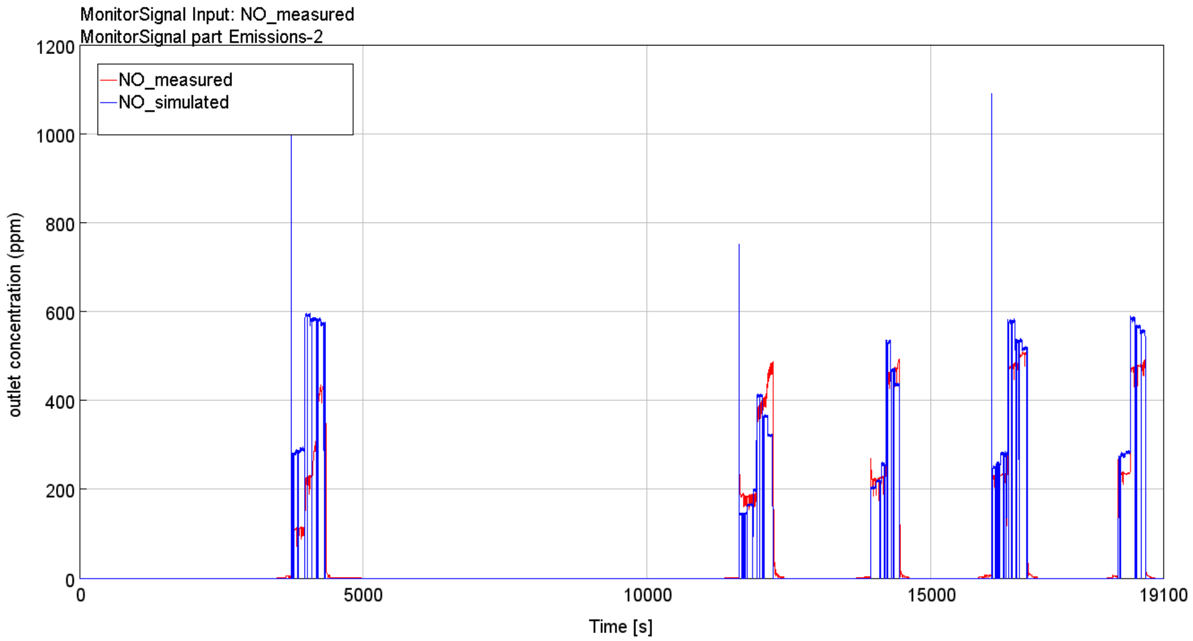

Figure 6.30. NO emissions, silicon carbide filter, no upstream DOC: comparison in between measured and simulated data.

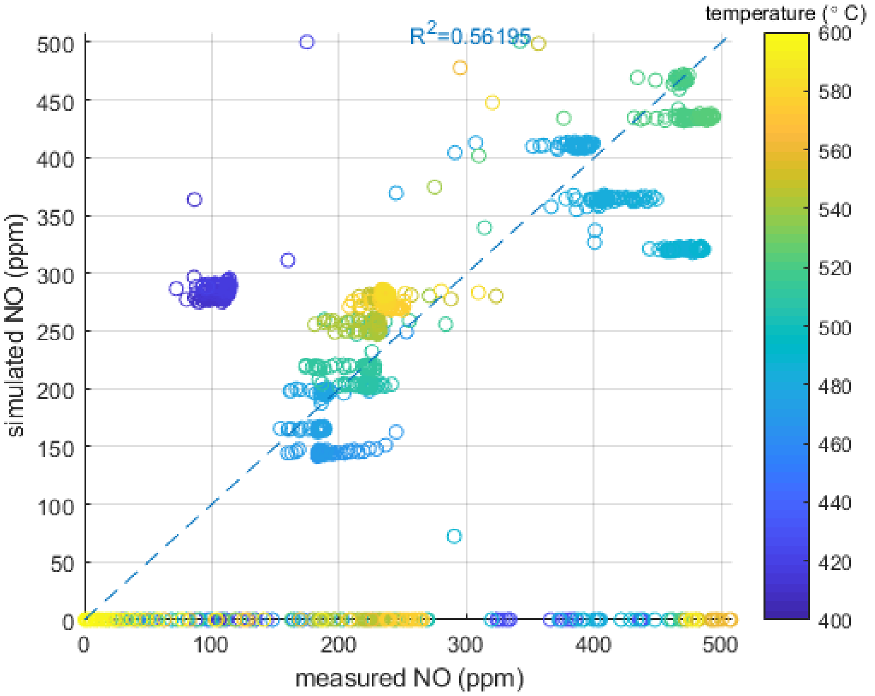

Figure 6.31. NO emissions scatter plot and determination coefficient, silicon carbide filter, no upstream DOC.

CO_2 emission prediction (figure 6.32, scatter plot figure 6.33) is good for the oxygen pathway at low temperature, then subsequent slight underprediction and overprediction for the highest temperature level applied occur. Large underprediction is verified for CO emissions (figure 6.34, scatter plot figure 6.35).

Previous theoretical analysis concluded a lower activation energy for the loading without upstream DOC. This is confirmed by CO_2 simulated trend, since at middle temperatures there is underprediction while overprediction was occurring in the original model.

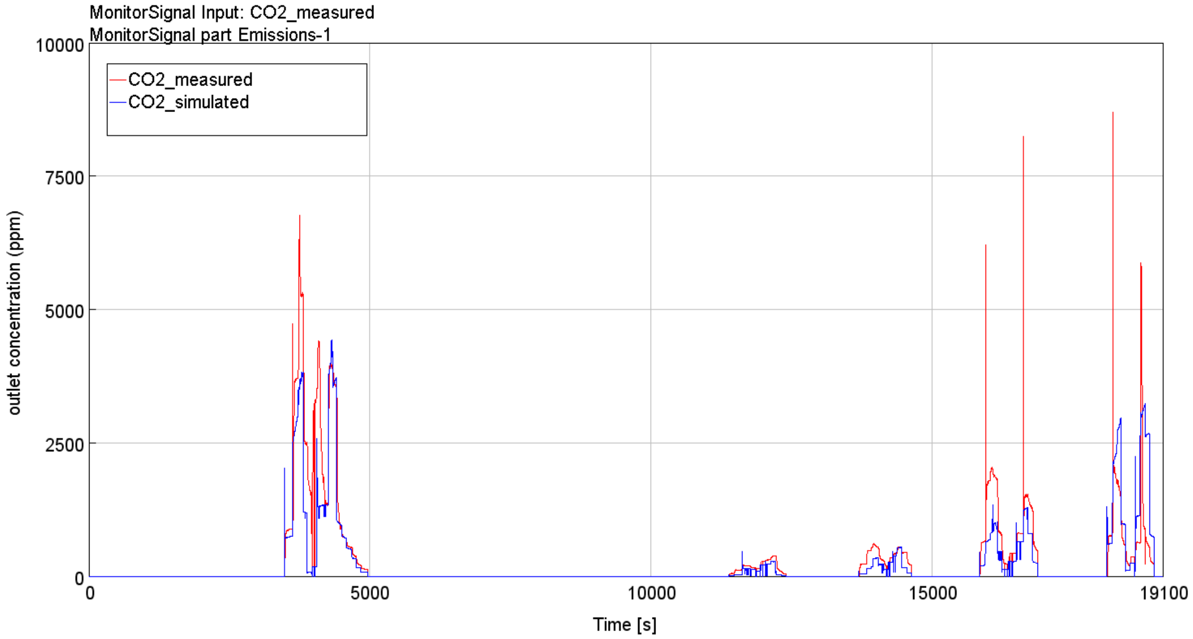

Figure 6.32. CO_2 emissions, silicon carbide filter, no upstream DOC: comparison in between measured and simulated data.

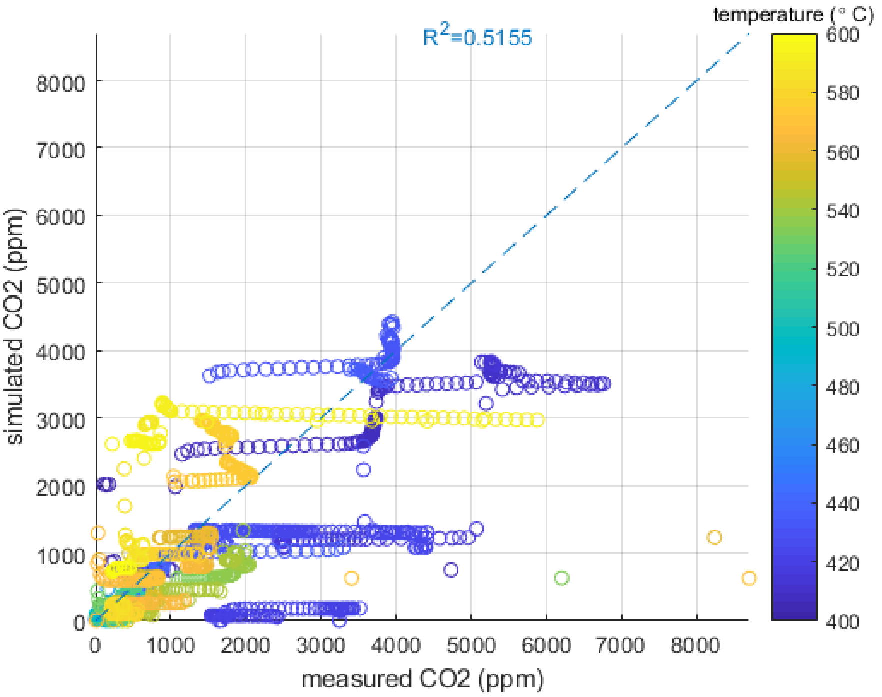

Figure 6.33. CO_2 emissions scatter plot and determination coefficient, silicon carbide filter, no upstream DOC.

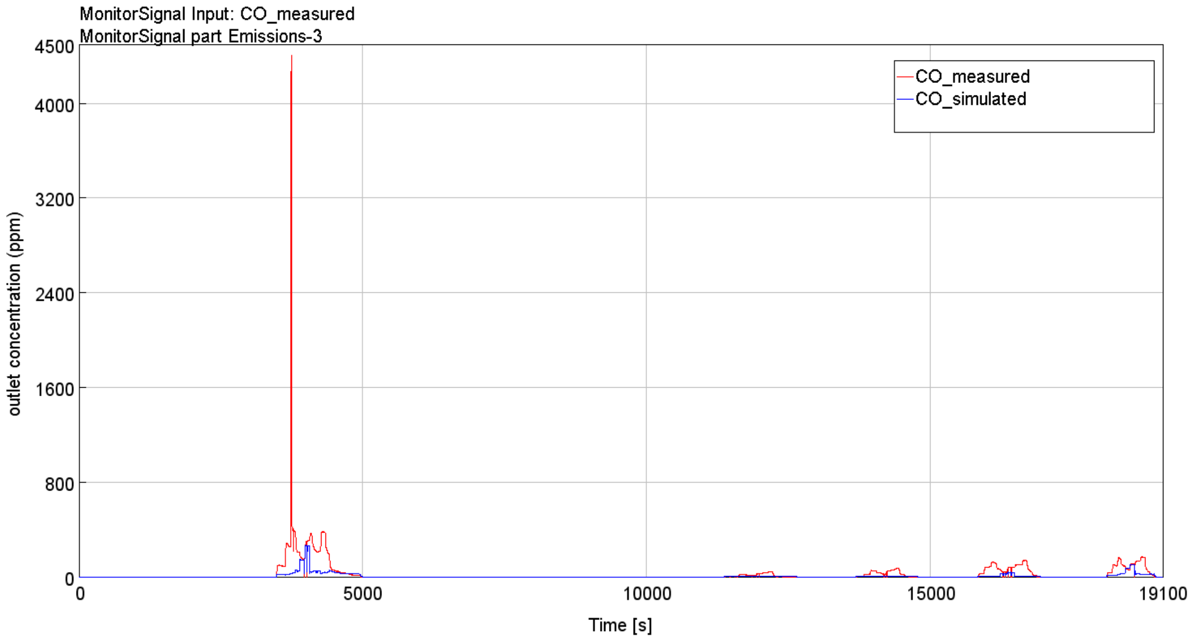

Figure 6.34. CO emissions, silicon carbide filter, no upstream DOC: comparison in between measured and simulated data.

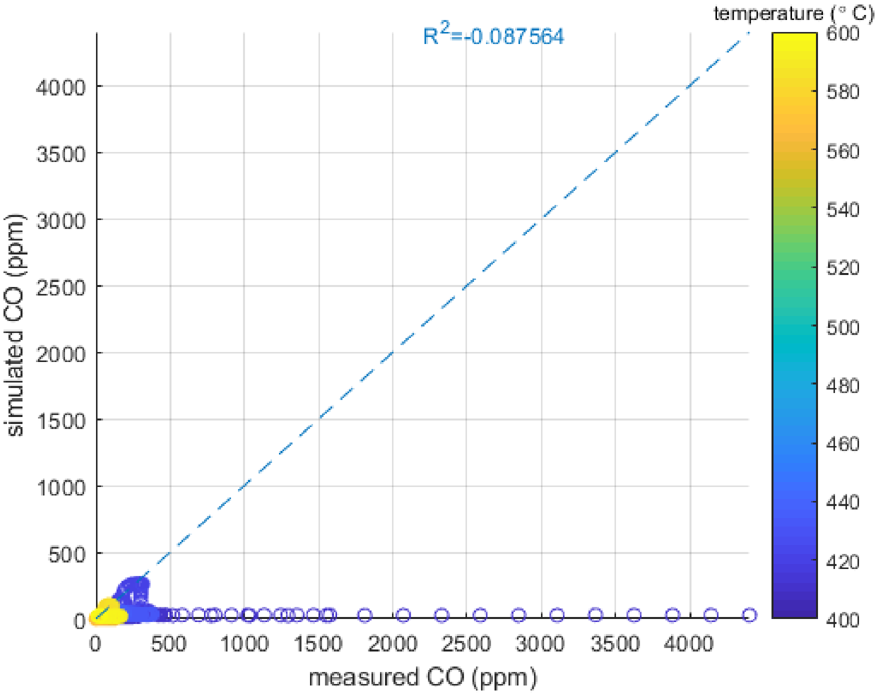

Figure 6.35. CO emissions scatter plot and determination coefficient, silicon carbide filter, no upstream DOC.

It is important to observe that the differences in loading conditions result in different soot physical and chemical characteristics. In the simulation, GT-SUITE default values have been used for soot cake properties due to the absence of soot loading comparison data to carry out an optimization. An interesting continuation for the work would be the tuning of soot parameters in the model with implementation of the same kinetic parameters if providing a sufficiently good solution and solving the previously discussed problems.

6.3.2.3 CeO_2 Catalyst

Once again, experiment no.11 has been selected for kinetic model validation since soot loading conditions are the same as experiment no.12. The SiC filter diameter dimension has been adjusted according to the catalytic coating thickness. No other changes compared to the uncoated filter have been applied to the base model, therefore results may be significantly affected by the change in the thermal properties of the internal wall, which has not been considered. In figure 6.36, the experiment inlet conditions.

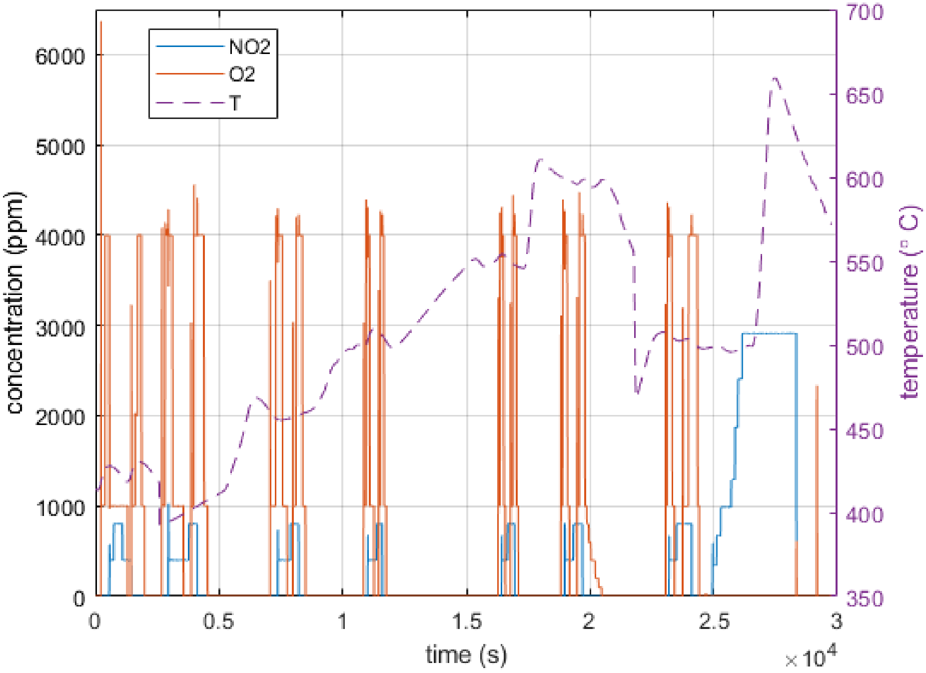

Figure 6.36. Temperature profile and pulses injection sequence for filter #11.

NO prediction (figure 6.37, scatter plot figure 6.38) is surprisingly highly effective, if compared to the previous validations, with slight underprediction at low temperatures and overprediction at high temperatures. The trend follows the one encountered with filter #12. It is important to remember that the loading conditions for the two experiments are identical.

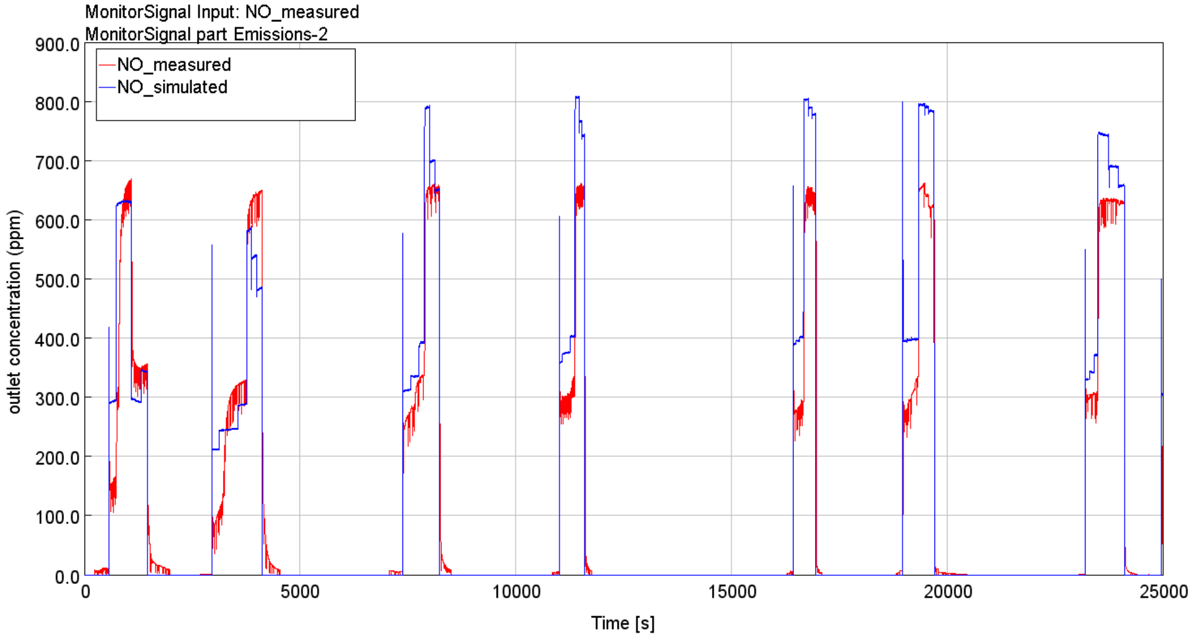

Figure 6.37. NO emissions, ceria-coated silicon carbide filter: comparison in between measured and simulated data.

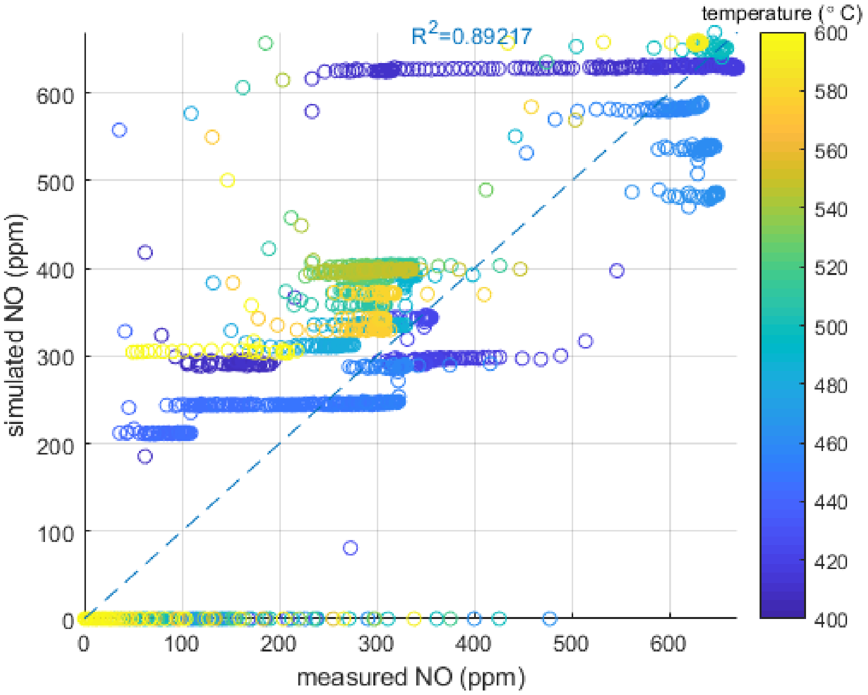

Figure 6.38. NO emissions scatter plot and determination coefficient, ceria-coated silicon carbide filter.

CO_2 (figure 6.39, scatter plot figure 6.40) and CO (figure 6.41, scatter plot figure 6.42) trends are also comparable to CO and CO_2 predictions for experiment no.12. A good fit is obtained also in this case for CO_2 for combined O_2/NO_2 injections, with NO_2 at high level, and O_2-only injections at high temperature. However, as expected, the entity of overprediction is different, since the kinetic parameters have not been modified. The best fit is obtained in this case at around 500°C (after 10000 s), lower compared to what observed for the uncoated filter. The poor error prediction testified by CO_2 determination coefficient R^2 should be ascribed to data collected after 25000 s, for which the inlet conditions were different and the error should not be considered significant.

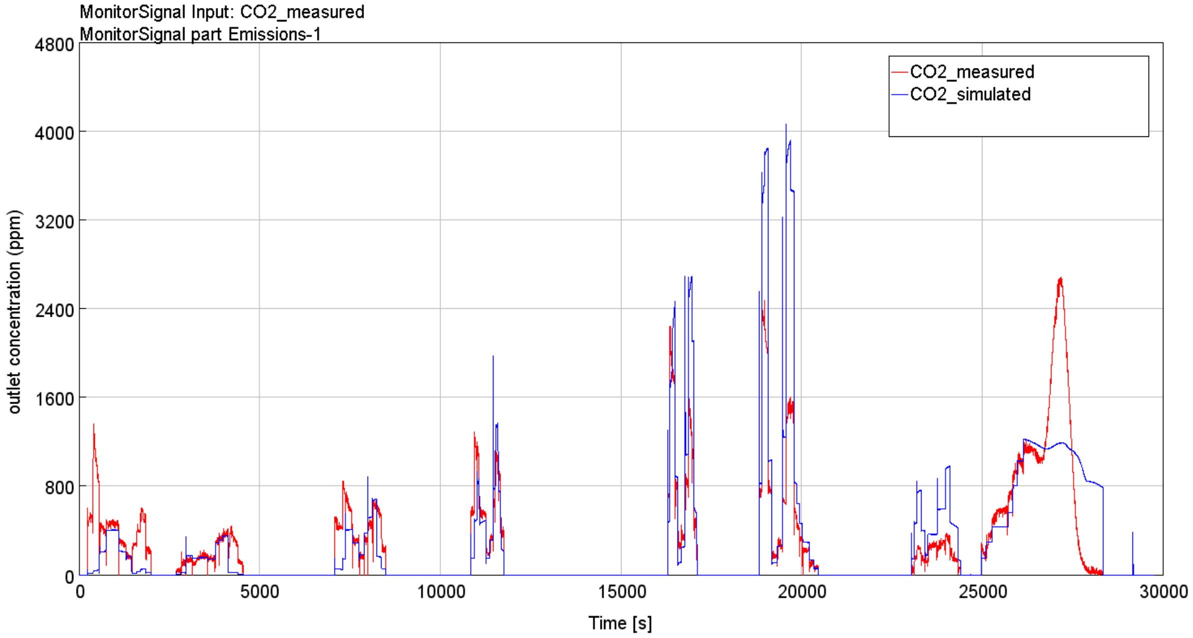

Figure 6.39. CO_2 emissions, ceria-coated silicon carbide filter: comparison in between measured and simulated data.

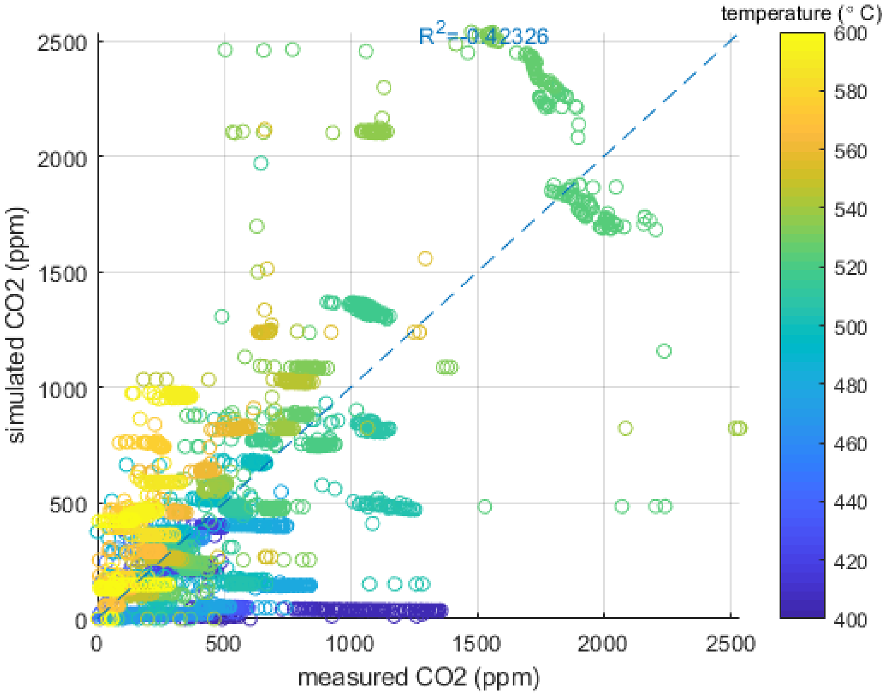

Figure 6.40. CO_2 emissions scatter plot and determination coefficient, ceria-coated silicon carbide filter.

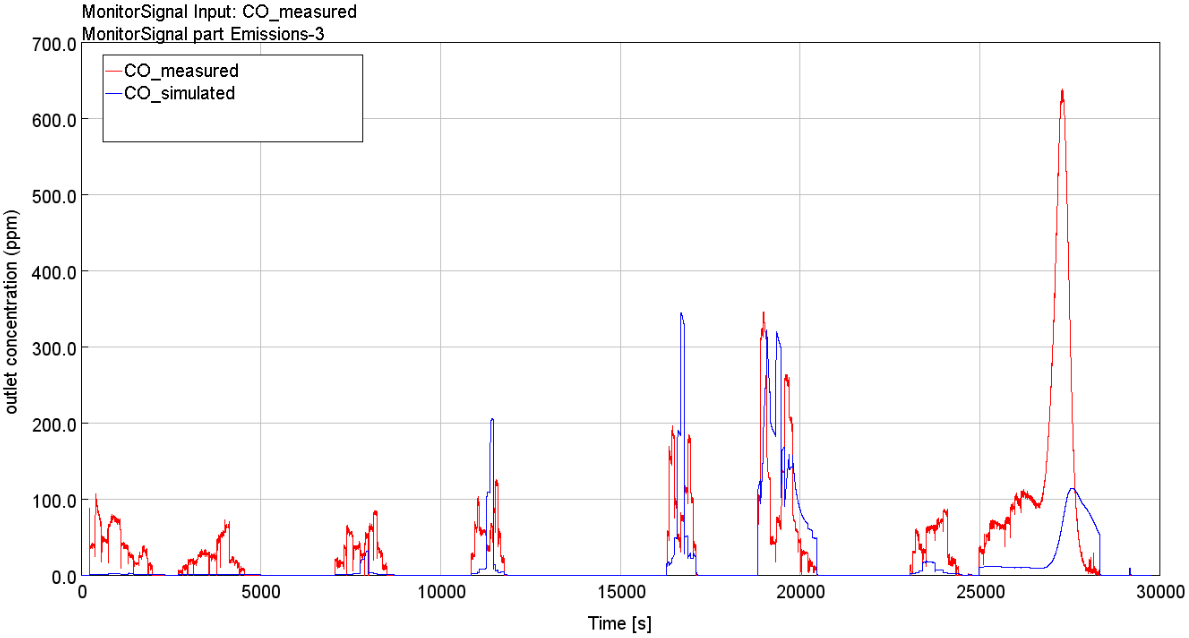

Figure 6.41. CO emissions, ceria-coated silicon carbide filter: comparison in between measured and simulated data.

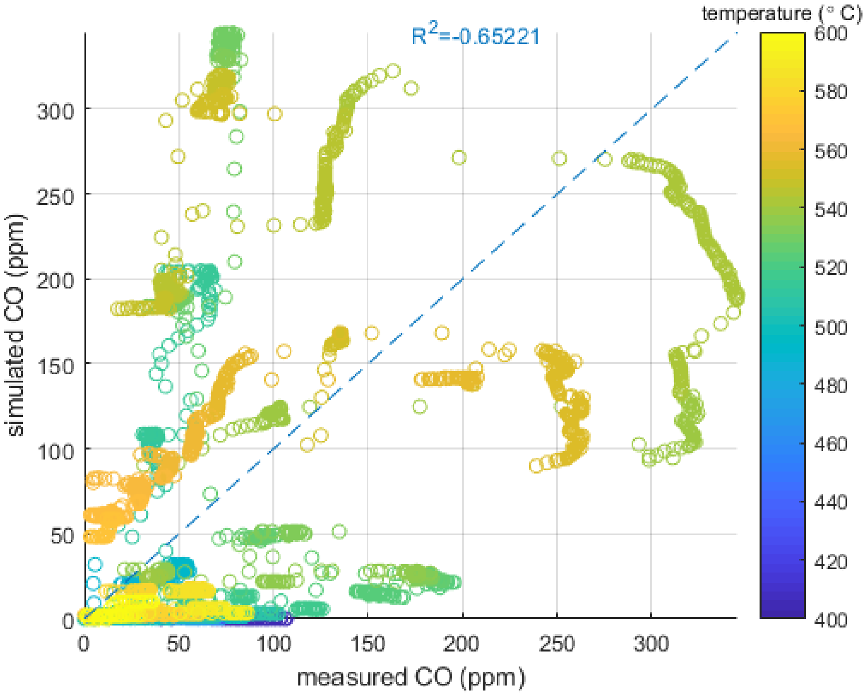

Figure 6.42. CO emissions scatter plot and determination coefficient, ceria-coated silicon carbide filter.

7. Conclusion

The developed work meets the objective of creation of an integrated and flexible model for soot oxidation in DPF under different experimental conditions. Previous models were limited to the exam of single oxidant at defined concentration level. Also, GT-SUITE internal limitations have been overcome satisfactorily. The model predictions are overall good for NO and CO_2 emission trends and less good for CO emission trend. Accuracy needs however to be increased for all simulated species.

It is important to remember that the purpose of the work was not to obtain a faithful reproduction of the experimental results but to get sufficiently accurate results in order to have a deeper insight over soot oxidation reaction mechanism reproducibility. In order to have a more extensive knowledge about phenomena taking part in soot oxidation, a model with more accurate performances is required. Therefore, a deeper analysis of the simulated results is left for when further improvements on the model will be achieved. The same can be said for the analysis of the filter loading conditions.

If the simultaneous presence of different experimental conditions such as nature and levels of the oxidants, temperature, substrates and loading conditions is an advantage on the one hand, it also constitutes a major limit due to the increased complexity of the phenomena taking place. The results show that it is effectively possible to build a flexible model considering different experimental conditions at a glance, however the model fails in accurate prediction of experimental data. It can be concluded that the present work constitutes a good basis for further improvement. In order to achieve better results, several actions are suggested:

- analysis of experimental results for the elaboration of appropriate inhibition functions to be added to the implemented kinetics
- improved reaction scheme linking CO production directly to oxidant concentrations
- calibration of the kinetic parameters in a decoupled way for each species, given the implemented range as starting point
- elaboration of a thermal model for the filter.

The pressure drop and the soot conversion trends deriving from the simulation are considered with some good guess to give satisfactory performances once the kinetic model will give better prediction of experimental results.

Bibliography

[1] Mohankumar S. and Senthilkumar P., 2017, Particulate matter formation and its control methodologies for diesel engine: a comprehensive review. *Renew. Sustain. Energy Rev.*, **80**, 1227–1238.

[2] Gupta T. and Singh D.K., 2016, Organic species emitted as a part of combustion residue: fate and transformation in the ambient air. *J. Energy Environ. Sustain.,* **1**, 10–18.

[3] U.S. Environmental Protection Agency, 2009, Integrated science assessment for particulate matter.

[4] Maricq M. M., 2007, Chemical characterization of particulate emissions from diesel engines: a review. *J. Aerosol Sci.* **38**, 1079–1118.

[5] The European Parliament and the Council of the European Union, 2014, Commission Regulation (EU) No 133/2014 of 31 January 2014. *Official Journal of the European Union*, L47:1–57.

[6] The International Council on Clean Transportation, 2016, A technical summary of Euro 6/VI vehicle emission standards, June 2016, ICCT briefing.

[7] Burtscher H., 2005, Physical characterization of particulate emissions from diesel engines: a review. *J. Aerosol Sci.* **36**, 896–932.

[8] Herner J.D., Robertson W.H. and Ayala A., 2007, Investigation of ultrafine particle number measurements from a clean diesel truck using the european PMP protocol. *SAE International World Congress,* Detroit, Michigan, 16-19 April 2007, SAE technical paper series 2007-01-1114.

[9] Giechaskiel B., Mamakos A., Andersson J., Dilara P., Martini G., Schindler W., and Bergmann A., 2012, Measurement of automotive nonvolatile particle number emissions within the European legislative framework: a review. *Aerosol Sci. Technol.* **46**, 719–749.

[10] Fino D., Bensaid S., Piumetti M. and Russo N., 2016, A review on the catalytic combustion of soot in diesel particulate filters for automotive applications: from powder catalysts to structured reactors. *Appl. Catal. A Gen.* **509**, 75–96.

[11] International Maritime Organization, 2008, Amendments to the annex of the protocol of 1997 to amend the international convention for the prevention of pollution from ships, 1973, as modified by the protocol of 1978 relating thereto (revised Marpol annex VI), Resolution MEPC.176(58).

[12] Zhou J., Zhou S. and Zhu Y., 2017, Characterization of particle and gaseous emissions from marine diesel engines with different fuels and impact of after-treatment technology. *Energies* **10**, 1–14.

[13] Johansen K., 2015, Multi-catalytic soot filtration in automotive and marine applications. *Catal. Today* **258**, 2–10.

[14] Gao J.B., Ma C.C., Xing S.K., Sun L.W. and Huang L.Y., 2018, A review of fundamental factors affecting diesel PM oxidation behaviors. *Sci. China Technol. Sci.* **61**, 330–345.

[15] J F Brilhac J. F., Stanmore B. R. and Gilot P., 2001, The oxidation of soot: a review of experiment, mechanism and models. *Carbon N. Y.* **39**, 2247–2268.

[16] Neeft J.P.A., Nijhuis T.X., 1997, Smakman E., Makkee M. and Moulijn J.A., Kinetics of the oxidation of diesel soot. *Fuel* **76**(12), 1129–1136.

[17] Messerer A., Niessner R. and U. Pöschl U., 2006, Comprehensive kinetic characterization of the oxidation and gasification of model and real diesel soot by nitrogen oxides and oxygen under engine exhaust conditions: measurement, Langmuir-Hinshelwood, and Arrhenius parameters. *Carbon N. Y.* **44**,307–324.

[18] Zhdanov V.P., Carlsson P.A. and Kasemo B., 2008, Kinetics of oxidation of nm-sized soot spherules. *Chem. Phys. Lett.* **454**, 341–344.

[19] Wang-Hansen C., S. Soltani S., and Andersson B., 2013, Kinetic Analysis of O_2- and NO_2-based oxidation of synthetic soot. *J. Phys. Chem. C* **117**, 522–531.

[20] Leistner K., Nicolle A. and Da Costa P., 2012, Detailed kinetic analysis of soot oxidation by NO_2, NO, and NO + O_2. *J. Phys. Chem. C*, **116**, 4642–4654.

[21] Li C. and Trevor C. Brown T.C., 2001, Carbon oxidation kinetics from evolved carbon oxide analysis during temperature-programmed oxidation. *Carbon N.Y.* **39**, 725–732.

[22] Carlsson P.A., 2012, Detailed modeling of carbon oxidation. *J. Phys. Chem. C* **116**, 9063–9071.

[23] Campbell P.A. and Mitchell R.E., 2008, The impact of the distributions of surface oxides and their migration on characterization of the heterogeneous carbon-oxygen reaction. *Combust. Flame* **154**, 47–66.

[24] Setiabudi A., Makkee M. and Moulijn J.A., 2004, The role of NO_2 and O_2 in the accelerated combustion of soot in diesel exhaust gases. *Appl. Catal. B Environ.* **50**, 185–194.

[25] Jeguirim M., Tschamber V., Brilhac J.F., and Ehrburger P., 2004, Interaction mechanism of NO_2 with carbon black: effect of surface oxygen complexes. *J. Anal. Appl. Pyrolysis* **72**, 171–181.

[26] Muckenhuber H. and Grothe H., 2006, The heterogeneous reaction between soot and NO_2 at elevated temperature. *Carbon N. Y.*, **44**, 546–559.

[27] Ishiguro T., Takatori Y. and Akihama K., 1997, Microstructure of diesel soot particles probed by electron microscopy: First observation of inner core and outer shell. *Combust. Flame* **108**, 231–234.

[28] Jung H., David B. Kittelson D.B. and Michael R. Zachariah M.R., 2004, Kinetics and visualization of soot oxidation using transmission electron microscopy. *Combust. Flame*, **136**, 445–456.

[29] Tighe C.J., Twigg M.V., Hayhurst A.N. and Dennis J.S., 2012, The kinetics of oxidation of diesel soots by NO_2. *Combust. Flame* **159**, 77–90.

[30] Strzelec A., Vander Wal R.L., Thompson T.N., Toops T.J. and Daw C.S., 2016, NO_2 oxidation reactivity and burning mode of diesel particulates. *Top. Catal.* **59**, 686–694.

[31] Seong H. and Choi S., 2015, Oxidation-derived maturing process of soot, dependent on O_2-NO_2 mixtures and temperatures. *Carbon N. Y.* **93**, 1068–1076.

[32] Echavarria C.A., Isabel C. Jaramillo I.C., Adel F. Sarofim A.F. and Lighty J.S, 2012, Burnout of soot particles in a two-stage burner with a JP-8 surrogate fuel. *Combust. Flame*, **159**, 2441–2448.

[33] Piumetti M., Van der Linden B., Makkee M., Miceli P., Fino D., Russo N., and Bensaid S., 2016, Contact dynamics for a solid-solid reaction mediated by gas-phase oxygen: Study on the soot oxidation over ceria-based catalysts. *Appl. Catal. B Environ.* **199**, 96–107.

[34] Ström H., Sjöblom J., Kannan A.S., Ojagh H., Sundborg O., and Koegler J., 2018, Near-wall dispersion, deposition and transformation of particles in automotive exhaust gas aftertreatment systems. *Int.J. Heat Fluid Flow* **70**, 171–180.

[35] Gamma Technologies, 2015, GT-SUITE Exhaust aftertreatment application manual, version 2017.

[36] Bueno-López A., 2014, Diesel soot combustion ceria catalysts. *Appl. Catal. B Environ.* **146**, 1–11.

[37] Piumetti M., Bensaid S., Russo N., and Fino D., 2015, Investigations into nanostructured ceria – zirconia catalysts for soot combustion. *Applied Catal. B, Environ.*, **165**, 742–751.

[38] Andana T., Piumetti M., Bensaid S., Veyre L., Thieuleux C., Russo N., Fino D., Quadrelli E.A., and Pirone R., 2017, Ceria-supported small Pt and Pt_3Sn nanoparticles for NO_x assisted soot oxidation. *Appl. Catal. B Environ.* **209**, 295–310.

Appendix A. Optimization

GT-SUITE provides the user an optimizer tool that is able to find local and global error minimums for specified parameters.

When optimizing a large number of parameters, genetic algorithm is the recommended search algorithm. A range for the variables search is imposed and the total number of iterations is calculated as product of the defined population size and generation number. Population size is determined proportionally to the number of independent variables, while the number of generations is often initially set to the value of 10 and then increased for refined optimizations. The objective for the optimizer is the minimization of a total error function defined as in equation A.1:

$$\sum_{i=1}^{K} \int_{D}^{t} (\text{measured} - \text{sensed})^2 dt \tag{A.1}$$

where K is the total sensed species and D is the dwell duration.

In specific, the measured emissions data for CO, CO_2 and NO have been fed to the error function definition. The dwell duration has been set to 8000 s. During optimization, the simulation time step has been set to 20 s in order to speed up the computation.

The optimization procedure has been described in the previous chapter. Sensitivity and parameters trend during the several optimizations for kinetics are here reported.

Estimated sensitivity for pre-exponential factors during the first optimization is plotted in figure A.1.

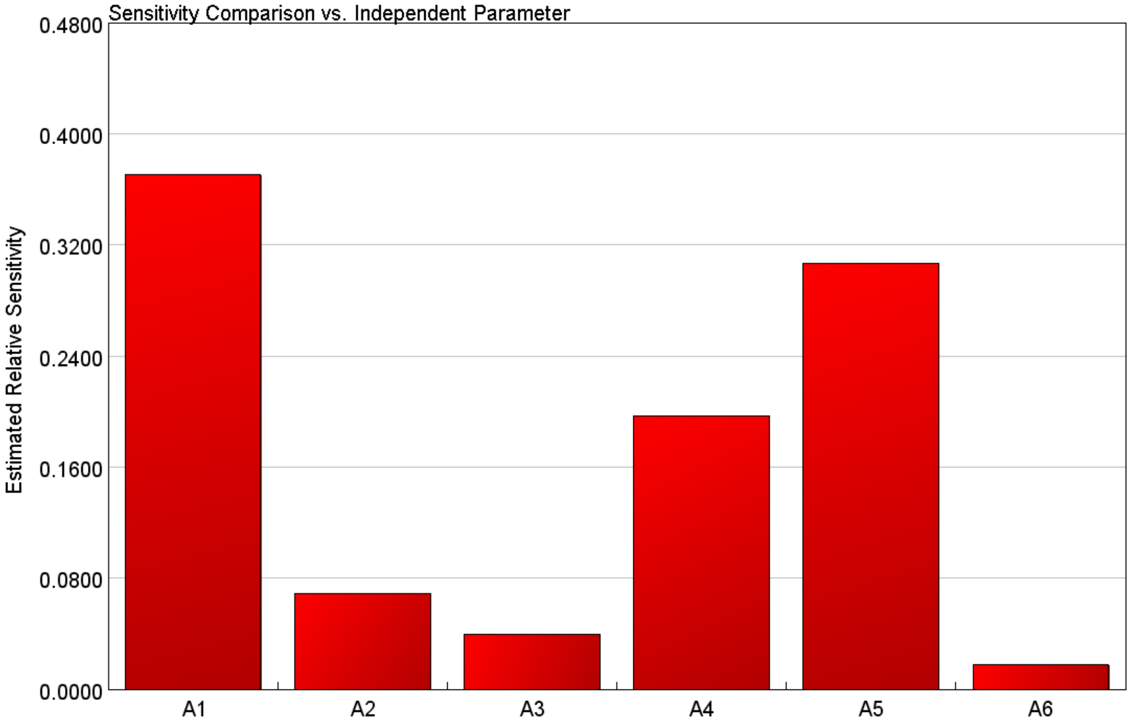

Figure A.1. Sensitivity plot for the pre-exponential factor values after the first optimization.

The values that are affecting the most the result of the first optimization are A_1, A_4 and A_5, respectively the pre-exponential factors for O_2-assisted oxidation and CO and CO_2 desorption (in the latter case, O_2-aided desorption).

The optimization plots are also reported in figures A.2-A4. The values in the vertical axes need to be considered as exponential values, or pre-exponential values are defined as $A_i=10^{Ai}$.

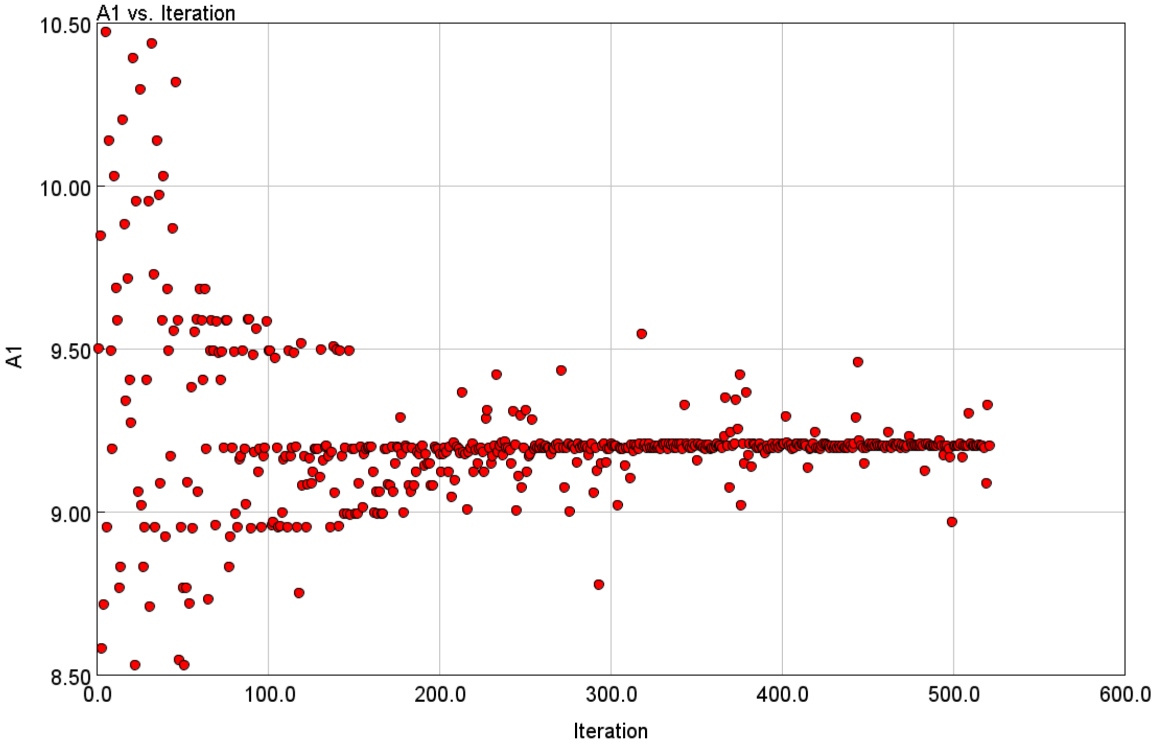

Figure A.2. Optimization plot for A_1.

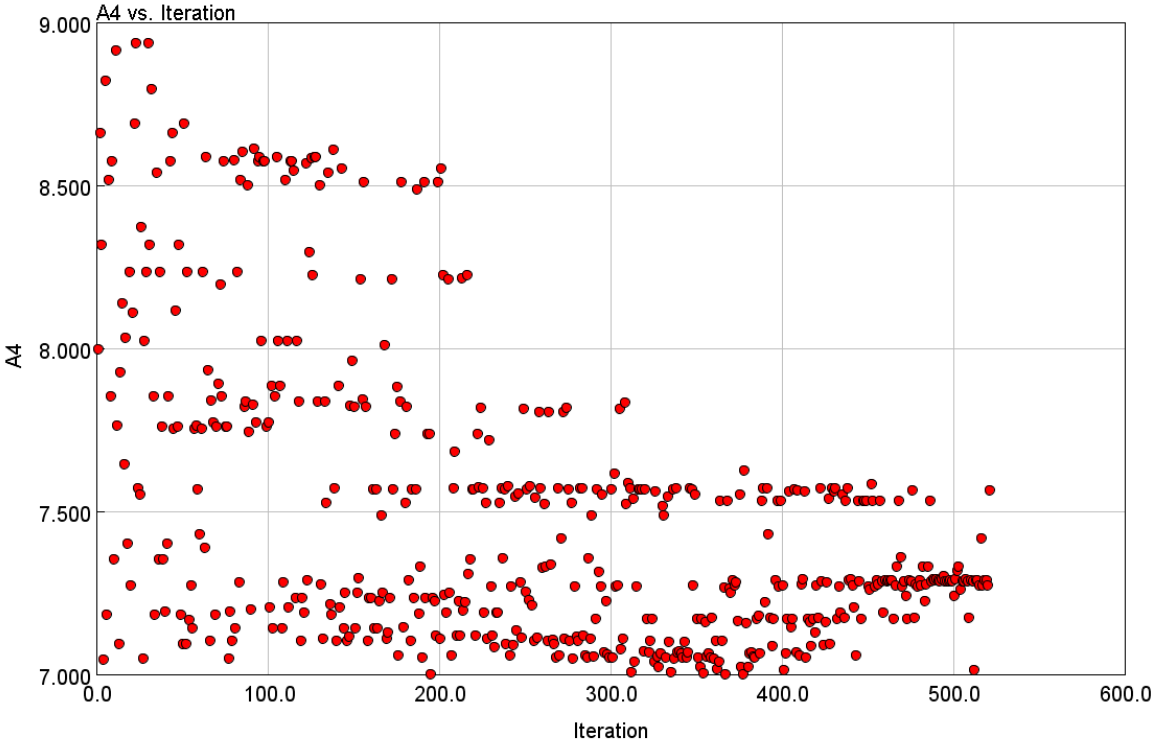

Figure A.3. Optimization plot for A_4.

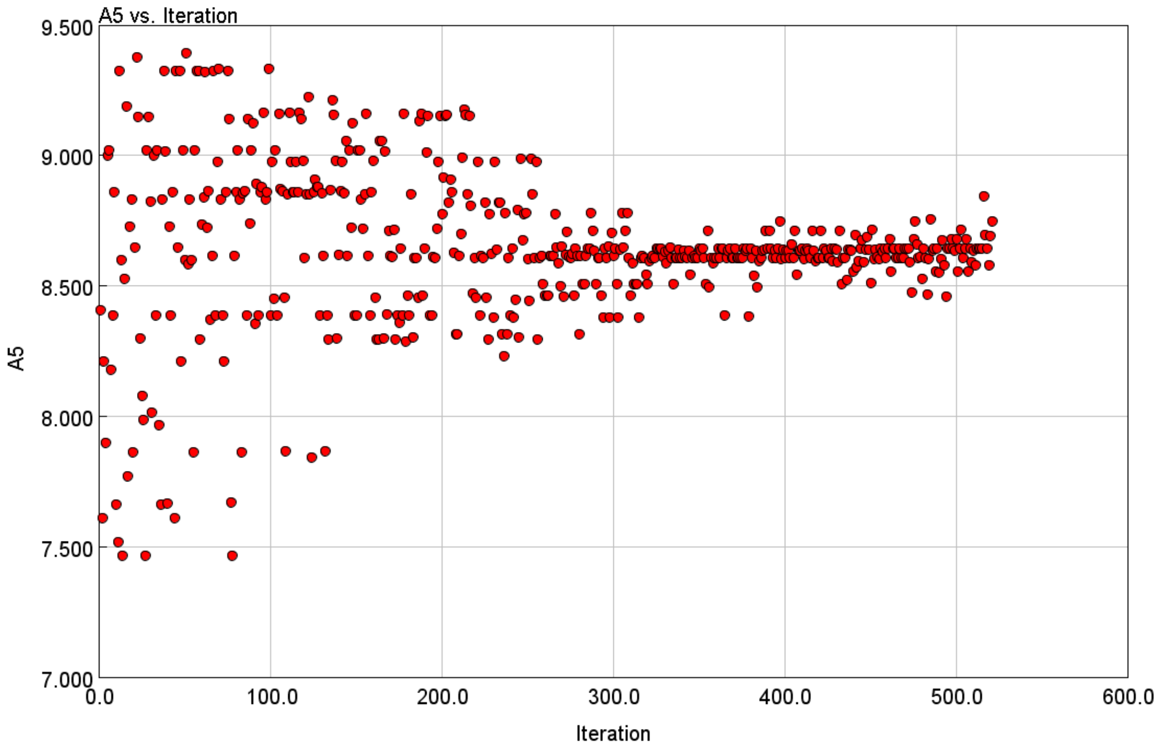

Figure A.4. Optimization plot for A_5.

It can be seen that parameter A_1 has converged during the optimization, however some scatter remains. The optimization of the parameter A_4 highlights a bimodal trend, therefore full convergence has not been reached within the programmed iterations. Pre-exponential factor A_5 has converged with a certain scattering.

Since activation energy is a parameter that needs careful tuning, the optimization has been practically carried out on a multiplier e_i applied to each first-guess value. The variation allowed for e factor during optimization is therefore small. Sensitivity for this parameter during the second optimization round is plotted in figure A.5.

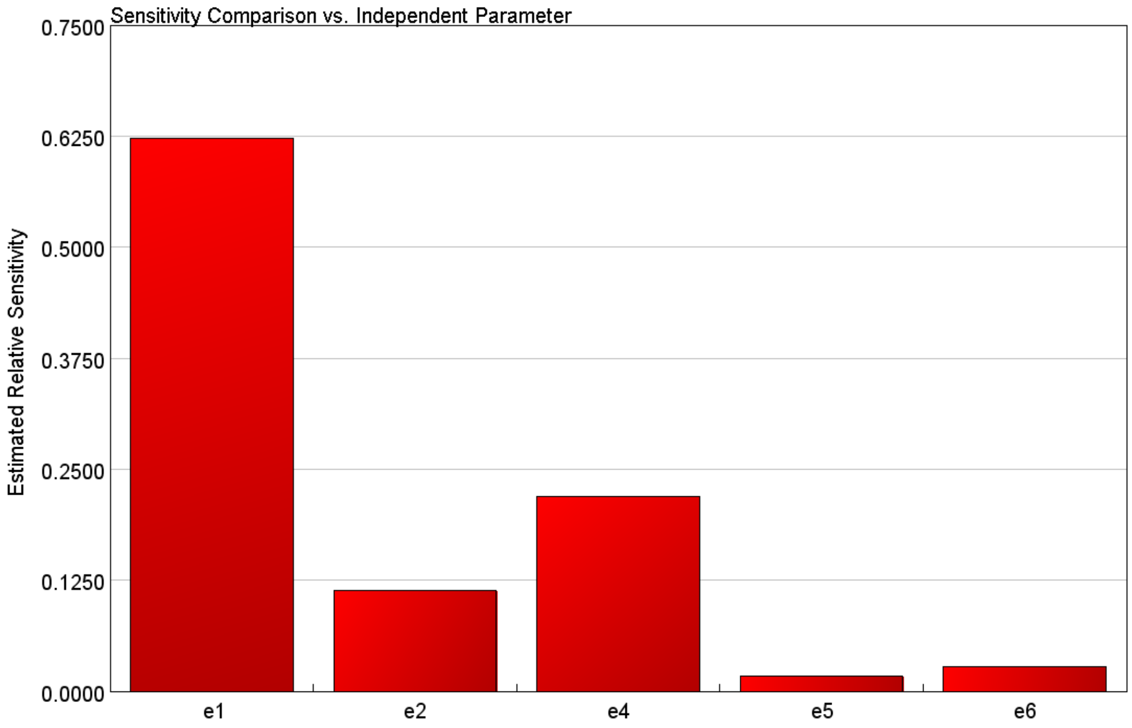

Figure A.5. Sensitivity plot for the activation energies multipliers after the second optimization.

The most sensitive activation energy variations occur for e_1 and e_4 (optimization plots in figures A.6-A.7). Again, oxygen reaction with soot is determining for the entire mechanism.

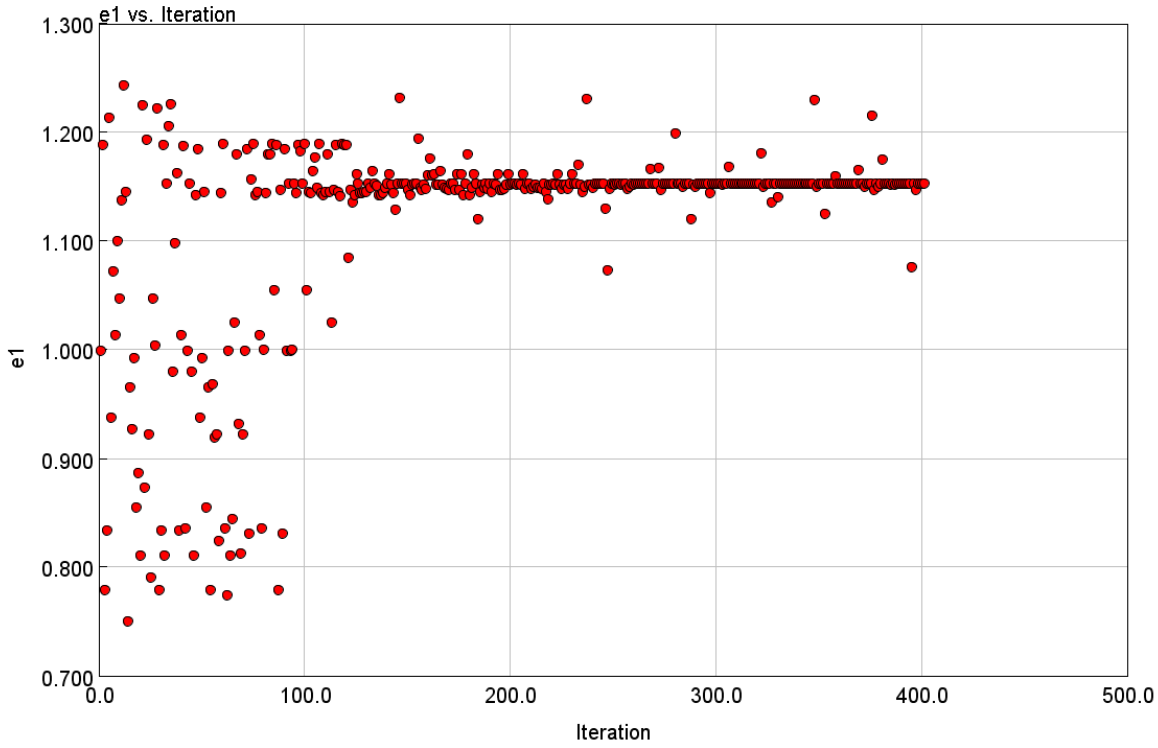

Figure A.6. Optimization plot for e_1.

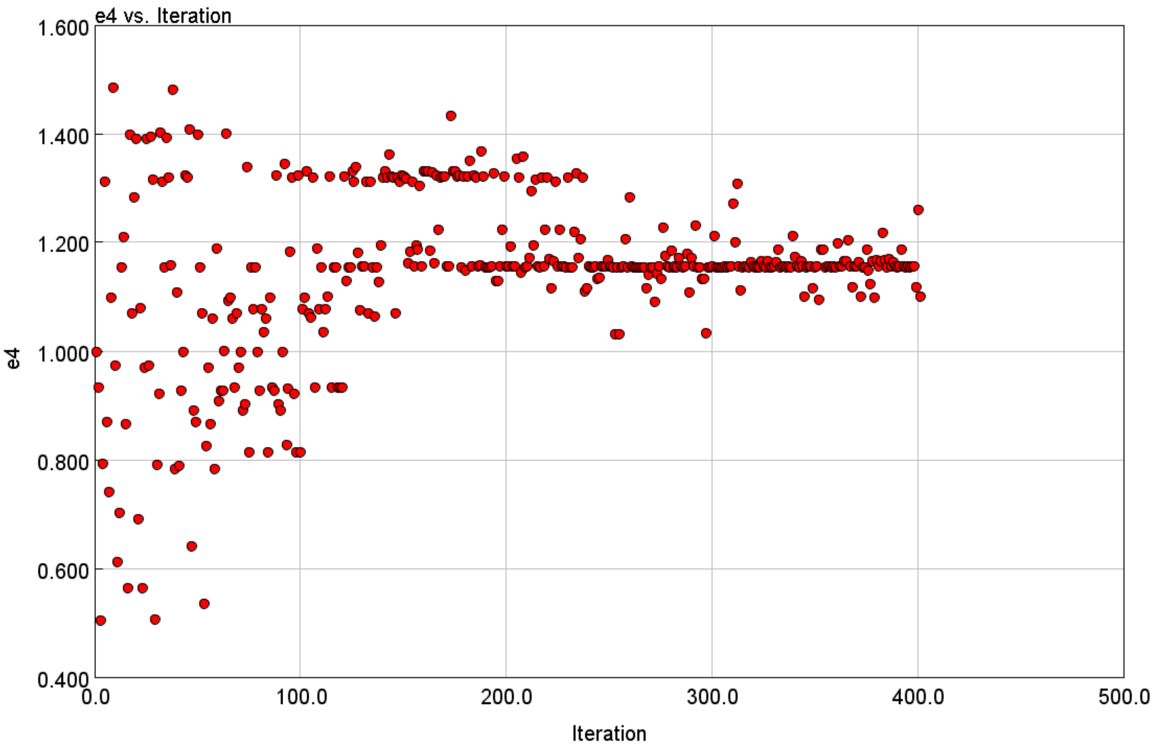

Figure A.7. Optimization plot for e_4.

Both parameters show good convergence with small scattering. It is important to repeat that the variation for the activation energy value is relatively small.

Pre-exponential factors have been optimized with the corrected values for activation energy, the sensibility of the optimization resulting in figure A.8. The parameters range for this last optimization has been narrowed.

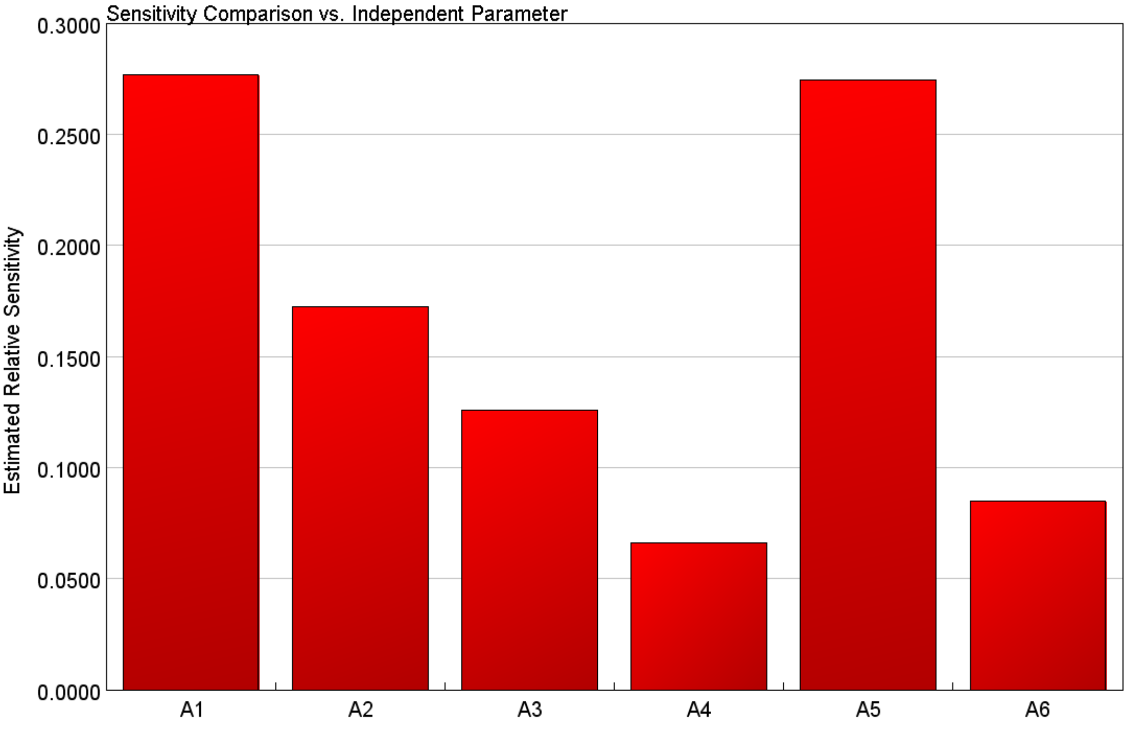

Figure A.8. Sensitivity plot for the pre-exponential values after the third optimization.

The sensitivity of the optimization is still high for A_1 and A_5, as in the first procedure, however A_2 and A_3 appear to be strongly affecting the calculated error. Optimization plots are reported in figures A.9-A.12.

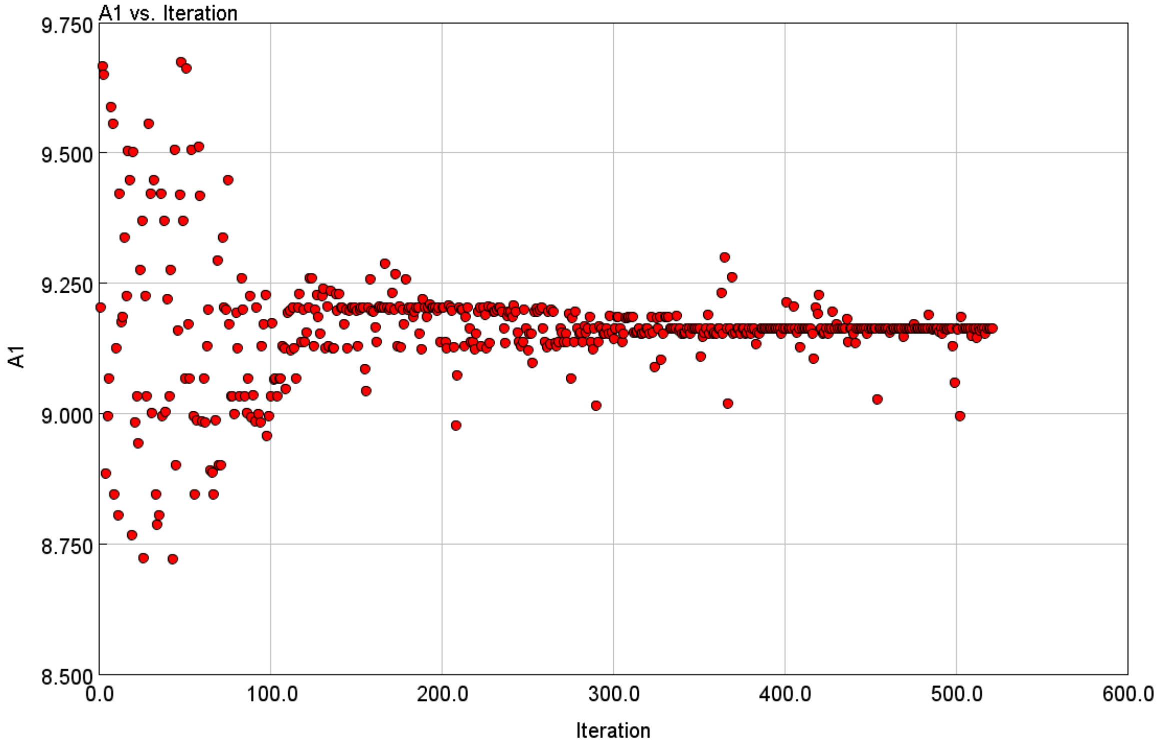

Figure A.9. Second optimization plot for A_1.

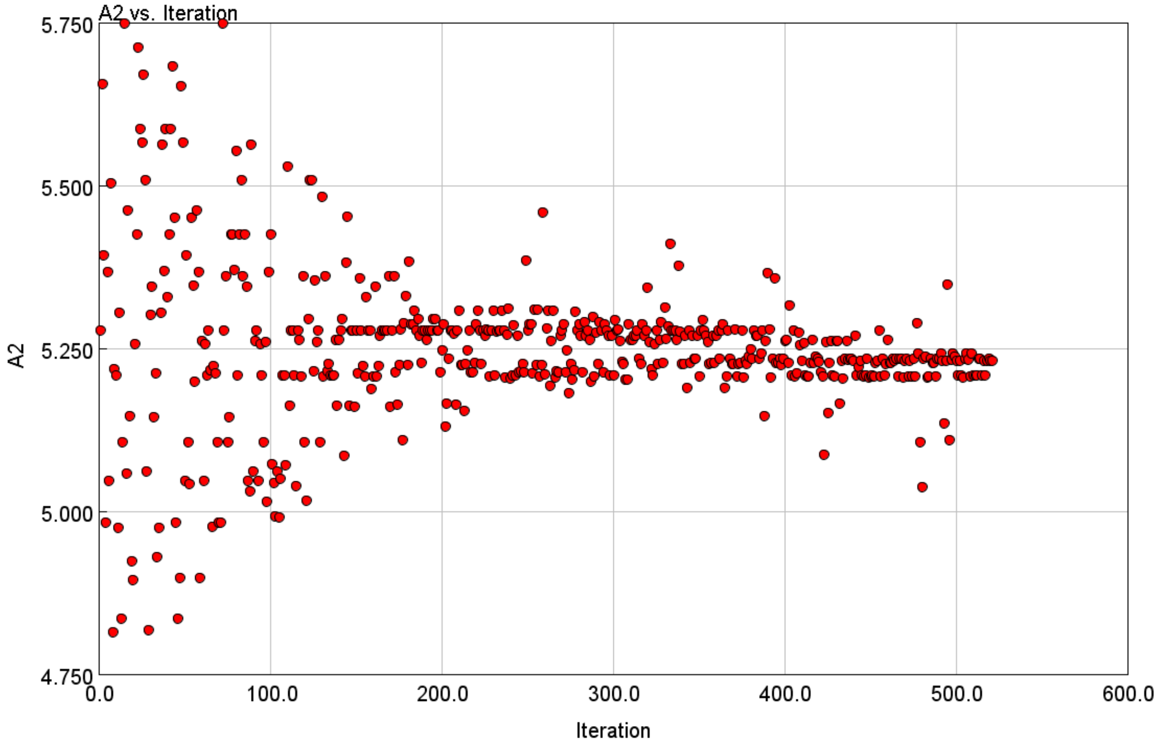

Figure A.10. Second optimization plot for A_2.

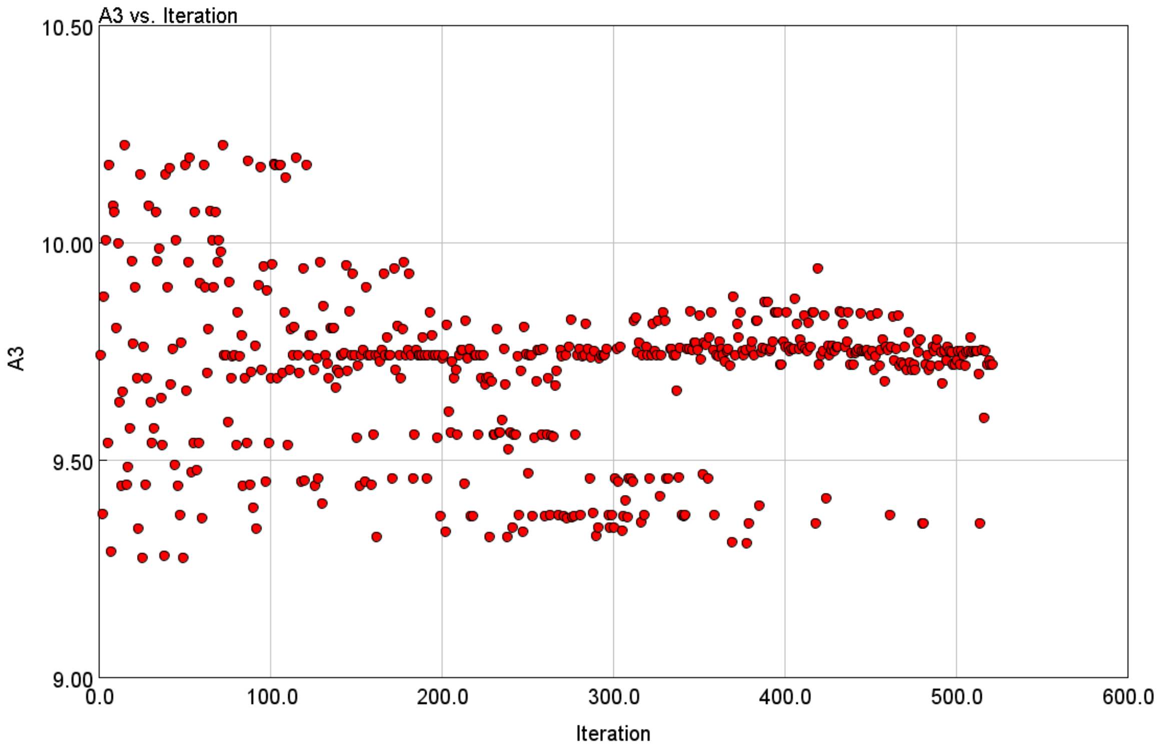

Figure A.11. Second optimization plot for A_3.

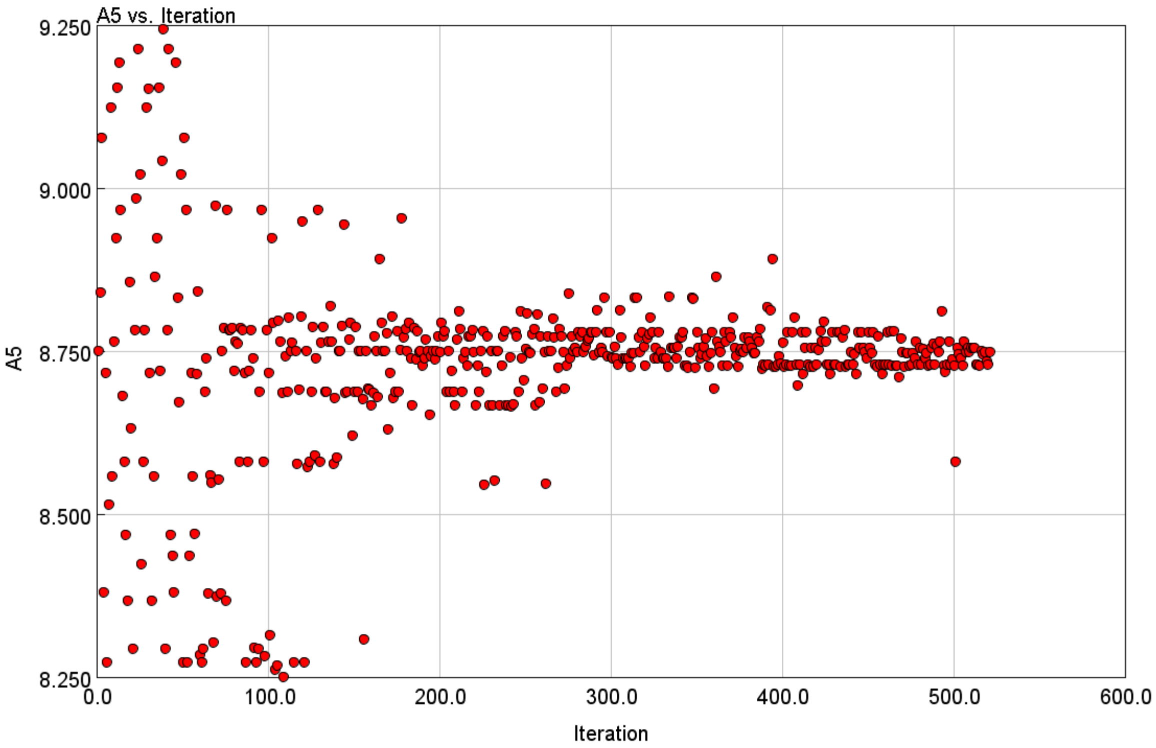

Figure A.12. Second optimization plot for A_5.

Parameter A_1 shows good convergence, while A_2, A_3 and A_5 seem to need some further refinement to reach full convergence. It is important to notice that pre-exponential factors have been defined in the simulation as exponential parameters, 10^{Ai}, therefore a small variation for A_i is significant in the results.

The optimization results show the importance of the oxygen-aided oxidation reaction in the mechanism, even if convergence for both pre-exponential factor and activation energy is obtained. The magnitude of the searching range during each optimization has been defined equally for all the kinetic parameters involved.

The sensitivity plots also point out the synergistic effect of the several parameters for determining the final result. Unless a very good range for some parameters is used during refined optimizations, it is not possible to consider some of the reactions alone.

Appendix B. Arrhenius Analysis

Arrhenius analysis has been performed on the results obtained for the original experiment no.12 in order to examine the performances and try to point out the issues linked to the model for future work.

Outlet experimental and simulated data have been captured at proper time instants for the sequence of the steady-state oxidant levels applied. The analysis has been carried out separately for CO and CO_2 and the nature of oxidant species is distinguished. O_2, NO_2 alone and coexistence of both oxidants are considered as different cases in the plots. Also, NO_2 decomposition equilibrium to NO and O_2 has been taken into account in the latter case since, according to the applied oxygen levels, NO_2 concentration can differ from the imposed 400 and 800 ppm values for this reason in the analysed temperature range, as shown in figure B.1.

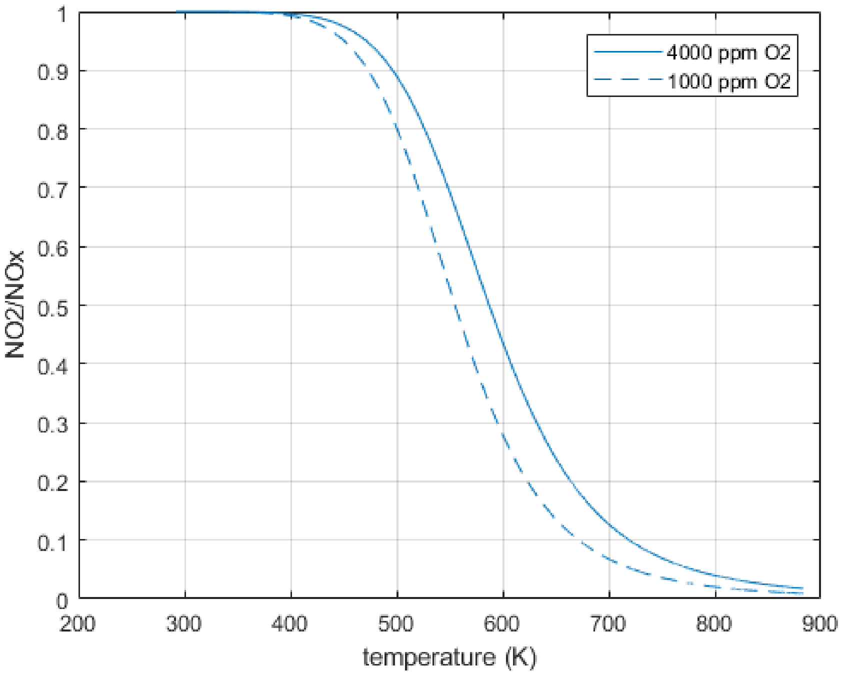

Figure B.1. NO_2/NO_x ratio for the analysed temperature range for the high and low oxygen levels.

Normalized reaction rates have been defined as in the set of equations B.1-B.6.

$$r_{CO,O_2} = \frac{[CO]}{{y_{O_2}}^{0.8}[C]^{2/3}} \tag{B.1}$$

$$r_{CO_2,O_2} = \frac{[CO_2]}{{y_{O_2}}^{0.8}[C]^{2/3}} \tag{B.2}$$

$$r_{CO,NO_2} = \frac{[CO]}{y_{NO_2}[C]^{2/3}} \tag{B.3}$$

$$r_{CO_2,NO_2} = \frac{[CO_2]}{y_{NO_2}[C]^{2/3}} \tag{B.4}$$

$$r_{CO,O_2,NO_2} = \frac{[CO]}{{y_{O_2}}^{0.8}y_{NO_2}[C]^{2/3}} \tag{B.5}$$

$$r_{CO_2,O_2,NO_2} = \frac{[CO_2]}{{y_{O_2}}^{0.8} y_{NO_2} [C]^{2/3}} \tag{B.6}$$

where [CO], [CO_2] are measured as outlet molar flow per unit reactor volume (mol $m^{-3}s^{-1}$). [C] term considers the reaction advancement and it is measured as soot mass in the soot cake per unit reactor volume (g dm^{-1}).

Logarithm of the normalized reaction rate is plotted against reciprocate of the absolute temperature (K^{-1}) in the figures B.2-B.7 for experimental and simulated data.

Normalization has been carried out on reaction rates in order to obtain results independent from the conversion parameter and the oxidant concentration levels. The mathematical expressions used are the same implemented in the kinetic model for the simulation, deriving from previous theoretical analysis. From the experimental data, a straight line is expected. However, as it can be seen in the plots, the normalization is not always effective. It is important to mention that in the previous analysis the single oxidant levels were considered separately when determining the specific kinetic expression. Also, effects such as mass transfer resistance can be identified at this stage. As mentioned in the dedicated chapter, literature reports significant diffusion resistance in the soot porous particle for O_2 species.

Therefore, the use of the model in a generalized form in some cases is not capturing the real mechanism.

The scope of the Arrhenius analysis is also the comparison in between experimental and simulated results, in order to have better information regarding the model prediction effectiveness.

For CO (figure B.2), normalization for the kinetic pathway with oxygen shows to be valid at high temperatures. The linear trend shows to be almost the same for the whole temperature span. The simulated data show a bimodal trend according to the two oxygen levels for all temperatures and a relevant difference for the slopes, corresponding to activation energies. For CO_2 (figure B.3) the slope prediction from the simulated data is better. The linear trend for experimental data is different at low and high temperatures and the normalization is only effective at high temperatures, as in the previous case.

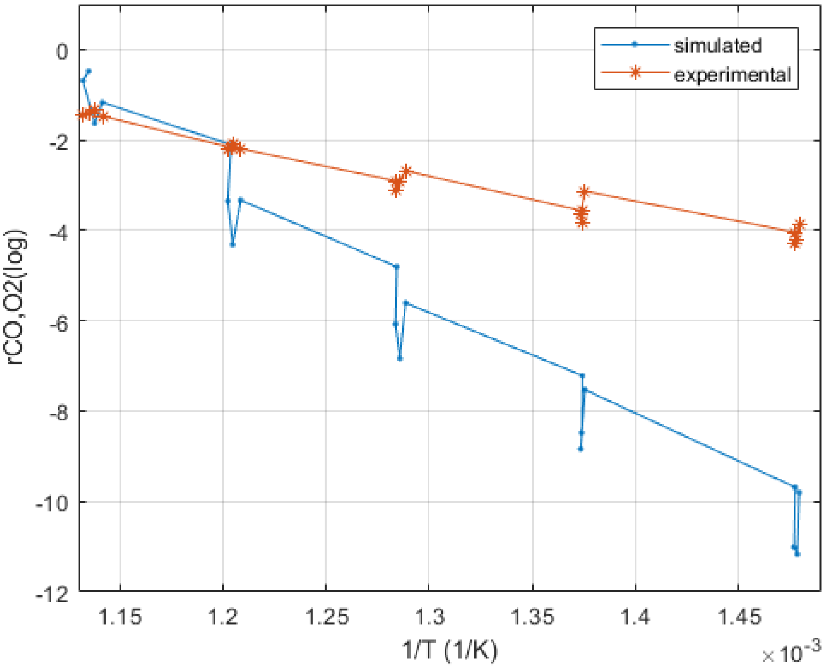

Figure B.2. Arrhenius plot for CO production rate in the presence of O_2: comparison in between experimental and simulated data.

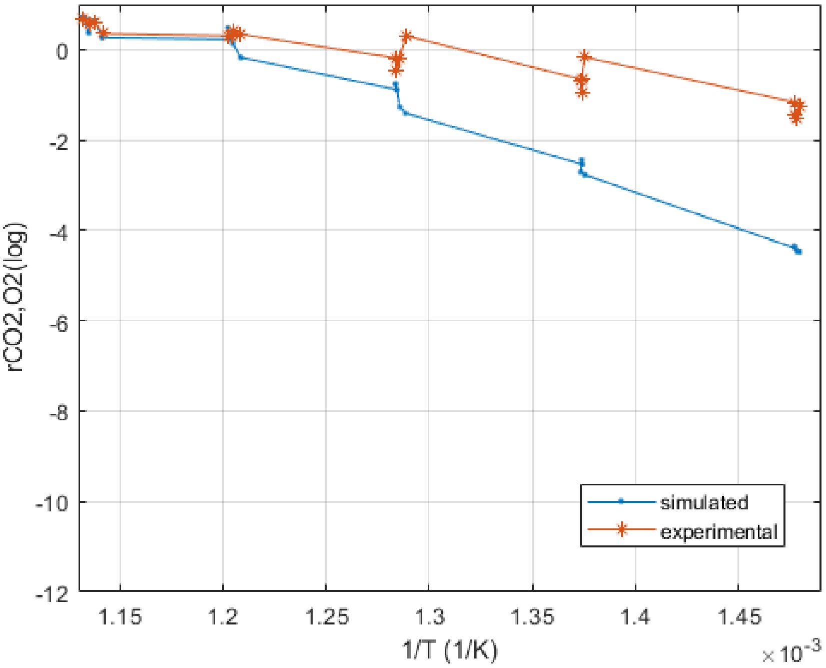

Figure B.3. Arrhenius plot for CO_2 production rate in the presence of O_2: comparison in between experimental and simulated data.

Looking at the kinetic pathway with NO_2, for CO production rate (figure B.4) the normalization of experimental data is working approximately well for the whole temperature range and the slope is slightly changed at lower temperatures. The normalization is captured surprisingly well for simulated data, however activation energy is significantly different in between the two curves. Also, a relevant change in the slope at low temperature appears for simulated data, meaning that other phenomena are taking place, except for chemical reactions.

CO_2 normalization for NO_2 oxidation is not good for experimental data (figure B.5). The reaction rate seems to be constant and even decreasing at high temperature for simulated data, which is not physically meaningful. Instead, the trend is due to bad CO/CO_2 selectivity prediction at high temperature.

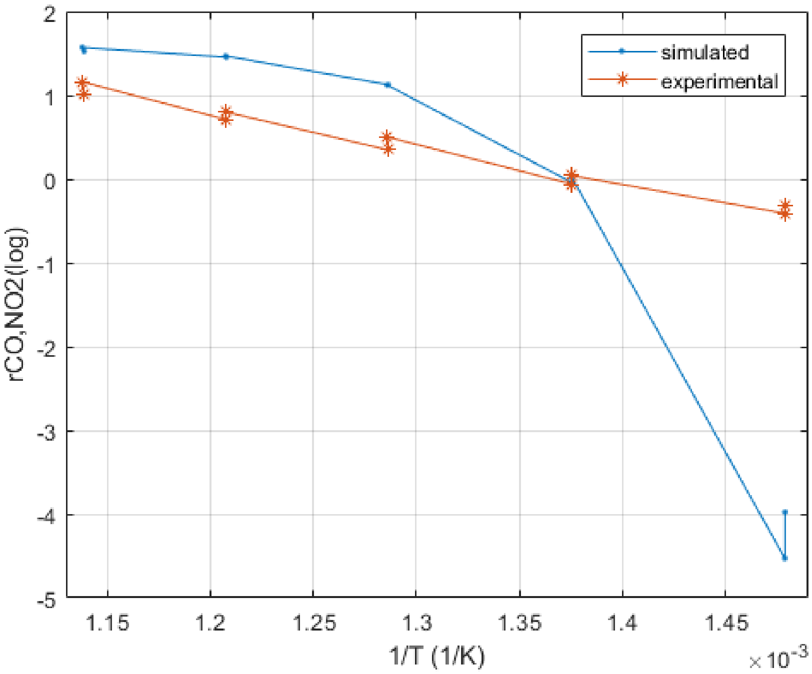

Figure B.4. Arrhenius plot for CO production rate in the presence of NO_2: comparison in between experimental and simulated data.

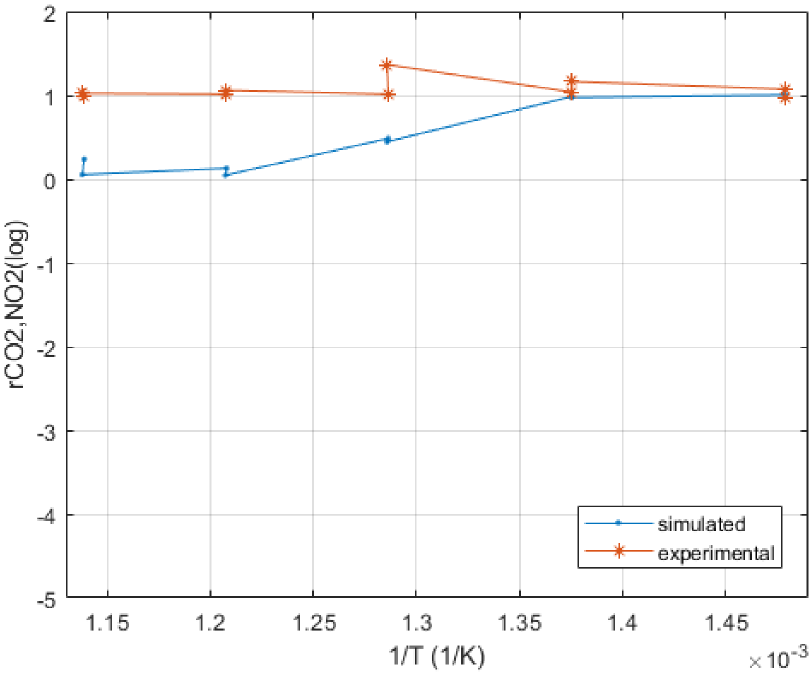

Figure B.5. Arrhenius plot for CO_2 production rate in the presence of NO_2: comparison in between experimental and simulated data.

When both oxidants are present, the imposed kinetics shows a bimodal fit according to the two nitrogen dioxide levels (figure B.6-B.7). For O_2 the normalization is instead well captured with the imposed kinetics at low temperatures, less accurately at high temperatures. The activation energy seems to be constant for CO_2 production while for CO the linear trend seems to be slightly different at low temperatures. Good fit is observed in between experimental and simulation data for the activation energy for CO_2 production rate especially at high temperatures.

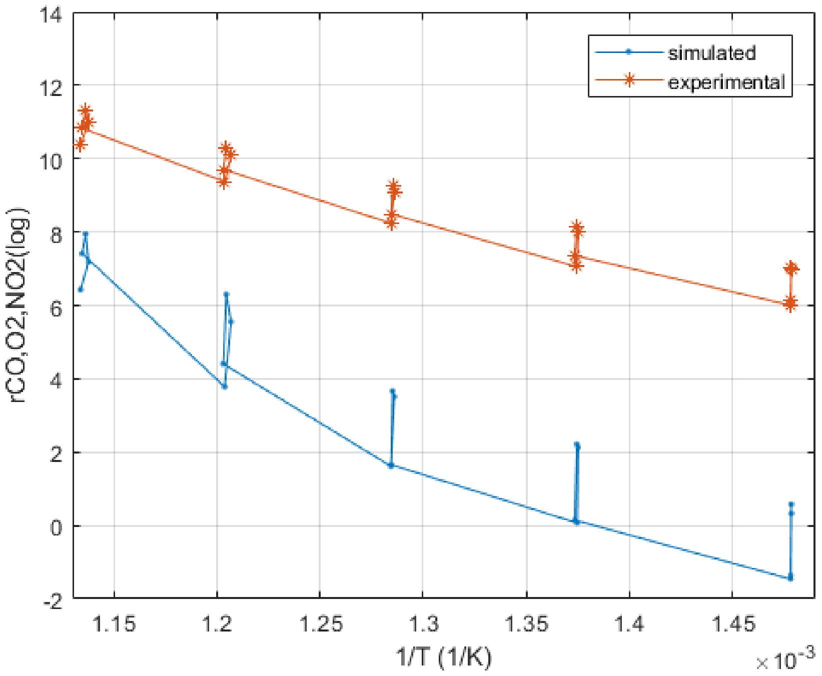

Figure B.6. Arrhenius plot for CO production rate in the simultaneous presence of O_2 and NO_2: comparison in between experimental and simulated data.

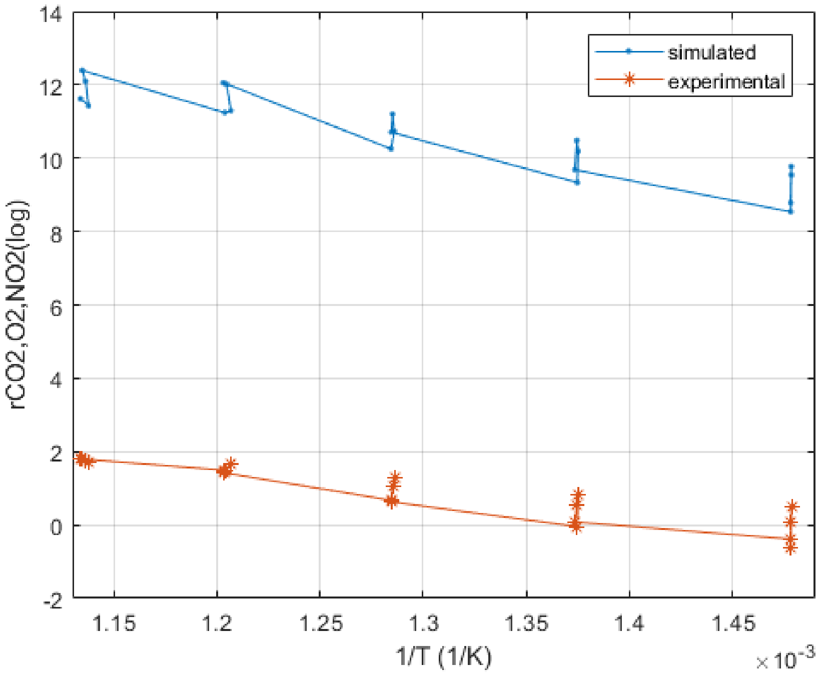

Figure B.7. Arrhenius plot for CO_2 production rate in the simultaneous presence of O_2 and NO_2: comparison in between experimental and simulated data.

Arrhenius analysis appears to be important for evaluating the effectiveness of a kinetic model. The applied model has proven to be not always good for predicting the system behaviour when input conditions are changed, or the oxidant concentration levels. In order to get a better fit in between experimental and simulated data, a more complicate kinetic model is needed with the definition of proper inhibition functions that are able to "correct" the deviations of experimental results from the proposed model.

A major finding from the analysis is the adequateness for the description of O_2 and NO_2 simultaneous effect and, in particular, the activation energy prediction for CO_2 production rate is satisfactory.

It is also important to remember that for the simulation, surface kinetics has been implemented, therefore the deviation in between the experimental and simulated plots must be ascribed to some possible issues occurring with this reaction scheme. The global kinetics was excluded due to bad predictions when both oxidants were applied. Performances of the surface scheme are good for the combined oxidant effect instead, but they still need improvement when a single oxidant is fed.

Ringraziamenti

Il progetto è stato realizzato nell'ambito del programma Erasmus+ per mezzo di accordi fra la Chalmers University of Technology di Göteborg e il Politecnico di Torino.

Sono molto riconoscente per aver avuto la possibilità di realizzare questo lavoro presso la Chalmers University of Technology. Ho avuto modo di apprezzare la formazione complementare e diversificata in entrambe le università.

Vorrei ringraziare in particolare il mio supervisore Jonas Sjöblom, per avermi dato l'opportunità di lavorare su un argomento complesso ma ricco di sfide. I continui e proficui confronti sono stati certamente fondamentali per lo sviluppo del lavoro. I suoi suggerimenti sono stati di gran valore e ha aiutato a dare un senso alle mie idee.

Inoltre, ringrazio il relatore Marco Piumetti del Politecnico di Torino, per la sua disponibilità nell'accettare l'incarico e per aver messo a mia disposizione materiale utile per la stesura della tesi.

Il lavoro di tesi rappresenta la conclusione di un percorso accademico, ma anche di vita. È per questo motivo che ritengo doveroso ringraziare chi mi ha accompagnato in questi anni.

Un grazie speciale a tutta la mia famiglia, zii, cugini, che da sempre mi sostiene nel perseguire i miei obiettivi.

I miei genitori, Barbara e Fabrizio, senza il loro supporto questi anni non sarebbero trascorsi così spensieratamente. Da sempre ho l'esempio quotidiano di come determinazione, duro lavoro e assenza di presunzione siano le carte vincenti. Mi hanno trasmesso interessi e passioni e mi hanno insegnato che realizzarsi è cercare la sostanza e non l'apparenza.

Sara, perché da sempre sei la mia guida e il mio esempio. Nella nostra diversità ci completiamo.

I miei nonni, Albina e Francesco, che sono sempre stati più agitati di me ogni volta che avevo una prova importante.

I compagni di corso e di Politecnico, perché da sola non ce l'avrei mai fatta. Non è scontato incontrare altre persone con cui accompagnarsi in questo percorso. Insieme abbiamo affrontato fino all'ultima sfida a cui siamo stati sottoposti e mi hanno permesso di prendere con leggerezza l'intero periodo universitario.

Le amiche che mi conoscono da più tempo, perché io credo ancora nel non perdersi di vista e perché sanno tutta la strada che mi ha portata fin qui. Chi si sarebbe immaginato 10 anni fa questo giorno.

Grazie.

> *I shall go on shining, as a brilliantly meaningless figure in a meaningless world.*
>
> *F. Scott Fitzgerald*